Microstructural Evolution of Solid Oxide Fuel Cell: Modeling and Optimization

By

Taufiq Abdullah

Submitted to the graduate degree program in the Department of Mechanical Engineering and the Graduate Faculty of the University of Kansas in partial fulfillment of the requirements for the degree of Master of Science.

Dr. Lin Liu

Thesis Advisor Chair

Dr. Xianglin Li

Committee Member

Dr. Peter W. TenPas

Committee Member

Date Defended: 11/01/2016

The Thesis Committee for Taufiq Abdullah
certifies that this is the approved version of the following thesis:

Microstructural Evolution of Solid Oxide Fuel Cell: Modeling and Optimization

Chairperson Dr. Lin Liu

11/01/2016

Date approved

ABSTRACT

The solid oxide fuel cell (SOFC) with up to 60 % energy efficiency and a life expectancy of 40,000 hours has emerged as an ideal candidate to meet the energy challenges of the modern world. However, the commercialization of SOFC is hindered due to its high operating temperature, high manufacturing cost, and lack of structural reliability. Previous studies have investigated the development of functionally graded electrodes to improve SOFCs performance; however, further investigation needs to be done on the cell-level optimization for functionally graded electrodes. In addition, the performance of functionally graded SOFCs is influenced by the SOFC microstructural evolution at elevated operating temperature. Microstructural evolution cause performance degradation and crack formation at elevated operating temperate. It is generally believed that microstructural evolution caused by the coarsening of Ni particles of Ni-yttria stabilized Zirconia (YSZ) in the anode of a SOFC, which leads to the performance degradation and crack formation. Ni particle coarsening is believed to be controlled by the interface diffusion due to the minimization of total free energy of the anode system. High operating temperature of SOFC leads to the enhanced interface diffusion of Ni particle. In this work, a multi-scale electrode polarization model of SOFCs has been expanded and developed into a cell-level model using various nonlinear particle size and porosity graded microstructures. The cell-level SOFCs model has been utilized to reveal the complex relationship among the transport phenomena, which include the transports of electron, ion, and gas molecules through the electrode. The performance of functionally graded electrodes has been investigated to understand the effects of tailored electrode microstructures on cell power output, as well as microstructural evolution using diffuse-interface theory as well as phase-field method. The developed microstructural evolution framework is capable of exploring the quantitative effect of Ni particle coarsening by tracking the

effective properties (e.g., particle size, particle size ratio, TPB area) on the performance of SOFC. The TPB is found to be affected by microstructural evolution and the accumulation of pores is discovered to be responsible for crack formation. The work advances the understanding of the cell performance with graded microstructures and the effect of microstructural evolution on the performance of SOFC.

ACKNOWLEDGEMENT

I want to express gratefulness and humbleness to Almighty ALLAH for his kindness and mercy.

I would also like to take this opportunity to thank those who have assisted me throughout my graduate education and provided input and help during the writing of my thesis. First, I would like to thank Dr. Lin Liu for his great support and guidance in concept clarification, presentation of this research, and financial support. Without him, this work would not have been possible. I would also like to extend my appreciation to Dr. Li and Dr. Tenpass for their invaluable lecture teaching and for their support as committee members.

My gratitude also goes to Pengjian Guan, Changhong Liu, and the entire fuel cell research group for their innovative ideas, feedback, and support throughout my study.

TABLE OF CONTENTS

[1] Material in this chapter is a published paper: Abdullah, T. and L. Liu, "Simulation-based microstructural optimization of solid oxide fuel cell for low temperature operation", International Journal of Hydrogen Energy, Volume: 41, Issue: 31, Pages: 13632-13643, 2016.

[2] Material in this chapter is a published paper: Abdullah, T. and L. Liu, "*Meso-Scale Phase-Field Modeling of Microstructural Evolution in Solid Oxide Fuel Cells",* Journal of The Electrochemical Society, 2016. **163**(7): p. F618-F625.

List of Figures

List of Tables

CHAPTER 1 . INTRODUCTION

1.1 MOTIVATION

The world's ever-growing economy largely depends on the fossil fuel. This dependency may result in regional or global conflicts when it will come to energy crisis, since fossil fuels are not equally dispersed around the planet. In addition, the processes of refining and using fossil fuel have vastly adverse effects on the global environment. In 2010, 80% of the world's total energy demand was met by fossil fuel sources. Approximately 41% of the total CO_2 produced in 2010 was produced by the burning of fossil fuels, and this has caused the concentration of CO_2 in the atmosphere to experience a 40% increase when compared to the pre-industrial era [1]. This increase in atmospheric greenhouse gases is widely accepted and believed to be the single most significant driving factor of global warming. Excessive consumption of fossil fuels is expected to result in other negative effects including ocean acidification and the rising of global sea levels [2]. Therefore, the challenge herein is to explore a suitable alternative that would take the pressure off the fossil fuels and be more nature friendly.

By 2025, the electrical energy consumed by the world is expected to rise by more than 50% [3-6], as shown in Figure 1.1. The consumption rate of the total electricity of the world by U.S in 2003 is around 24%. And this rate is expected to grow to 44% in the first quarter of the new century. The installed generating capacity needs to be expanded extensively in order to meet the future demand of the global electricity. The installed electricity generating capacity is expected to

increase worldwide from 3,626 GW (gigawatts) in 2003 to 5,495 GW in 2025 (Figure 1.2) where the average annual growth rate is 2.2% [4-6].

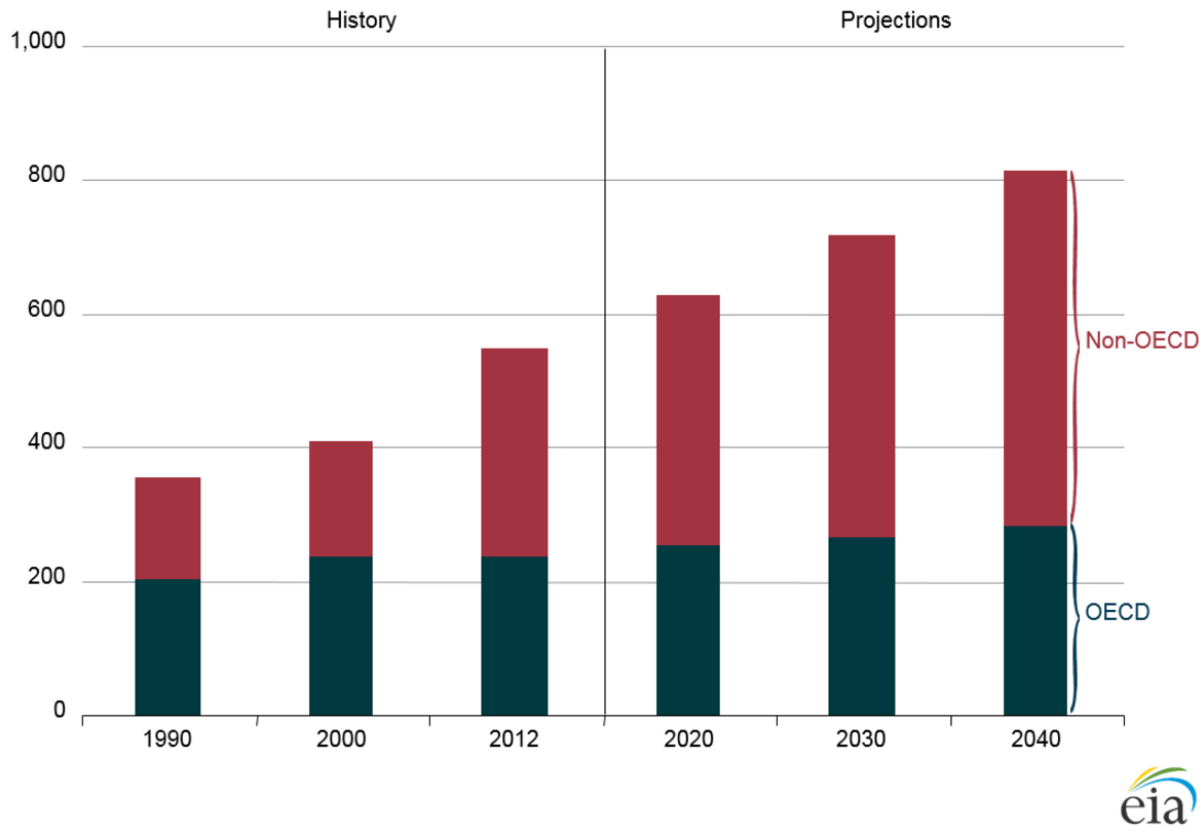

Figure 1.1. World and US electricity demand, 1990-2040 [3-5]

The U.S. electricity generating capacity is declining compared to the generating capacity of the world. In 2003, it was around 25%. But according to the estimation of Energy Information Administration (EIA), it will be around 20% in 2025 (Figure 1.2). But the capacity of electricity generation in this country is still expected to grow about 38% from 2000 to 2025 [3]. Although, , according to the electricity consumption data in Figure 1.1 and the generation capacity data in Figure 1.2 the consumption is growing faster than generation. If nothing changes, then the U.S. will have to import electricity in the near future.

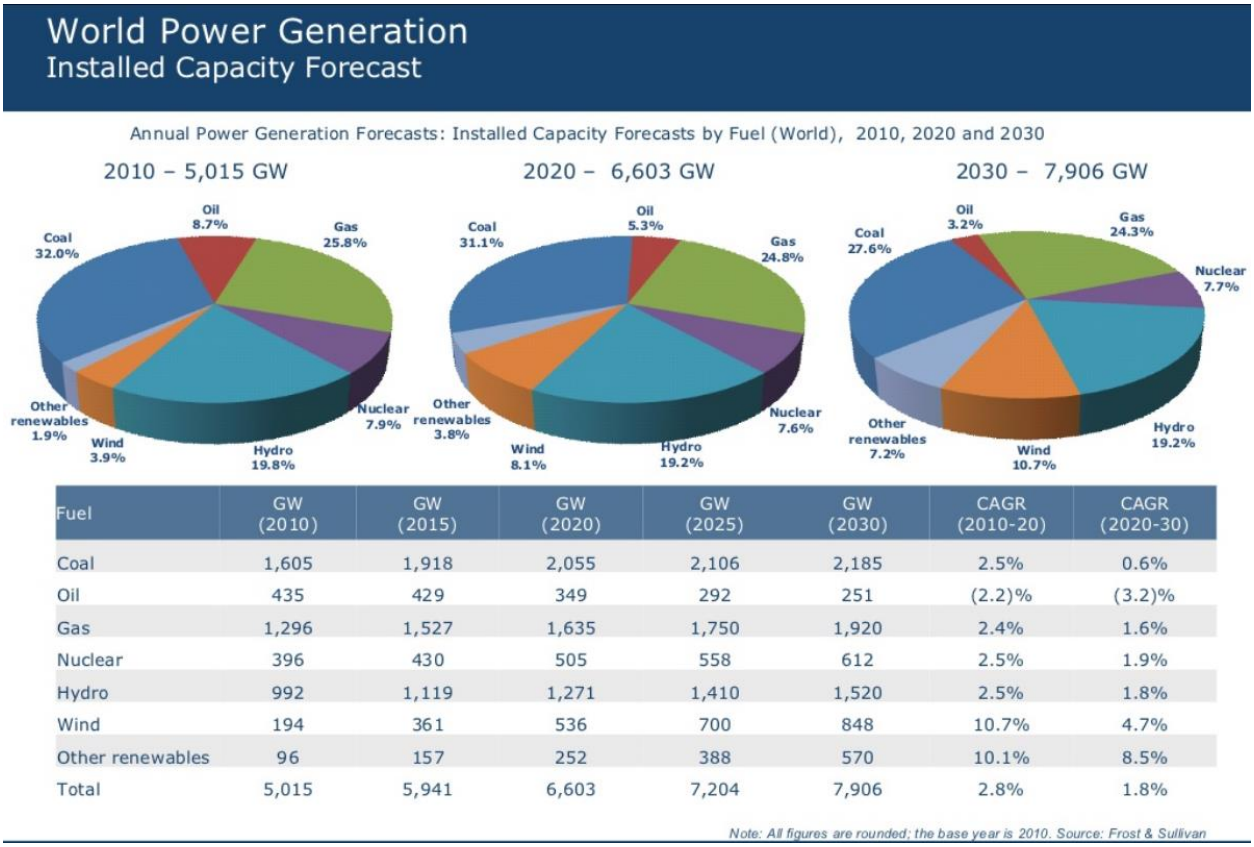

Fuel	GW (2010)	GW (2015)	GW (2020)	GW (2025)	GW (2030)	CAGR (2010-20)	CAGR (2020-30)
Coal	1,605	1,918	2,055	2,106	2,185	2.5%	0.6%
Oil	435	429	349	292	251	(2.2)%	(3.2)%
Gas	1,296	1,527	1,635	1,750	1,920	2.4%	1.6%
Nuclear	396	430	505	558	612	2.5%	1.9%
Hydro	992	1,119	1,271	1,410	1,520	2.5%	1.8%
Wind	194	361	536	700	848	10.7%	4.7%
Other renewables	96	157	252	388	570	10.1%	8.5%
Total	5,015	5,941	6,603	7,204	7,906	2.8%	1.8%

Note: All figures are rounded; the base year is 2010. Source: Frost & Sullivan

Figure 1.2. World electricity generating capacity 2010-2030 [3-5]

Electricity can be produced from many energy sources and in various ways. Conventional thermal power plants (using fossil fuels or nuclear energy) or alternative power generating units (such as hydropower stations, wind turbine generators, photovoltaic arrays, fuel cells, biomass power plants, geothermal power stations etc.) can be the generating source of electric power. Nuclear energy sources and fossil fuels are not renewable, and their sources are not unlimited. The ones that can be sustained for future use and can self-renew are the renewable energy resources, like the wind or solar energy. From Figure 1.3, where the world and U.S. electricity generation from 1980 to 2014 is shown by type, it is clear that the conventional fossil fueled thermal power plants and nuclear power plants are responsible for more than 80% of the world and the U.S.

electricity generation [6]. Apart from the hydro-electric power, there are limited other source of renewable energy. An overview will follow later in this section, where the present situation and the future development of various types of electricity generation will be discussed.

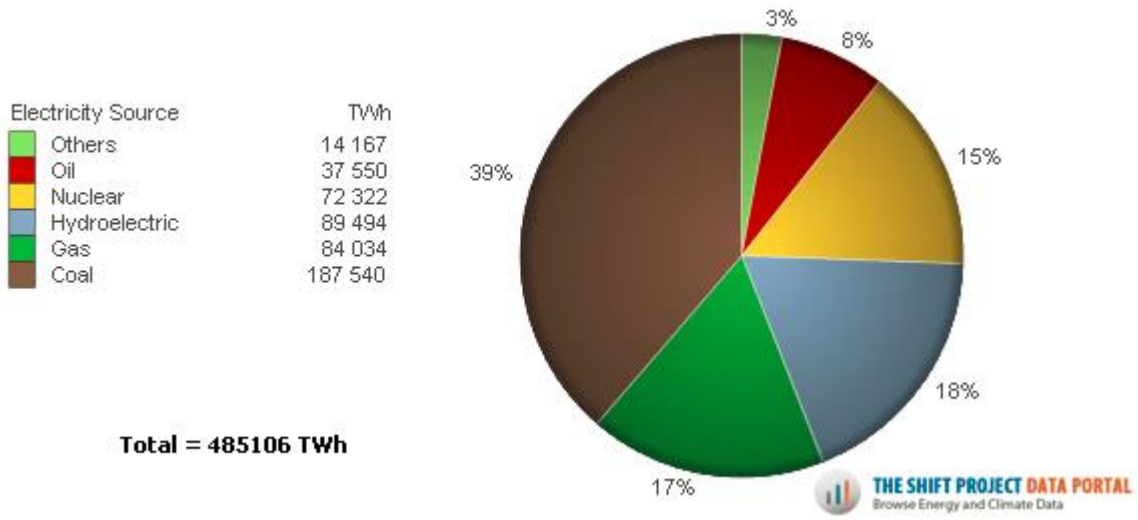

Figure 1.3. Electricity production from all energy sources from 1980 – 2014 [7]

Fossil fuels such as coal, oil and natural gases are used to generate electric power in conventional thermal power plants. Initially, water goes through a boiler, is heated up by the fossil fuels which are being burnt and then produces high temperature and high pressure steam. The produced steam then goes through a multi-stage steam turbine, by which a generator is operated to run electricity.

Coal has relatively abundant reserves and is of low price. That is why it is and will continue to be the leading raw material for electricity generation in the world and the U.S. The graphical representation is shown in Figure 1.4 and Figure 1.5 In terms of installed coal-fired capacity, the U.S. and China are the current front-runners,as both of these countries have huge amount of coal

reserves. Coal-fired electricity is anticipated to grow by 1.5% per year and coal is expected to fuel 38% of the world electricity generation in 2025 [5].

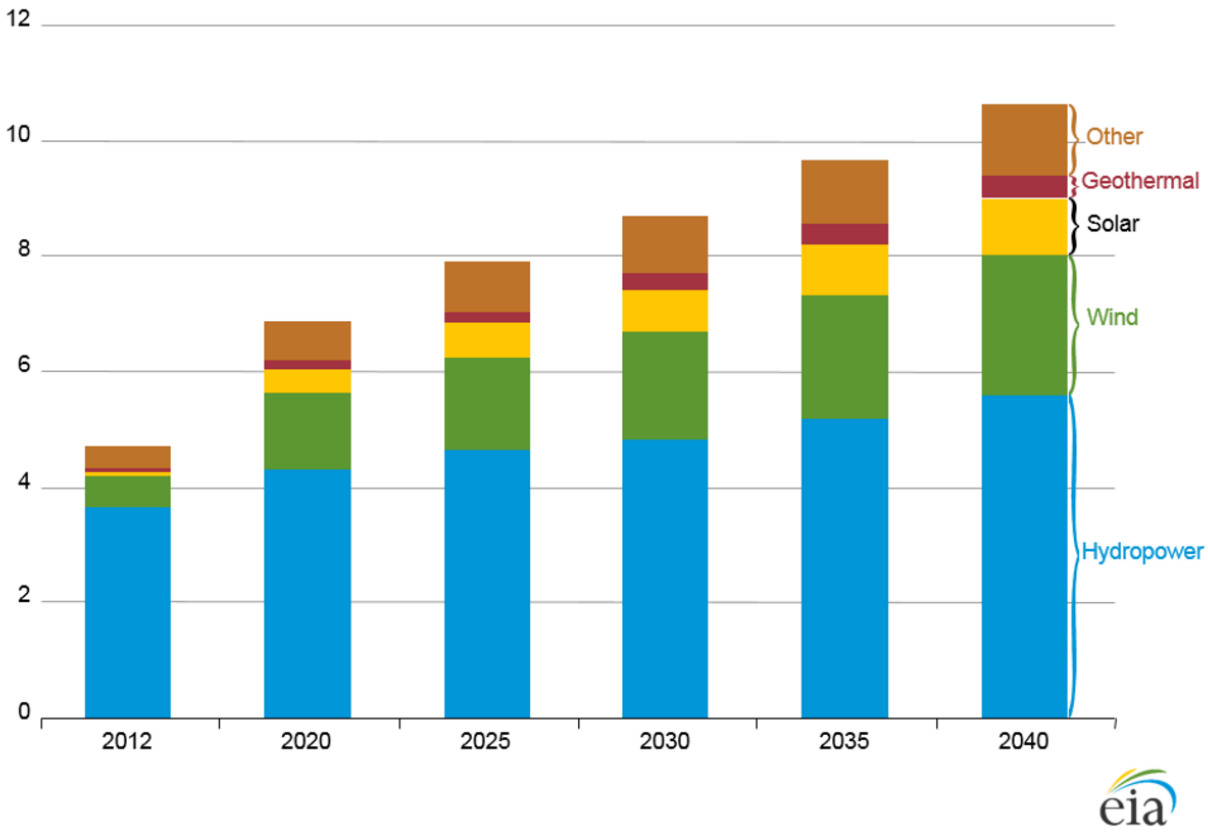

Figure 1.4. World electricity generation by fuel types [3-6]

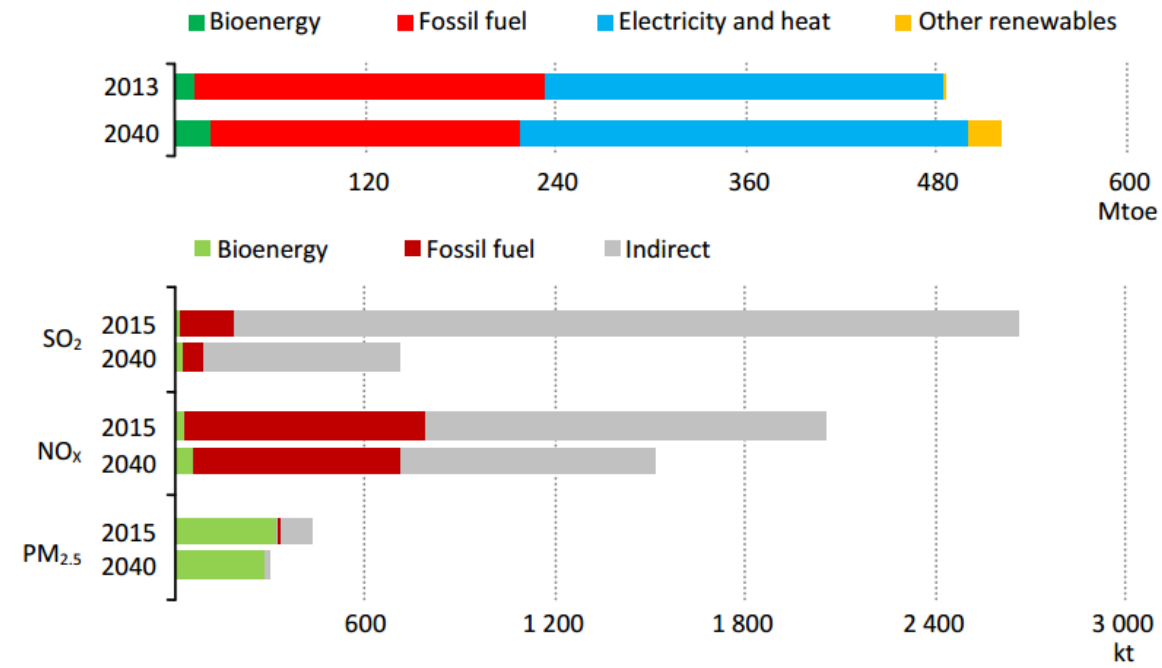

Sources: IEA; IIASA.

Figure 1.5. Energy demand in building and related pollutant emissions by fuel in the United States [3-6]

On the other hand, using natural gas as raw materials is a smart option for newer power plants because it is fuel efficient, flexible during operation, and can be deployed rapidly. Although the reserve of natural gas is not as plentiful as coal. In 2004, the amount of dry natural gas reserved in the U.S. was 192,513 billion cubic feet and the amount of natural gas consumed in the same country was 22,430.3 billion cubic feet [6]. The quarter of the amount consumed was used for producing electricity. At this consumption rate, the amount reserved would have been depleted by now. Fortunately, the natural gas is not the only means of resource and certainly the amount of reserve has changed [6]. The demand of crude oil is very high compared to its' reserve and it will continue to rise for around 2.5% per year [8]. The proven crude oil reserve was around 1277 billion barrels in 2005 and the daily demand of oil was 78.2 million barrels [8]. At this rate, clearly, the

reserve of the oil will not be able to sustain the increasing demand very long. Even the estimated undiscovered oil reserves, which is thought to be around 2800 billion barrels, will only be able to meet the present rate of demand for around 100 more years.

However, there are environmental sides to consider when it comes to fossil fuel usage. Also, high oil price and the instability of some oil production regions should also come into consideration. However, burning coal and fossil fuel has adverse impact on the environment due to the emission of greenhouse gasses. International communities have negotiated policies, like the Kyoto protocol, to reduce climate change by controlling the emission of CO_2 in developing countries [9]. The European Union has also committed to the EU 20-20-20 that outlines goals to reach emission levels 20% lower than in 1990, to increase the use of renewable energy by 20%, and to adopt an energy plan to increase total energy efficiency by 20% by 2020 [9]. However, the International Energy Agency (IEA) predicts that even with the successful implementation of EU 20-20-20, CO_2 levels will still be increased by 20% over the next 20 years [10]. Weighing the desire for inexpensive energy against the harmful effects caused by providing this energy, policymakers are facing a tremendous challenge and have started to look towards alternative energy sources for possible solutions.

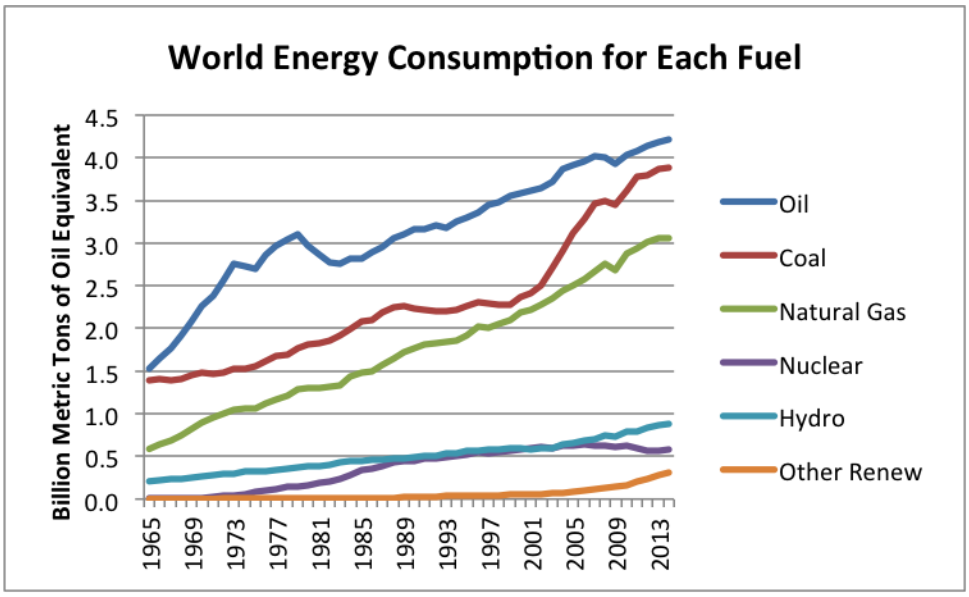

Figure 1.6. World energy consumption by fuel, showing each fuel separately on BP Statistical Review of World Energy 2015 [11]

1.2 FUEL CELLS

Fuel cell technology is an alternative electricity generation source considered to play a vital role in ensuring clean energy for a sustainable energy infrastructure. A fuel cell is an electrochemical energy conversion device that uses hydrogen and oxygen to produce electricity. Fuel cells provide electricity through the conversion of chemical energy; however, unlike batteries, fuel cells can operate continuously for as long as fuel and oxidant are supplied. The electrical energy converted by a fuel cell is created without combustion effects, which allows fuel cells to avoid Carnot cycle efficiency limitations [12]. Additionally, fuel cells can utilize different hydrocarbons, e.g., CO and natural gas.

Sir William Grove first introduced fuel cell using porous platinum as the electrodes and sulphuric acid as the electrolyte solution [13]. The first revolutionary step towards fuel cell was made by Dr. Francis T. Bacon in early 20^{th} century as he used nickel electrodes and built the first high pressure, medium temperature alkaline fuel cell system [14]. Later Pratt and Whitney adopted the concept of Bacon for the Apollo missions in the 1960s. The work of Bacon also stimulated the interest in fuel cell technology as an alternative to fossil fuel [14]. Since 1980, the fuel cell research stepped up to develop a wide range of technological concepts to make it sustainable as an alternative energy source.

The fuel cell technology can be divided into two groups: 1) high-temperature fuel cells, 2) low temperature fuel cells. Low temperature fuel cells, such as, Alkaline Fuel Cells (AFC), Polymer Electrolyte Membrane Fuel Cells (PEMFCs), and Phosphoric Acid Fuel Cells (PAFCs) use hydrated electrolytes, but they require expensive catalysts like platinum. On the other hand, high temperature fuel cells like molten carbonate fuel cells (MCFCs) and Solid Oxide Fuel Cells (SOFCs) that do not require any noble metal catalyst. They do not require any hydrogen reformer as the hydrogen can be produced internally. Comparison between different fuel cell technologies are shown in Table 1.1.

Table 1.1. Comparison of fuel cell technologies [15]

Fuel cell Type	Operating Temperature	Advantages	Disadvantages
Polymer Electrolyte Membrane (PEM)	50-100 ℃	• Solid electrolyte reduces corrosion and electrolyte management problems • Low temperature • Quick Start-up	• Expensive catalysts • Sensitive to fuel impurities • Low temperature waste heat
Alkaline (AFC)	90-100 ℃	• Cathode reaction faster in alkaline electrolyte, leads to high performance • Low cost components	• Sensitive to CO_2 in fuel and air • Electrolyte management
Phosphoric Acid (PAFC)	150-200 ℃	• Higher temperature enables it to operate at combined heat and power cycle (CHP) • Increased tolerance to fuel impurities	• Requires expensive catalyst • Longer start up time • Low current and power
Molten Carbonate (MCFC)	600-700 ℃	• High efficiency • Fuel flexibility • Can use a variety of catalysts • Suitable for CHP	• High temperature corrosion and break down • Long start up time • Low power density

Solid Oxide (SOFC)	700-1000 ℃	• High efficiency • Fuel flexibility • Solid electrolyte • Suitable for CHP • Can be used in hybrid/ gas turbine cycle	• High temperature corrosion and breakdown • Long start up time

Among different available technologies polymer electrolyte membrane fuel cells (PEMFC) and sold oxide fuel cells (SOFC) both have shown huge potential for transportation systems and stationary power generation systems [16]. Due to their high efficiency, low carbon emission, fuel flexibility, and flexible modular structure, they can be strategically placed for grid reinforcement, improving system integrity, and efficiency. In addition to that, the high temperature of SOFC can be used for residential and commercial applications [16], which is the research subject of this thesis.

1.3 SOLID OXIDE FUEL CELLS

SOFC is a solid state conversion device, which consists of an anode, electrolyte, and a cathode. Cathode is also known as the air electrode and reduces the oxygen to oxygen ions. The electrolyte transport the oxygen ion produced in the cathode side to the anode. The fuel electrolyte or anode oxidizes the fuel using oxygen ion to produce water and heat.

$$0.5O_2 + 2e^- = O^{2-}$$ (Cathode half reaction)

$$H_2 + O^{2-} = H_2O + 2e^-$$ (Anode half reaction)

$H_2 + 0.5O_2 = H_2O$ (Overall electrochemical reaction)

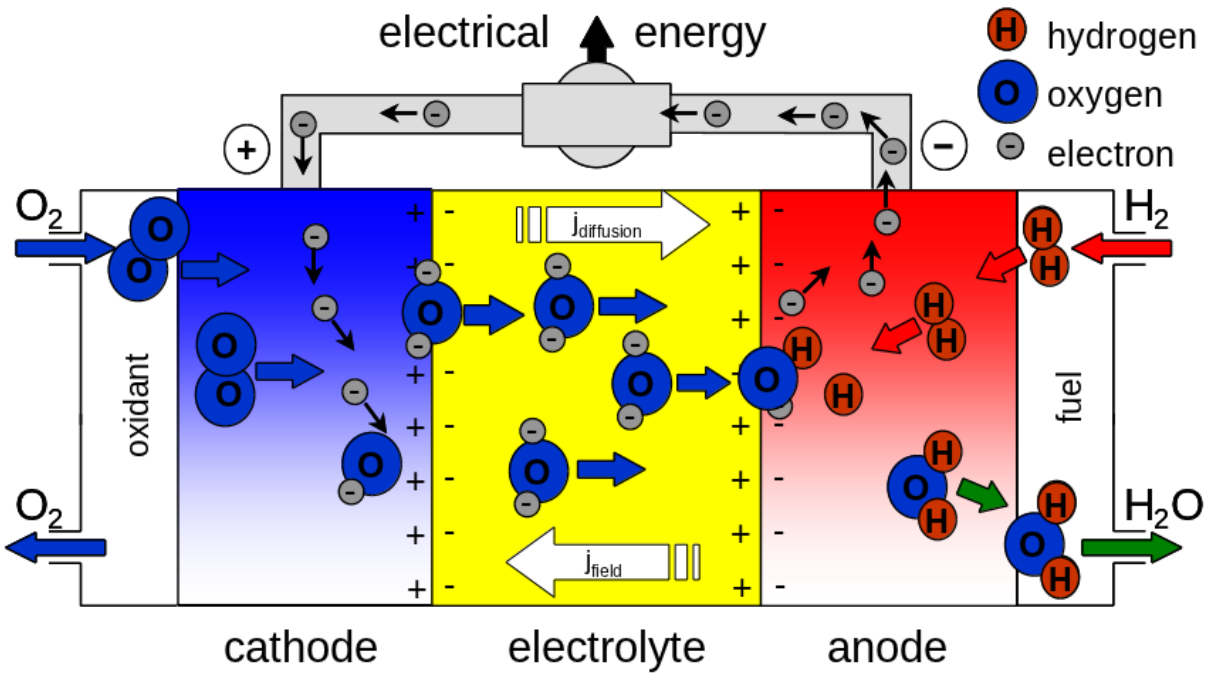

Figure 1.7. Transport and reduction mechanisms in a SOFC [17]

Multiple SOFC cells are stacked together to achieve the desired power output because the power output obtained from a single cell is relatively small. The gradient energy developed by the fuel gas oxidation reaction in the anode side controls the transportation of oxygen ions from cathode to anode. The electrons produced by the electrochemical reaction, flow from anode to cathode by an external connection. The aforementioned electrochemical reaction occurs in the triple phase boundary (TPB) area. TPB is the area of contact between the three phases (i.e., add on the three phases) necessary for the electrochemical reaction. The SOFC promises to meet the energy demand of the modern world in a more environment-friendly way. The higher efficiency of SOFC compared to the conventional energy sources reduces the emissions per unit electricity

production. In addition, SOFCs have demonstrated its advantage of fuel flexibility and impurity tolerance. It has demonstrated more than 50% energy efficiency and the utilization of its waste heat could raise the efficiency up to 85% [18].

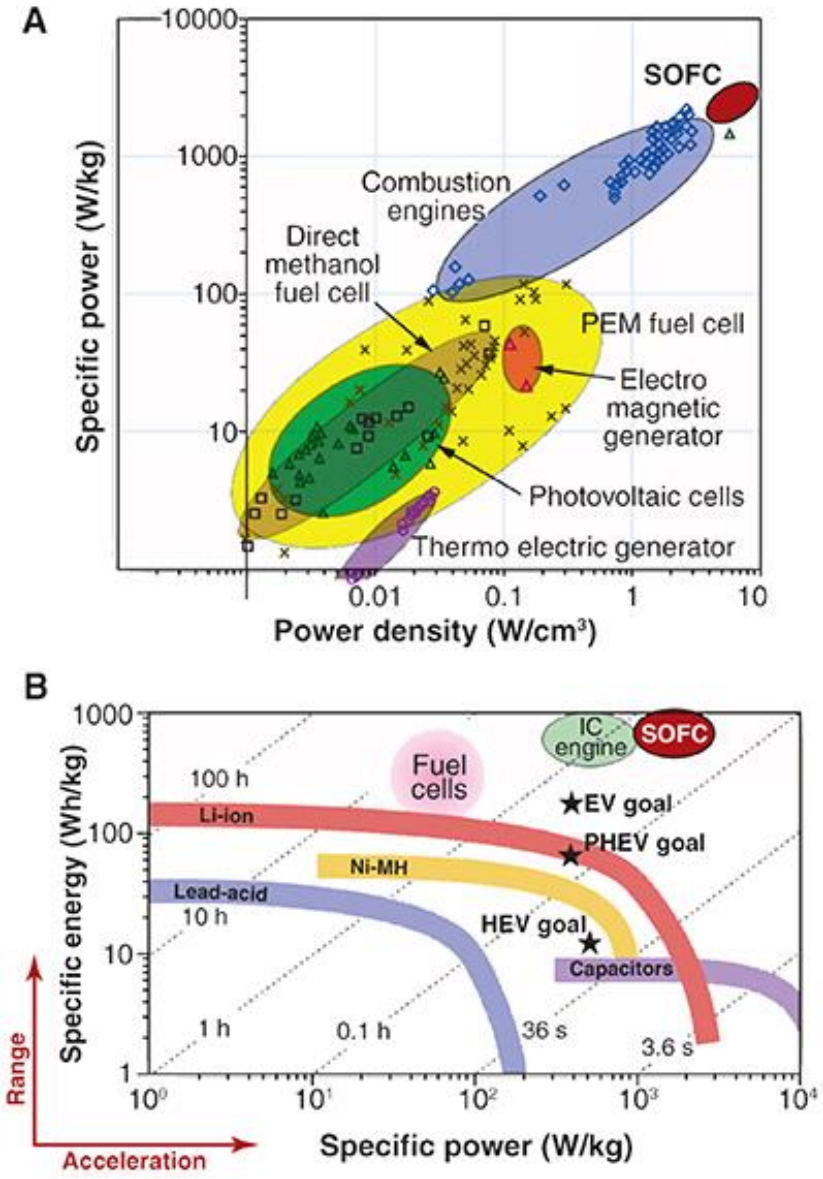

Figure 1.8. (a) Comparison of various energy generation (b) energy conversion technologies [19]

Despite the immense potential, the widespread use of SOFCs is hindered due to its high operating temperatures and lack of structural reliability. Hence, further investigation needs to be done on cell level operation to reduce the operating temperature of SOFC. Successfully tailoring the microstructure of SOFC electrodes can increase the efficiency at lower operating temperatures. In this work, a complete cell level model has been developed assuming the electrode composite particles to be randomly packed. Micro and macro models were developed separately and then integrated to establish a cell level model. The developed full cell model is used to investigate the electrochemical performance of SOFCs at lower operating temperature. The results of this modeling work closely match the referenced literature and provide a robust measure of SOFC performance. The conclusions drawn from the modeling work demonstrate that the performance of SOFCs can be improved with a tailored microstructure.

Furthermore, microstructural evolution occur in SOFCs at elevated operation temperature (above 600°C), which causes severe performance. Nickel (Ni) coarsening of Ni-yttria stabilized zirconia (YSZ) in the anode of SOFCs is believed to lead to the microstructural evolution. In the meanwhile, severe thermal stress due to high operation temperature is one of the main factors responsible for crack formation in the microstructure. Both microstructural evolution and crack formation have a significant impact on both electrochemical activity and structural integrity of SOFCs during operation. Based on diffuse interface theory, an integrated phase field model is established to investigate electrode microstructural evolution and crack formation in SOFCs. Then, the model is applied to SOFCs with tailored microstructures, to explore the synergy between microstructural evolution and SOFCs performance degradation. The results show that particle size and particle size ratio are the most influential microstructural parameters in the microstructural

evolution of SOFCs' electrochemical activity and accumulation of pore is responsible for crack formation. This work will provide one comprehensive evaluation computational tool for SOFC's long-term degradation analysis and novel electrode design.

1.4 RESEARCH OBJECTIVES

The objectives of the research are (1) to develop cell level multi-scale polarization model to optimize the peak power density of SOFC; 2) lowering SOFC operation temperature via computationally tailoring electrode microstructure; 3) to establish a meso-scale phase field model to analyze the microstructural evolution and performance degradation of SOFC; 4) to develop an integrated phase field model is established to investigate electrode microstructural evolution and crack formation in SOFCs.

1.5 THESIS ORGANIZATION

The rest of the thesis is divided into 5 chapters. Chapter 1 is the introduction. Comprehensive literature review on microstructural modeling and structural degradation can be found on chapter 2. Simulation based microstructural optimization of SOFC to reduce the operating temperature is presented in chapter 3. Mesoscale phase-field model of microstructure evolution in SOFC is illustrated in chapter 4. Conclusion and suggested future work is presented in chapter 5.

1.6 REFERENCE

1. Skea, J., *The renaissance of energy innovation.* Energy & Environmental Science, 2014. **7**(1): p. 21-24.
2. Rice, M.B., et al., *Climate change. A global threat to cardiopulmonary health.* American journal of respiratory and critical care medicine, 2014. **189**(5): p. 512-519.
3. (EIA), E.I.A., *International Energy Outlook 2005,.*
4. EIA, *International Energy Annual 2003.*
5. EIA, *System for the Analysis of Global Energy Markets 2005.*
6. EIA, *Annual Energy Outlook 2006 (Early Release).*
7. Project, T.S., *Breakdown of Electricity Generation by Energy Source.*
8. EIA, *World Oil Market, International Energy outlook - International Petroleum (Oil) Reserves and Resources.*
9. Protocol, K., *United Nations framework convention on climate change.* Kyoto Protocol, Kyoto, 1997.
10. Böhringer, C., et al., *EU climate policy up to 2020: An economic impact assessment.* Energy Economics, 2009. **31**: p. S295-S305.
11. Tverberg, G., *Our Finite World.* 2015.
12. Abdeljawad, F.F., *Mesoscale Modeling of Heterogeneous Materials Systems: From Solid Oxide Fuel Cells to Bulk Metallic Glasses.* 2014.
13. Chau, K., Y. Wong, and C. Chan, *An overview of energy sources for electric vehicles.* Energy Conversion and Management, 1999. **40**(10): p. 1021-1039.
14. Acres, G.J., *Recent advances in fuel cell technology and its applications.* Journal of Power Sources, 2001. **100**(1): p. 60-66.
15. Energy, U.S.D.o., *FUEL CELL TECHNOLOGIES PROGRSM.* 2011.

16. Wang, C., *Modeling and control of hybrid wind/photovoltaic/fuel cell distributed generation systems.* 2006.

17. Joos, D.-I.J., *Solid Oxide Fuel Cell: Modeling and Simulation.*

18. Flesner, R., *Modeling of Solid Oxide Fuel Cell functionally graded electrodes and a feasibility study of fabrication techniques for functionally graded electrodes.* 2009.

19. *SOLID OXIDE FUEL CELL PROMISE, PROGRESS, AND PRIORITIES WORKSHOP.* 2013.

20. Liu, L., et al., *Modeling of solid oxide fuel cells with particle size and porosity grading in anode electrode.* Fuel Cells, 2012. **12**(1): p. 97-108.

CHAPTER 2 . LITERATURE REVIEW

2.1 INTRODUCTION

The SOFC is merited with high efficiency, low carbon emission, fuel flexibility, and ease of operation [1]. The stationary SOFCs operation calls for a long life expectancy of more than 40,000 hours. Significant progress has been made in SOFC modeling in order to satisfy the ever growing demand of alternative energy source [2]. In this chapter, we summarize and review the literature for both experimental observations and theoretical investigations on microstructural properties, material system, and microstructural evolution of SOFC during operation.

2.2 SOFC CONFIGURATIONS

The SOFC unit cell is made of a metal-oxide electrolyte sandwiched between anode and cathode. A number of unit cells are stacked together to achieve the desired voltage for practical use. There are four different kinds of SOFC configurations: (1) planar, (2) tubular, (3) monolithic, and (4) coplanar, as seen in Figure 2.1. The anode-supported SOFCs are the most popular due to their high efficiency; Hence, we focus on the anode-supported SOFCs instead of electrolyte or cathode supported structures [3]. The improvements in fabrication techniques have resulted in increased peak power densities from $\sim 250\ \mathrm{mW/cm^2}$ at 1,000℃ in 1989 [4], to the vicinity of $2\ \mathrm{W/cm^2}$ at 800℃ for planar SOFC [4]. The electrolyte supported cell is popular for its ease of sealing. Coplanar configuration does not separate the reactant gasses, which leads to the lower

efficiency of SOFC. The tubular configuration does not require the anode to be on the outside of the tube. This type of configuration can be easily mass produced by extrusion and dip coating process, which has been developed by Siemens Westinghouse for decades [5]. The monolithic structure is used to increase the volumetric power efficiency.

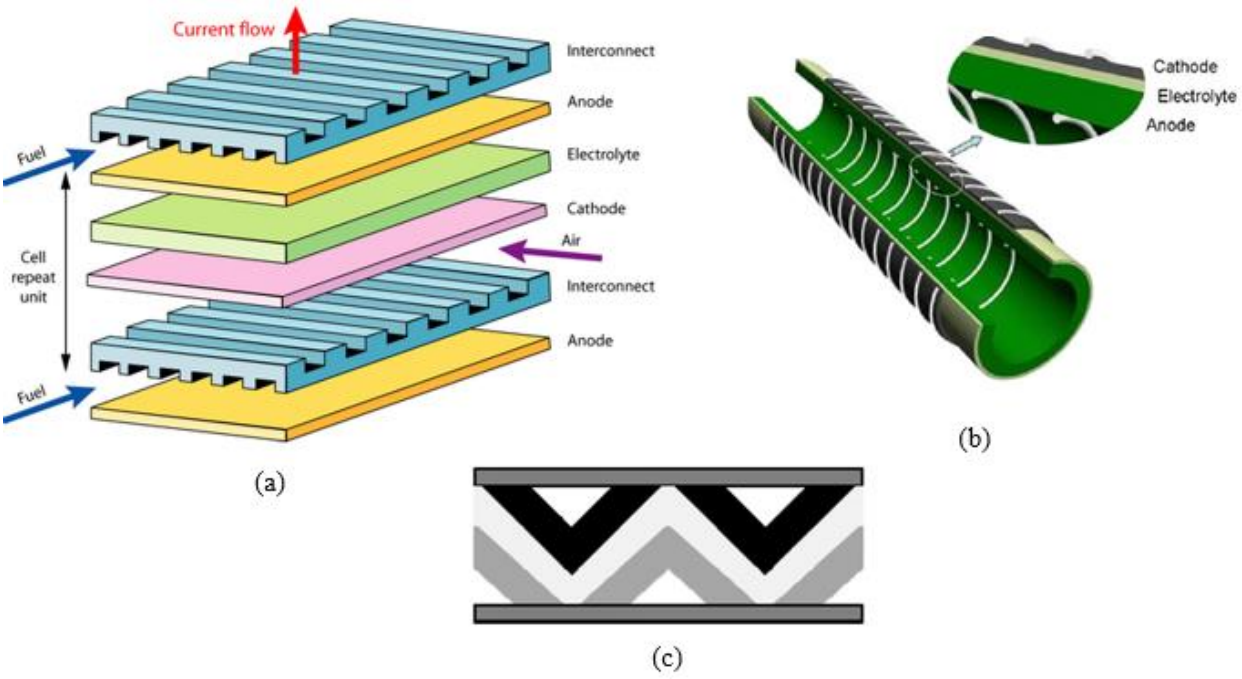

Figure 2.1. Schematic of SOFC configurations, (a) planar SOFC [6], (b) tubular SOFC [7], (c) monolithic SOFC [3]

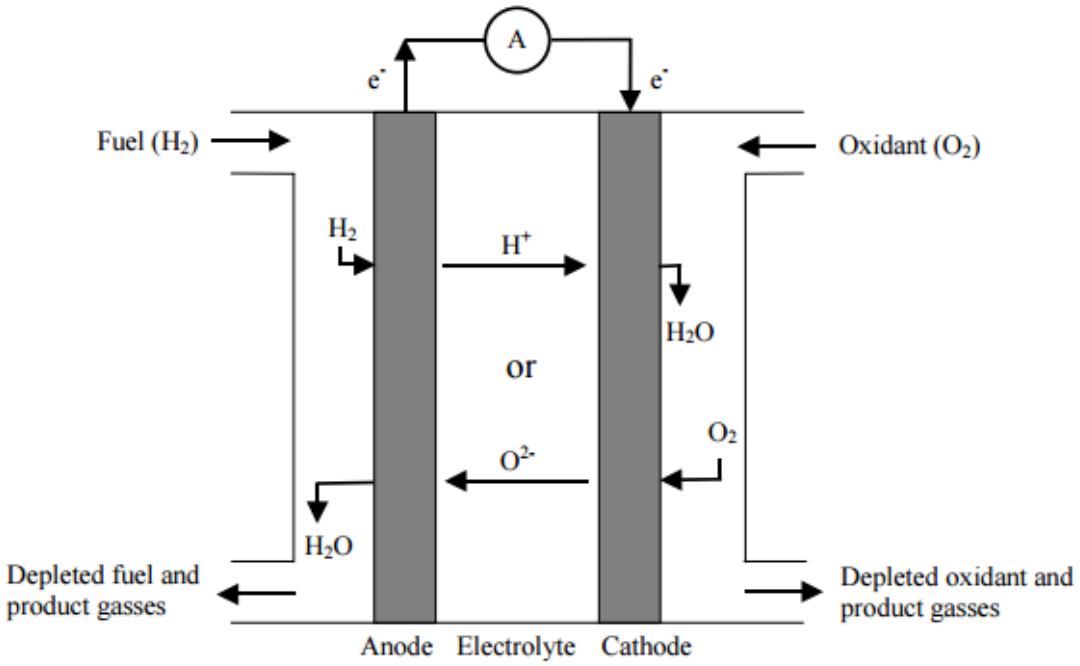

Figure 2.2. Schematic representation of SOFC working principle [8]

In a unit SOFC cell, the anode acts as oxidation reaction sites. At the anode-electrolyte interface, hydrogen molecules react with oxygen ions to produce water. Two electrons also get released as a result of this reaction. Spacil [9] in the 1960s firstly introduced the porous Ni/YSZ cermet as anode material. Spacil used the combination of Ni and YSZ for the following reasons: 1) Nickel is an excellent conductor of electronic charges and a good catalyst for the fuel oxidation, 2) High operating temperature of SOFC, facilitate the transportation of oxygen ion through YSZ composite, 3) the fuel gas and reaction byproduct can transfer through the porous Ni/YSZ composites, and 4) the use of porous Ni/YSZ composites mitigates mechanical stresses that caused at the anode-electrolyte interface due to the mismatch in thermal expansion coefficient. Currently, porous Ni/YSZ cermet is the most commonly used material system for SOFC anode [10], which can be fabricated using various techniques. A Ni/YSZ cermet can be fabricated inexpensively via wet ceramic processing such as screen printing [11], slurry spraying [4], or tape casting [12] of

NiO and YSZ powders. The processed mixture is then sintered at a high temperature to fabricate Ni/YSZ cermet, which is then placed in a hydrogen mixture at high temperatures to reduce the NiO to Ni [13, 14]. The other alternative techniques, such as atmospheric plasma spraying [15], vacuum plasma spraying [16], electrochemical vapor deposition [17], and laser reactive deposition [18] have also been used but their usage has been limited due to their high fabrication cost. In the Ni/YSZ cermet, Ni particle serves as oxidation catalyst [19] and the porous structure conducts electron and inhibits a channel for fuel transportation between the electrolytes and interconnect. The YSZ facilitates the transportation of oxygen ions and acts as a supporting structure for the coarsening of Ni particles during microstructural evolution. The YSZ also acts as a mediator to match the thermal expansion coefficients of the anode and electrolyte [20]. Typically, the Ni particle is $0.2 - 5$ μm in diameter, and generally, the range of the porosity level lies in the order of $30 - 40\%$ [21]. The electrons released by the reaction and the byproducts of the reaction are transported to the interconnect while fuel is supplied towards the anode-electrolyte interface [22]. Schematic representation of the reaction mechanism of a porous Ni/YSZ cermet has been shown in Figure 2.2. Furthermore, SOFC anodes are expected to be good electronic conductors and electro-catalytically active to allow for the transportation of oxygen ions and fuel gas to triple phase boundary (TPB) area. Triple phase boundaries (TPBs) are the area in contact where the electronic conducting Ni phase, ion conducting YSZ phase, and pore phase meet together [23]. The TPB area serves as a reaction site to produce electricity, hence, it is desired to have high TBP area to host more electrochemical reactions [24].

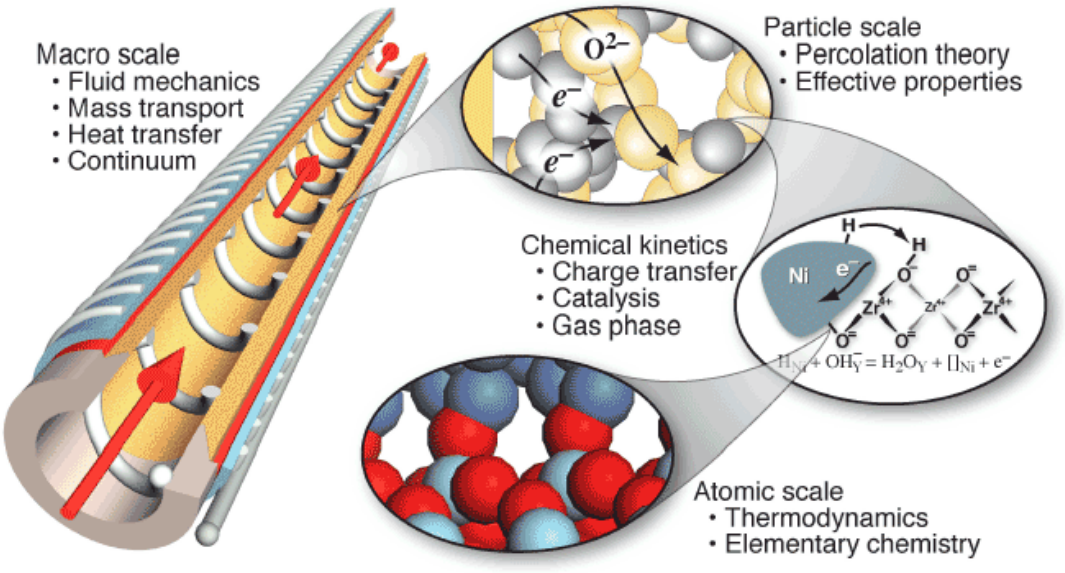

Figure 2.3. Schematics of TPB area [25]

2.3 SOFC PERFORMANCE

The SOFC performance is controlled by different efficiency parameters, these are; (1) thermodynamic efficiency, (2) voltage efficiency, and (3) current efficiency [3]. Thermodynamic efficiency is formulated by Nernst potential equation that is also known as open circuit voltage (OCV). The OCV is dependent on the operation temperature as well as the partial pressure of reactant gasses utilized during SOFC operation [26]. The OCV increases with decreasing temperature, as seen in Figure 2.4. However, temperature also has a significant impact on the ionic conductivity of the cell, as the ionic conductivity increases with the increasing temperature, hence it is desired to have a high temperature during SOFC operation.

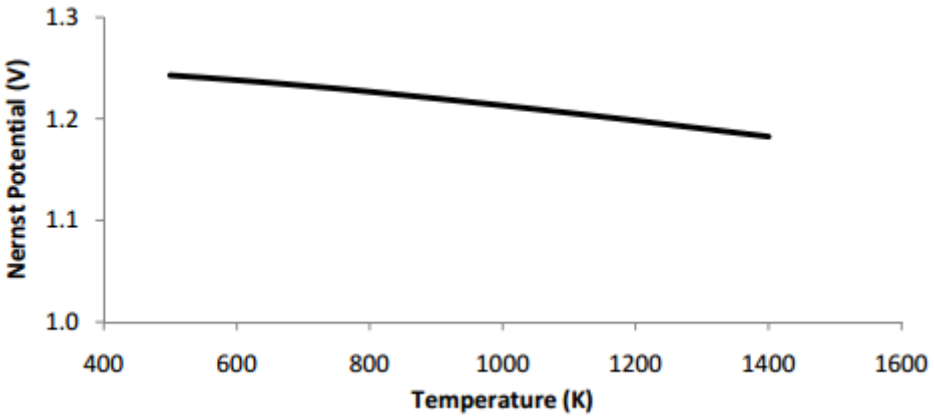

Figure 2.4. Nernst potential verses temperature [3]

In addition, SOFC operation is associated with three different voltage losses; (1) activation loss, (2) ohmic loss, and (3) concentration loss. The voltage loss is also known as polarization. Figure 2.5 shows three different voltage losses that are widely studied during SOFC operation. The energy required for the catalytic reaction to occur controls the activation loss. The rate of reaction is influenced by the temperature, hence, the temperature is a dominant factor in activation loss. Furthermore, the activation loss is dependent on the material, ion concentration, and surface area and can be formulated by Butler-Volmer equation [27-29]. Electrical and ionic resistance in determine the ohmic loss. Slow diffusion of reactant leads to the lack of reactants at the TPB area, which in turn causes the concentration loss [30, 31]. Literature shows, functionally graded micro-structures of anode reduces activation loss [32-34]. In a functionally graded electrode, the material properties (i.e., particle size, porosity, tortuosity, composition) changes gradually over the volume of the electrode as seen in Figure 2.6. The functionally graded structure can also reduce the concentration loss by enhancing diffusion and high electrochemical activity near the TPB area reduces the activation loss [35-37].

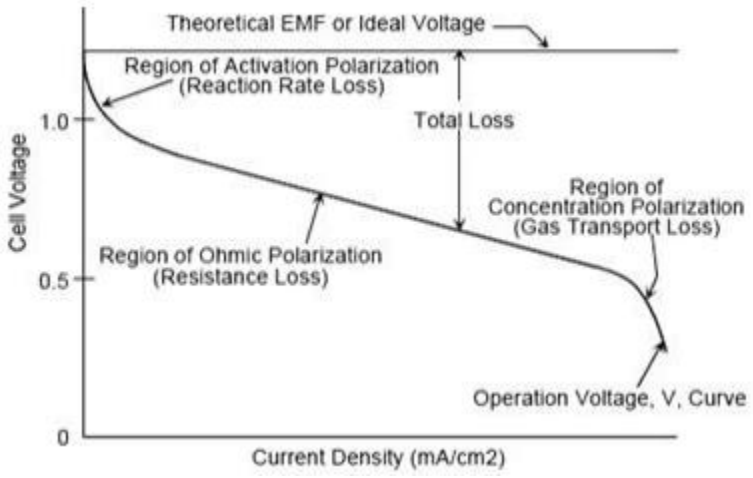

Figure 2.5. Typical polarization I-V curve of SOFC [38]

2.4 FUNCTIONALLY GRADED ELECTRODE MICROSTRUCTURE MODELING

In order to improve SOFCs performance, efforts have been put into microstructural investigations of mass transport and electrochemical reactions by developing numerical models [40-42]. The typical modeling used to consider electro-chemical properties of Ni/YSZ, however, recent investigations consider particle geometry to estimate TBP area [41]. The mass transportation of hydrogen and water vapor was formulated using Lattice Boltzmann method [43]. Distribution of oxygen ion was examined using Monte Carlo simulations [44]. Generally, the differential equations have been solved by using finite volume method, however, finite difference and finite element method has also been widely used [45].

Costamagna *et al.* [46] considered randomly packed sphere theory to treat electrode microstructure, which, provided analytical estimates of active area and effective conductivity for a randomly packed spherical bed. Chinda *et al.* [47] showed the effective ionic and electronic

conductivities in the reaction zone layers are the function of the necking factor that minimum activation loss is achieved for necking factor =0.5. Binary randomly packed sphere theory was also adopted by Bouvard and Lange [48] in their modeling work. These numerical investigations were mainly focused on the formulation of TPB area, however, more recent studies have been focused to improve the performance of SOFC anode by modifying electrode microstructures near TPB area [49-54]. Functionally graded electrode microstructure has been investigated to improve the performance of SOFC anode [3, 4, 10, 40, 41, 45, 46].

The functionally graded electrode computational modeling can be classified into the macro-scale and the micro-scale modeling based on the length-scale [55]. The Macro-scale modeling investigates the mass & heat transfer, and charge transport phenomena associated with the electrochemical reactions. The microscopic phenomena occurring within the fuel cell components is taken into consideration via the micro-scale modeling approach. Functionally grading of microstructure can optimize the TPB area by increasing the electrical-ionic conductivity, reducing the concentration loss, and decreasing the operating temperature. Studies have also been using three different kinds of grading in SOFC anode to improve the TPB area, namely, porosity grading, particle size grading, and composition grading. There are reports in the literature that attempt to correlate effective grading with microstructure [3, 4, 10, 40, 41, 45, 46]. Attempts have been made on microstructural optimization using linear particle size grading [34]. Particle size distribution has also been studied which strongly influence anode performance [56]. Two-layered anode structure has been investigated [57], which proposes a finer microstructure in the inner layer (electrolyte layer) than that of outer layer (interconnect layer). The finer inner layer maximizes the TPBs to lower activation loss, while the coarser outer layer facilitates the transportation of gas to

minimize concentration loss. Wang *et al.* [58] implemented a mathematical model to predict SOFCs performance by inserting one interlayer in electrodes. It was found that the insertion of an interlayer has the potential to improve the SOFC operation, but the cell performance strongly depends on the thickness of the interlayer [58].

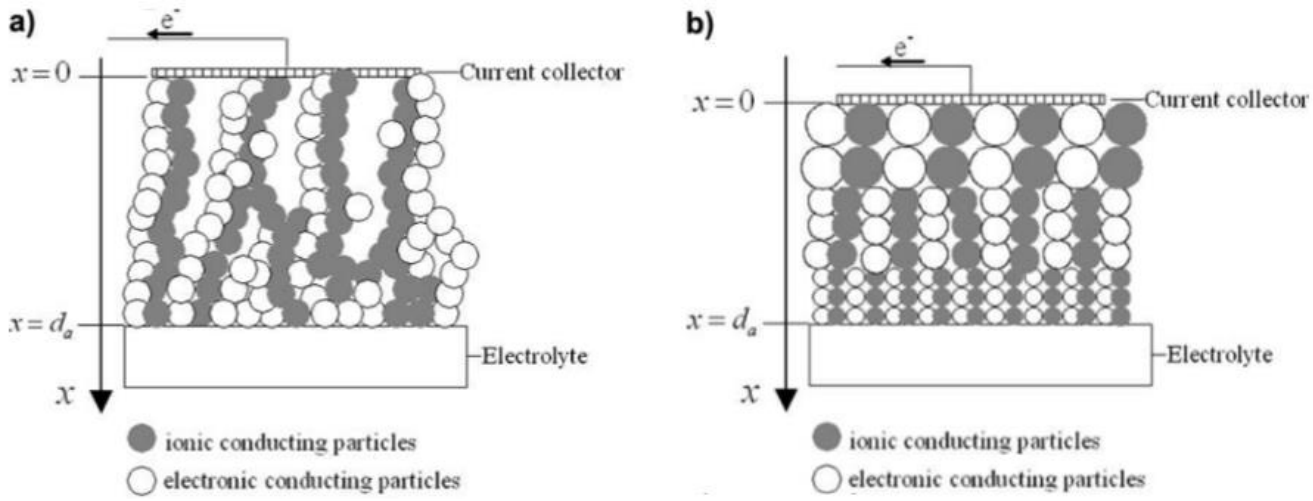

Figure 2.6. Schematice illustration of, (a) porosity grading, and (b) particle size grading [34]

The modeling work used the experimental data obtained by Jiang *et al.* [59]. Ni *et al.* [36] showed, the effective microstructural properties, in general, depend on electrode variables such as porosity and average grain size. A significant difference in particle size reduces the porosity and makes the structure more packed, which in turn indicates dense particle packing near the TPB area. On the other hand, comparable particle size makes the structure more porous, which reduces the TPB area and makes the structure more prone to activation loss. The larger porosity allows the greater diffusion of the molecule through the microstructure by reducing the concentration loss. Hence, the concentration loss of a functionally graded electrode can be reduced by applying densely packed structure near the electrode- electrolyte surface and porous structure near the fuel channel. The result showed significant performance improvement over the non-graded anode due to

reduced concentration loss and increased TPB area. Greene *et al.* [40] developed a micro-scale level model to investigate the ohmic loss in graded electrode computational model to explore mass transport and ohmic loss in graded SOFC electrodes from a micro-scale level. A porosity graded electrode is applied to demonstrate the reduction of overpotential. Wang *et al.* [60] investigated the particle size and tortuosity grading to compare the performance of functionally graded electrode with non-graded SOFC electrode, which demonstrated the particle size ratio appears to be increasing with the increase of porosity, which leads to the decrease of TPB area. The porosity is inversely proportional to the tortuosity, hence, the increase in porosity also reduces the active reaction sites by decreasing the tortuosity. Smaller tortuosity means the fuel molecules travels a shorter distance from one end of the electrode to the other. The porosity of a medium can be easily derived from its weight and density, but the tortuosity of porous media, in general, depends on the pore volume fraction, shape, and connectivity. A Bruggeman relation [61] exist expressing the tortuosity as a function of porosity. Chung *et al.* [47] investigated the validity of Bruggman relation for 16 different porous electrodes, which shows the total tortuosity as a function of active phase porosity.

2.5 MICROSTRUCTURAL EVOLUTION OF SOFC ANODE

The high temperature of SOFC enables it to operate without precious meatal catalyst. However, high operating temperature also lead to microstructural evolution of SOFC components. A typical SOFC electrode consists of three phase structure, i.e., electronic conducting phase (Ni phase), ionic conducting phase (YSZ phase), and gas phase (pore phase). Since the melting temperature of Ni is relatively low 1,453℃ [62], coarsening of Ni particle tends to occur during

long-term operation, leading to the microstructural evolution [63]. This high operating temperatures and aforementioned complex microstructure of SOFC anode lead to microstructural evolution during operation. The microstructural evolution of SOFCs leads to performance degradation. In this section, experimental findings and modeling results pertaining to the microstructural evolution in SOFC anode are reviewed as below.

2.6 PERFORMSNCE DEGRADATION DUE TO Ni COARSENING

In situ SOFC performance degradation have been investigated in terms of area-specific resistance increase or cell power or voltage decrease using electrochemical impedance spectroscopy (EIS) in a few articles [3-6]. However these EIS methods are unable to characterize mechanism and impact of each phase evolution. In recent studies, researchers investigated the degradation and failure mechanism of SOFC using non-electrochemical methods (i.e., X-ray tomography and X-ray diffraction) [7]. However, numerical modeling is required to get a clear understanding of time-dependent, 3D Ni-cermet based anode structure.

The SOFC anode is usually made of composite Ni/ YSZ composites, which has a complex morphology to facilitate the electrochemical reaction. The electrochemical reaction occurs in the TPB area where the pore phase, electron conducting phase, and ion conducting phase are in contact [8]. The electrochemical reaction mechanism of SOFC is yet to be fully understand however TPB is considered as the single most important geometrical parameter controlling the SOFC anode resistance [9]. Hence, it is expected to have increased TPB area. However, the anode microstructure is not stable and typically evolve with time due to the agglomeration and coarsening

and of Ni particle [10]. Microstructural evolution due to the coarsening of Ni particle leads to the performance degradation in SOFC microstructure. Coarsening process was first studied by Wilhemlm Ostwald in 1900 and reported particle-radius dependency of the material system [64-66]. The outcome of the result is known as Ostwald ripening [65], it is a process by which a material system releases its free energy. Lifshitz and Slyozov and Wagner, independently, developed a theory of particle coarsening which is later known as LSW theory [67, 68]. They considered spherical second phase particles embedded in a matrix phase with fixed position. The effects of the Ni particle coarsening on the TPB area, and the volume fraction of each phase on coarsening behavior have been the subject of many studies [69-77], where it was shown that the temporal evolution law for diffusion-limited coarsening is valid for all volume fractions.

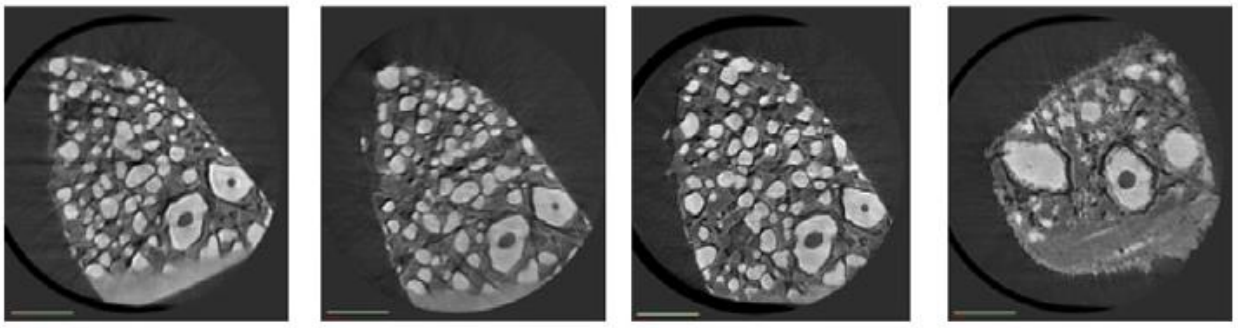

Figure 2.7. Evolution of Ni particle [78]

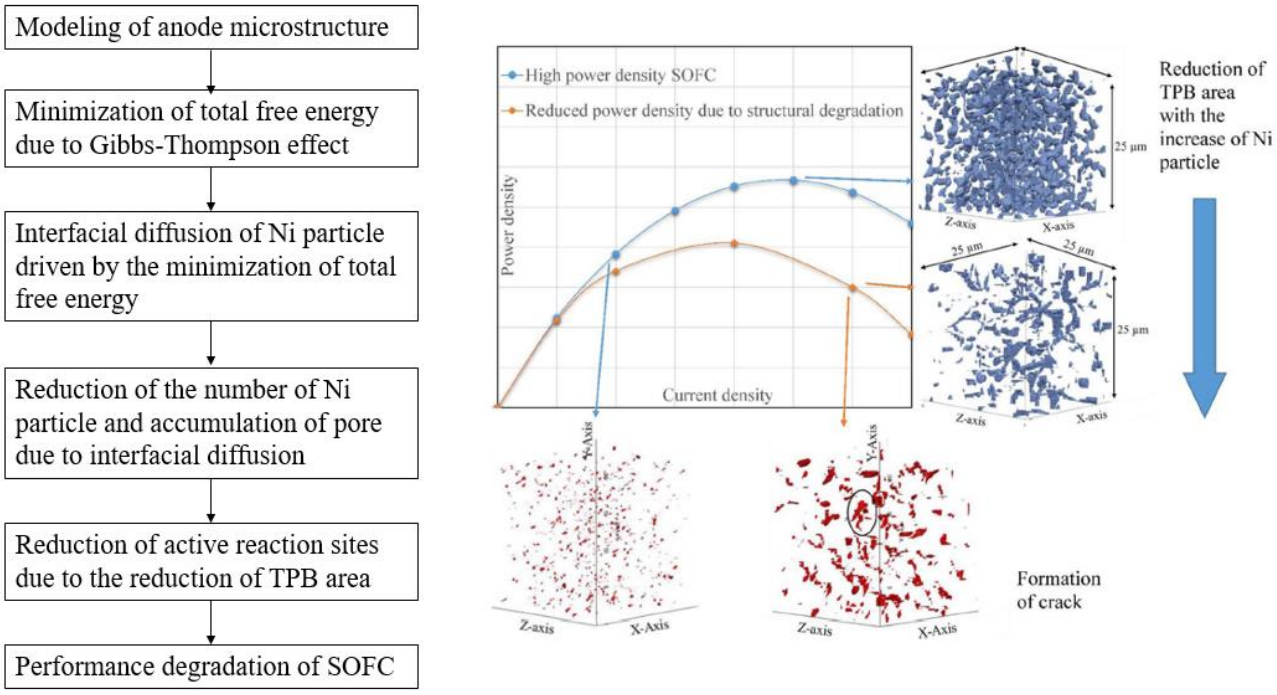

Figure 2.8.Schematic of SOFC anode evolution due to Ni particle coarsening

In addition the phase diffusion is dependent on the volume fraction of the each phase [65, 79]. The evolution of each phase leads to the reduction of total interfacial area. In an immiscible binary mixture the domain of a phase pure in each component is the interfacial area of that phase. The isotropic interfaces do not exhibit the orientation dependency. In general, the formulation of the microstructural evolution process starts with the diffusional flux that is dependent on the local interface curvature. The diffusional flux of a Ni particle is a capillary driven phenomena which is controlled by the interfacial free energy of the anode system. The pioneering work of Mullins [80, 81] investigated on the kinetic model of surface evolution due to capillary forces. It showed, regions with high mean curvature exhibit larger interfacial energy than that of the ones with smaller curvatures. The dominant transport mechanism (i.e., surface and volume diffusion, or vapor diffusion) dictates the final form of the governing equation, which describes the normal velocity of the interface in terms of the mean interface curvature.

In addition, high temperature leads to enhanced mass transport for the Ni phase. Variations in the local interfacial area of the Ni phase in combination with enhanced Ni phase mobility lead to a mass transport and redistribution of the Ni phase, where Ni atoms are transferred from regions of high curvature regions to low curvature regions (Figure 2.7). Furthermore, when two solid phases are in contact, a local equilibrium contact angle is established to balance interfacial energy [82]. For high operating temperature of Ni/YSZ system at SOFC, the experimental investigations determine the contact angle of Ni droplet on YSZ substrates to be approximately 117° [83]. Large contact angle indicates that the Ni particle thermodynamically does not favor contact into YSZ substrates. Figure 2.8 is a schematic illustration of the equilibrium contact angle of Ni phase on static YSZ structure, where, $\alpha > 90°$. Experimental efforts have been made to investigate the long term coarsening of Ni/YSZ anode. Ageing experiment by Simwonis *et al.* [84] showed the electrochemical activity is decreased by 33% over 4000 hours of operation. Micro-graph analysis of the investigation showed the Ni particle size is increased by 26%. Thyden [85, 86] conducted an experimental investigation for 17,500 hours and showed increase in H_2O concentration can promote the Ni particle coarsening and lead to the conductivity loss. The microstructural evolution in SOFC anode was investigated using optical microscopy, field emission-scanning electron microscopy (FE-SEM), SEM –charged contrast (SEM-CC), focused ion beam (FIB-SEM), and EIS measurement. Tanasisni *et al.* [87] reported coarsening of Ni particle leads to the anode degradation, which in turn reduce the performance of SOFC. The modeling also showed he cell potential also dropped and Ni particle size increased during operation. Despite these experimental efforts numerical models are required to investigate the quantitative correlation between microstructure and coarsening of Ni particle. The performance of SOFC is largely dependent on

the microstructural parameter yet only a very few models have considered the effect of Ni coarsening on the performance of SOFC [13-15]. These models are mainly based on simplified microstructure using empirical relations due to the difficulty of getting 3D microstructural information of NI/YSZ anode. In summary, various experimental observations [53, 71, 84, 88-92] indicate that Ni particle coarsening in SOFC anodes leads to: 1) continuous decrease in the TPB area due to the coarsening of Ni particle, which ultimately lead to the reduction in the total number of electrochemically active sites; 2) Decrease in Ni phase contiguity and electronic conductivity. When Ni clusters become spatially isolated, they can no longer conduct electrons to the current collector; and 3) Evolution of the pore phase microstructure, where the total number of pore decreases by increasing the average pore size.

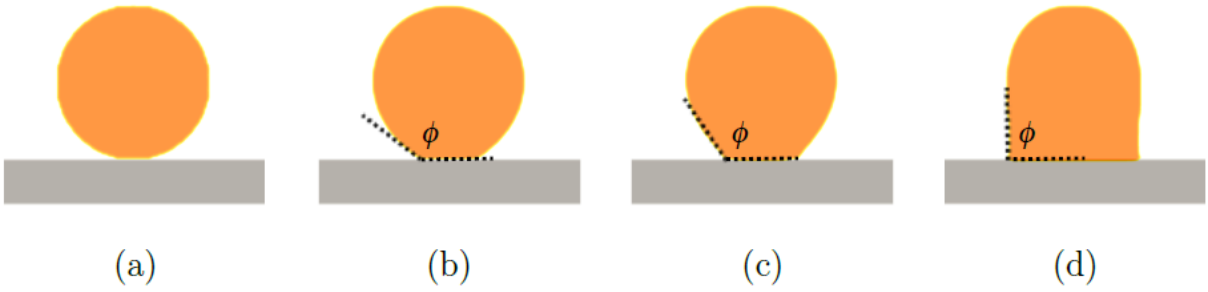

Figure 2.9. The evolution of a Ni (orange) particle on a static YSZ (grey) substrate as the state of equilibrium is approached with a contact angle [93]

2.7 CRACK FORMATION IN SOFC ANODES

The particle size distribution of SOFC anodes is controlled by controlled milling process. During the Anode forming process the combination of NiO and YSZ powders are sintered at high temperature to form a dense microstructure of NiO-YSZ networks as shown in Figure 2.9, where

NiO (green) and YSZ (pink) phases form interconnected networks. The anode is then reduced in order to transform NiO particles to Ni, thus creates a porous Ni/YSZ cermet as shown in figure. The pore phase is developed due to the shrinkage caused by the transformation of NiO to Ni, which act as pre-existing crack or defects in the structure. During SOFC operation, the anodes is kept at a reduced state and Ni phase is stabilized against oxidation. During the operation period of SOFC, Ni coarsening takes place. Ni coarsening is driven by the interfacial free energy where Ni particles along with several microstructural features evolve with time in order to reduce the total interfacial energy of the Ni phase. During SOFC microstructural evolution the Ni phase releases its interfacial free energy and grows in size. The average size of the Ni particle increases and the number of Ni particle decreases. The movement of Ni particle is controlled by the Gibbs-Thompson effect. And the transportation of Ni particle is done by interface diffusion. Elevated operating temperature of SOFC promotes the interface diffusion of Ni particle. During this interface diffusion the YSZ particle acts as supporting structure due to their low mobility. The other constituent of SOFC microstructure is gas phase or pore phase. Numerous pore exist in the structure to facilitate the transportation of gas. In addition to that pore phase transport the byproduct of electrochemical reaction. These pores are essential part of TPB area however at elevated temperature during the interface diffusion the pore phase agglomerate together to form a large continuous crack in the microstructure. In summary, the pore phase acts a pre-existing microstructural defects during the microstructural evolution. Whenever these pores agglomerate together to form a continuous structure crack formation occurs in the structure.

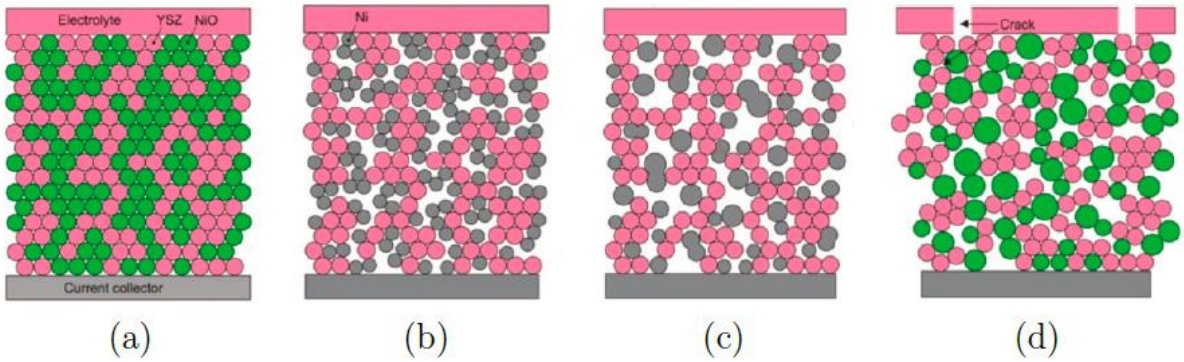

Figure 2.10. A schematic illustration of the microstructural evolution that are associated with a reduction-oxidation (redox) cycle. (a) A system is prepared by combining NiO and YSZ particles. (b) Initially, the anode is subjected to reducing environment to form a porous Ni/YSZ cermet, (c) Ni coarsening takes place during SOFC utilization. (d) When the anode is suddenly subjected to oxidizing environments, Ni particles are transformed to NiO. Ni, YSZ and NiO particles are shown in grey, pink and green respectively [94].

2.8 CONCLUSION

Therefore, a study of functionally graded electrode, will be introduced that is capable of simulating the complex gas transport phenomena and electrochemical reactions. The cell-level model is applied to provide insight into reducing SOFC operating temperature via optimizing electrodes' microstructures. The microstructural factors of SOFC are physically linked to each other in the real world, and considered in the modeling approach based on the microscopic correlation between the particle size, porosity, and particle size ratio. After that a meso-scale phase field model is developed to investigate the microstructural evolution and performance degradation

in SOFCs. The integrated phase field model is proposed using diffuse-interface theory and the Ginzburg-Landau equation. The modeling efforts focusing at Ni phase coarsening and its impact on features affecting the performance, assume that coarsening dynamics and mass transport processes are solely driven by high operating temperature which is ∼70% of the melting temperature of Ni. Electrochemical reaction will have a direct impact on several kinetic parameters that affect Ni coarsening. Furthermore, additional heating effects exist due to the localized nature of these reactions, which are typically confined to regions at and in the vicinity of TPB.

2.9 REFERENCE

1. Song, C., *Fuel processing for low-temperature and high-temperature fuel cells: Challenges, and opportunities for sustainable development in the 21st century.* Catalysis today, 2002. **77**(1): p. 17-49.
2. Campanari, S. and M. Gazzani, *High Efficiency SOFC Power Cycles With Indirect Natural Gas Reforming and CO2 Capture.* Journal of Fuel Cell Science and Technology, 2015. **12**(2): p. 021008.
3. Flesner, R., *Modeling of Solid Oxide Fuel Cell functionally graded electrodes and a feasibility study of fabrication techniques for functionally graded electrodes.* 2009.
4. Abbas, M.R., et al., *Microstructural evaluation of a slurry based Ni/YSZ thermal barrier coating for automotive turbocharger turbine application.* Materials & Design, 2016.
5. Casanova, A., *A consortium approach to commercialized Westinghouse solid oxide fuel cell technology.* Journal of power sources, 1998. **71**(1): p. 65-70.
6. Fisher, C., *Solid Oxide Fuel Cells.* 2015.

7. Shi, H., et al., *High performance tubular solid oxide fuel cells with BSCF cathode.* international journal of hydrogen energy, 2012. **37**(17): p. 13022-13029.

8. Huczkowski, P., *Effect of geometry and composition of Cr steels on oxide scale properties relevant for interconnector applications in Solid Oxide Fuel Cells (SOFCs)*. 2006, Fakultät für Maschinenwesen.

9. Spacil, H.S., *Electrical device including nickel-containing stabilized zirconia electrode*. 1970, Google Patents.

10. Jo, S.Y. and J.-Y. Park. *Electrochemical Performance and Stability of Perovskite Structured Anode Materials for Intermediate Temperature-Solid Oxide Fuel Cells*. in *Meeting Abstracts*. 2016. The Electrochemical Society.

11. Jamil, Z., et al., *Anode fabrication for solid oxide fuel cells: Electroless and electrodeposition of nickel and silver into doped ceria scaffolds.* International Journal of Hydrogen Energy, 2016. **41**(22): p. 9627-9637.

12. Xue, Y., et al., *Anode supported planar solid oxide fuel cells with the large size of 30 cm× 30 cm via tape-casting and co-sintering technique.* International Journal of Hydrogen Energy, 2016. **41**(3): p. 1871-1876.

13. Hoa, N.K., H. Abd Rahman, and M. Rao Somalu. *Preparation of Nickel Oxide-Samarium-Doped Ceria Carbonate Composite Anode Powders by Using High-Energy Ball Milling for Low-Temperature Solid Oxide Fuel Cells*. in *Materials Science Forum*. 2016. Trans Tech Publ.

14. Fernández-González, R., et al., *Decreasing the polarisation resistance of a Ni-YSZ solid oxide fuel cell anode by infiltration of a ceria-based solution.* International Journal of Hydrogen Energy, 2016.

15. Fan, E., J. Kuhn, and O. Kesler, *Suspension plasma spraying of La 0.6 Sr 0.4 Co 0.2 Fe 0.8 O 3− δ cathodes: Influence of carbon black pore former on performance and degradation.* Journal of Power Sources, 2016. **316**: p. 72-84.

16. Schiller, G., R. Costa, and K.A. Friedrich, *DEVELOPMENT OF CERAMIC FUNCTIONAL LAYERS FOR SOLID OXIDE CELLS.* Ceramics for Energy Conversion, Storage, and Distribution Systems: Ceramic Transactions, 2016. **255**: p. 19.

17. Ye, L., et al., *Highly Efficient Materials Assembly Via Electrophoretic Deposition for Electrochemical Energy Conversion and Storage Devices.* Advanced Energy Materials, 2016.

18. Solovyev, A., et al., *Magnetron-Sputtered YSZ and CGO Electrolytes for SOFC.* Journal of Electronic Materials, 2016: p. 1-8.

19. Yoon, K.R., et al., *Synthesis of Ni-based co-catalyst functionalized W: BiVO 4 nanofibers for solar water oxidation.* Green Chemistry, 2016. **18**(4): p. 944-950.

20. Noh, S., et al., *Performance Enhancement in Thin Film Solid Oxide Fuel Cells Using Metal-Mixed Ionic Electronic Conductors Bilayer Anode.* Science of Advanced Materials, 2016. **8**(1): p. 11-16.

21. Brandon, N. and D. Brett, *Engineering porous materials for fuel cell applications.* Philosophical Transactions of the Royal Society of London A: Mathematical, Physical and Engineering Sciences, 2006. **364**(1838): p. 147-159.

22. Zhu, W.Z. and S. Deevi, *Development of interconnect materials for solid oxide fuel cells.* Materials Science and Engineering: A, 2003. **348**(1): p. 227-243.

23. Gawel, D.A., J.G. Pharoah, and S.B. Beale, *Development of a SOFC performance model to analyze the powder to power performance of electrode microstructures.* ECS Transactions, 2015. **68**(1): p. 1979-1987.

24. Shearing, P., D. Brett, and N. Brandon, *Towards intelligent engineering of SOFC electrodes: a review of advanced microstructural characterisation techniques.* International Materials Reviews, 2013.

25. *Detailed Kinetic Modeling.*

26. Liso, V., et al., *Solid oxide fuel cell performance comparison fueled by methane, MeOH, EtOH and gasoline surrogate C 8 H 18.* Applied Thermal Engineering, 2016. **99**: p. 1101-1109.

27. Choudhary, T. and P. Murty, *Parametric Analysis of Syn-Gas Fueled SOFC with Internal Reforming*. 2015, SAE Technical Paper.

28. He, W., et al., *Gas transport in porous electrodes of solid oxide fuel cells: A review on diffusion and diffusivity measurement.* Journal of Power Sources, 2013. **237**: p. 64-73.

29. Harun, N.F., D. Tucker, and T.A. Adams, *Impact of fuel composition transients on SOFC performance in gas turbine hybrid systems.* Applied Energy, 2016. **164**: p. 446-461.

30. Mahjoub, R. and K.M. Mehraban, *Irreversibility and Electrochemical Modeling of GT-SOFC Hybrid System and Parametric Analysis on Performance of Fuel Cell.* cell, 2016. **2**: p. 2.

31. Ramírez-Minguela, J., et al., *Study of the entropy generation in a SOFC for different operating conditions.* International Journal of Hydrogen Energy, 2016. **41**(21): p. 8978-8991.

32. Abdullah, T. and L. Liu, *Peak Power Optimization of Solid Oxide Fuel Cells with Particle Size and Porosity Grading.* ECS Transactions, 2014. **61**(13): p. 33-46.

33. Liu, L., et al., *Modeling of solid oxide fuel cells with particle size and porosity grading in anode electrode.* Fuel Cells, 2012. **12**(1): p. 97-108.

34. Ni, M., M.K. Leung, and D.Y. Leung, *Micro-scale modelling of solid oxide fuel cells with micro-structurally graded electrodes.* Journal of Power Sources, 2007. **168**(2): p. 369-378.

35. Woolley, R.J. and S.J. Skinner, *Functionally graded composite La 2 NiO 4+ δ and La 4 Ni 3 O 10− δ solid oxide fuel cell cathodes.* Solid State Ionics, 2014. **255**: p. 1-5.

36. Ni, M. and T. Zhao, *Solid Oxide Fuel Cells: From Materials to System Modeling.* Solid Oxide Fuel Cells: From Materials to System Modeling, 2013: p. 978.

37. Sukeshini, M., et al., *Aerosol Jet® Printing of functionally graded SOFC anode interlayer and microstructural investigation by low voltage scanning electron microscopy.* Journal of Power Sources, 2013. **224**: p. 295-303.

38. Jain, R. and B. Mandal, *Studies on Ideal and Actual Efficiency of Solar Polymer Electrolyte Fuel Cell.* The AlternativeEnergyeMagazine. February, 2007.

39. Lee, S.-J., et al., *Microstructural analysis of the functionally graded electrodes in solid oxide fuel cells.* J. Ceram. Process. Res, 2012. **13**: p. 810-815.

40. Greene, E.S., W.K. Chiu, and M.G. Medeiros, *Mass transfer in graded microstructure solid oxide fuel cell electrodes.* Journal of Power Sources, 2006. **161**(1): p. 225-231.

41. Wang, C., *Microscale Correlations Adoption in Solid Oxide Fuel Cell.* Journal of Fuel Cell Science and Technology, 2015. **12**(4): p. 041006.

42. Zhu, H., et al., *Modeling elementary heterogeneous chemistry and electrochemistry in solid-oxide fuel cells.* Journal of the electrochemical society, 2005. **152**(12): p. A2427-A2440.

43. Iwai, H., et al., *Quantification of SOFC anode microstructure based on dual beam FIB-SEM technique.* Journal of Power Sources, 2010. **195**(4): p. 955-961.

44. Sunde, S., *Monte Carlo simulations of polarization resistance of composite electrodes for solid oxide fuel cells.* Journal of the Electrochemical Society, 1996. **143**(6): p. 1930-1939.

45. Ožbolt, J., F. Oršanić, and G. Balabanić, *Modeling pull-out resistance of corroded reinforcement in concrete: Coupled three-dimensional finite element model.* Cement and Concrete Composites, 2014. **46**: p. 41-55.

46. Costamagna, P., P. Costa, and V. Antonucci, *Micro-modelling of solid oxide fuel cell electrodes.* Electrochimica Acta, 1998. **43**(3): p. 375-394.

47. Chinda, P., et al., *Mathematical modeling of a solid oxide fuel cell with nearly spherical-shaped electrode particles.* Journal of sustainable energy and environment, 2010. **1**: p. 185-196.

48. Bouvard, D. and F. Lange, *Relation between percolation and particle coordination in binary powder mixtures.* Acta metallurgica et materialia, 1991. **39**(12): p. 3083-3090.

49. Hua, B., et al., *Carbon-resistant Ni-Zr 0.92 Y 0.08 O 2-δ supported solid oxide fuel cells using Ni-Cu-Fe alloy cermet as on-cell reforming catalyst and mixed methane-steam as fuel.* Journal of Power Sources, 2016. **303**: p. 340-346.

50. Gerdes, K., et al., *FUNCTIONAL GRADING OF CATHODE INFILTRATION FOR SPATIAL CONTROL OF ACTIVITY*. 2016, US Patent 20,160,020,468.

51. Qian, J., et al., *Chemically stable BaZr 0.7 Pr 0.1 Y 0.2 O 3-δ-BaCe 0.8 Y 0.2 O 3-δ bilayer electrolyte for intermediate temperature solid oxide fuel cells.* Electrochimica Acta, 2015. **151**: p. 497-501.

52. Liu, T., et al., *Novel light-weight, high-performance anode-supported microtubular solid oxide fuel cells with an active anode functional layer*. Journal of Power Sources, 2015. **293**: p. 852-858.

53. Pandey, A., et al., *In-situ Young's moduli of the constitutive layers in a solid oxide fuel cell.* Journal of Power Sources, 2015. **273**: p. 522-529.

54. Timurkutluk, B., et al., *A review on cell/stack designs for high performance solid oxide fuel cells.* Renewable and Sustainable Energy Reviews, 2016. **56**: p. 1101-1121.

55. Shaat, M. and S. Mohamed, *Nonlinear-electrostatic analysis of micro-actuated beams based on couple stress and surface elasticity theories.* International Journal of Mechanical Sciences, 2014. **84**: p. 208-217.

56. Bertei, A. and C. Nicolella, *Percolation theory in SOFC composite electrodes: effects of porosity and particle size distribution on effective properties.* Journal of Power Sources, 2011. **196**(22): p. 9429-9436.

57. Huan, D., et al., *High-Performanced Cathode with a Two-Layered R–P Structure for Intermediate Temperature Solid Oxide Fuel Cells.* ACS applied materials & interfaces, 2016. **8**(7): p. 4592-4599.

58. Wang, C., G. Huang, and R. Miller. *Computational Analysis of Solid Oxide Fuel Cell with Functionally Graded Electrodes*. in *Proceedings of the 49th AIAA Aerospace Sciences Meeting including the New Horizons Forum and Aerospace Exposition, Orlando, FL, USA*. 2011.

59. Jiang, S., W. Wang, and Y. Zhen, *Performance and electrode behaviour of nano-YSZ impregnated nickel anodes used in solid oxide fuel cells.* Journal of power sources, 2005. **147**(1): p. 1-7.

60. Wang, C., *A Computational Analysis of Functionally Graded Anode in Solid Oxide Fuel Cell by Involving the Correlations of Microstructural Parameters.* Energies, 2016. **9**(6): p. 408.

61. Pisani, L., *Simple expression for the tortuosity of porous media.* Transport in Porous Media, 2011. **88**(2): p. 193-203.

62. Liu, X., et al., *Investigation on microwave absorption properties of CuO/Cu 2 O-coated Ni nanocapsules as wide-band microwave absorbers.* RSC Advances, 2013. **3**(34): p. 14590-14594.

63. Khan, M.S., et al., *Fundamental mechanisms involved in the degradation of nickel–yttria stabilized zirconia (Ni–YSZ) anode during solid oxide fuel cells operation: A review.* Ceramics International, 2016. **42**(1): p. 35-48.

64. Abdeljawad, F.F., *Mesoscale Modeling of Heterogeneous Materials Systems: From Solid Oxide Fuel Cells to Bulk Metallic Glasses.* 2014.

65. Voorhees, P.W., *The theory of Ostwald ripening.* Journal of Statistical Physics, 1985. **38**(1-2): p. 231-252.

66. Vengrenovitch, R., *On the Ostwald ripening theory.* Acta metallurgica, 1982. **30**(6): p. 1079-1086.

67. Wagner, C., *Theorie der alterung von niederschlägen durch umlösen (Ostwald-reifung).* Zeitschrift für Elektrochemie, Berichte der Bunsengesellschaft für physikalische Chemie, 1961. **65**(7-8): p. 581-591.

68. Lifshitz, I.M. and V.V. Slyozov, *The kinetics of precipitation from supersaturated solid solutions.* Journal of physics and chemistry of solids, 1961. **19**(1-2): p. 35-50.

69. Chen, L. and J. Shen, *Applications of semi-implicit Fourier-spectral method to phase field equations.* Computer Physics Communications, 1998. **108**(2): p. 147-158.

70. Chen, L.-Q., *Phase-field models for microstructure evolution.* Annual review of materials research, 2002. **32**(1): p. 113-140.

71. Folch, R. and M. Plapp, *Quantitative phase-field modeling of two-phase growth.* Physical Review E, 2005. **72**(1): p. 011602.

72. Karma, A., D.A. Kessler, and H. Levine, *Phase-field model of mode III dynamic fracture.* Physical Review Letters, 2001. **87**(4): p. 045501.

73. Li, Q., et al., *Phase-field modeling of three-phase electrode microstructures in solid oxide fuel cells.* Applied Physics Letters, 2012. **101**(3): p. 033909.

74. Miehe, C., M. Hofacker, and F. Welschinger, *A phase field model for rate-independent crack propagation: Robust algorithmic implementation based on operator splits.* Computer Methods in Applied Mechanics and Engineering, 2010. **199**(45): p. 2765-2778.

75. Wise, S.M., et al., *Efficient phase-field simulation of quantum dot formation in a strained heteroepitaxial film.* Superlattices and Microstructures, 2004. **36**(1-3): p. 293-304.

76. Yeon, D.H., P.R. Cha, and M. Grant, *Phase field model of stress-induced surface instabilities: Surface diffusion.* Acta Materialia, 2006. **54**(6): p. 1623-1630.

77. Zuo, P. and Y.-P. Zhao, *A phase field model coupling lithium diffusion and stress evolution with crack propagation and application in lithium ion batteries.* Physical Chemistry Chemical Physics, 2015. **17**(1): p. 287-297.

78. Shearing, P., et al., *Exploring microstructural changes associated with oxidation in Ni–YSZ SOFC electrodes using high resolution X-ray computed tomography.* Solid State Ionics, 2012. **216**: p. 69-72.

79. Brailsford, A. and P. Wynblatt, *The dependence of Ostwald ripening kinetics on particle volume fraction.* Acta Metallurgica, 1979. **27**(3): p. 489-497.

80. Mullins, W.W., *Theory of thermal grooving.* Journal of Applied Physics, 1957. **28**(3): p. 333-339.

81. Mullins, W.W., *Two-Dimensional Motion of Idealized Grain Boundaries.* Journal of Applied Physics, 1956. **27**(8): p. 900-904.

82. Balluffi, R.W., S. Allen, and W.C. Carter, *Kinetics of materials*. 2005: John Wiley & Sons.

83. Tsoga, A., A. Naoumidis, and P. Nikolopoulos, *Wettability under Non-Reactive and Reactive Conditions in the Systems Ni/YSZ and Ni/Ti-TiO2/YSZ,* in *Interfacial Science in Ceramic Joining*. 1998, Springer. p. 79-86.

84. Simwonis, D., F. Tietz, and D. Stöver, *Nickel coarsening in annealed Ni/8YSZ anode substrates for solid oxide fuel cells.* Solid State Ionics, 2000. **132**(3): p. 241-251.

85. Hagen, A., J.F. Rasmussen, and K. Thydén, *Durability of solid oxide fuel cells using sulfur containing fuels.* Journal of Power Sources, 2011. **196**(17): p. 7271-7276.

86. Hagen, A., et al., *Durability study of SOFCs under cycling current load conditions.* Fuel Cells, 2009. **9**(6): p. 814-822.

87. Tanasini, P., et al., *Experimental and theoretical investigation of degradation mechanisms by particle coarsening in SOFC electrodes.* Fuel Cells, 2009. **9**(5): p. 740-752.

88. Brown, M., S. Primdahl, and M. Mogensen, *Structure/Performance Relations for Ni/Yttria-Stabilized Zirconia Anodes for Solid Oxide Fuel Cells.* Journal of the Electrochemical Society, 2000. **147**(2): p. 475-485.

89. Fouquet, D., et al., *Kinetics of oxidation and reduction of Ni/YSZ cermets.* Ionics, 2003. **9**(1-2): p. 103-108.

90. Fukui, T., et al., *Morphology control of Ni–YSZ cermet anode for lower temperature operation of SOFCs.* Journal of power sources, 2004. **125**(1): p. 17-21.

91. Iwata, T., *Characterization of Ni-YSZ Anode Degradation for Substrate-Type Solid Oxide Fuel Cells.* Journal of the Electrochemical Society, 1996. **143**(5): p. 1521-1525.

92. Sarantaridis, D. and A. Atkinson, *Redox Cycling of Ni-Based Solid Oxide Fuel Cell Anodes: A Review.* Fuel Cells, 2007. **7**(3): p. 246-258.

93. Abdeljawad, F.F., *Mesoscale Modeling of Heterogeneous Materials Systems: From Solid Oxide Fuel Cells to Bulk Metallic Glasses*, in *Mechanical and Aerospace Engineering Department*. 2014, Princeton University.

94. Faes, A., A. Hessler-Wyser, and A. Zryd, *A review of redox cycling of solid oxide fuel cells anode.* Membranes, 2012. **2**(3): p. 585-664.

95. Waldbillig, D., A. Wood, and D. Ivey, *Electrochemical and microstructural characterization of the redox tolerance of solid oxide fuel cell anodes.* Journal of Power Sources, 2005. **145**(2): p. 206-215.

96. Cassidy, M., G. Lindsay, and K. Kendall, *The reduction of nickel□ zirconia cermet anodes and the effects on supported thin electrolytes.* Journal of Power Sources, 1996. **61**(1): p. 189-192.

CHAPTER 3 . SIMULATION BASED MICROSTRUCTURAL OPTIMIZATION OF SOLID OXIDE FUEL CELL FOR LOW TEMPERATURE OPERATION[1]

3.1 INTRODUCTION

Solid oxide fuel cell (SOFC) power generation promises high energy efficiency while producing low emissions [1-4]. However, further commercialization of SOFCs is hampered by high operating temperatures (over 1000 K) [5-7], which limits the selection of materials. Moreover, severe thermal stress due to the high operating temperatures can cause serious structural failure (e.g., cracking and delamination) [8, 9]. For example, a model for crack formation in SOFCs under thermal cycling was previously developed and validated by Liu *et al.* [6]. Additionally, Liu *et al.* [9] investigated the detrimental effect of degradation of the anode microstructure on overall cell performance during thermal cycling. Due to the adverse effects of high operating temperature, much attention has been focused on lowering SOFC operating temperature [10-12]. However, decreasing the operating temperature can significantly reduce SOFCs efficiency as well as the power output [13]. Thus, anode-supported SOFCs were developed as one of the attempts to lower

[1] Material in this chapter is a published paper: Abdullah, T. and L. Liu, "Simulation-based microstructural optimization of solid oxide fuel cell for low temperature operation", International Journal of Hydrogen Energy, Volume: 41, Issue: 31, Pages: 13632-13643, 2016.

the operating temperature while maintaining overall cell performance [3, 14]. Investigation on anode-supported SOFC shows electrode microstructure plays a vital role in determining SOFC electrochemical behavior [5, 15-17]. The triple phase boundary (TPB) is widely considered to be one of the key microstructural features responsible for determining the electrochemical behavior of SOFCs [5, 17, 18]. As shown in Figure 3.1, the TPB is the contact area among the three phases (i.e., the ion conducting phase, electron-conducting phase, and gas phase) necessary for electrochemical reactions in the electrodes [19, 20]. The power output of SOFC is directly dependent on TPB area within the electrodes [9, 17, 21]. Many studies, including but not limited to [22, 23], show that optimizing the TPB area of the electrode is an important factor in achieving maximum power output. A precise structural characterization of TPB area is, therefore, crucial to correlate the electrochemical performances with its microstructure [17]. Experimental studies use high-quality sample preparation and high-resolution techniques such as Focus Ion Beam (FIB) [24, 25] and Atomic Force Microscopy (AFM) [26-31] techniques to explore TPB microstructure. The FIB-SEM (Scanning Electron Microscopy) technique is used for three-dimensional (3D) reconstruction of TPB microstructure. Wilson *et al.* [32] determined key microstructural parameters of TPB such as phase volume fractions, tortuosity, etc. of LSM-YSZ composite cathode using the FIB-SEM techniques. Symmetric LSM-YSZ-LSM cells were also investigated using the aforementioned techniques [33]. Size, shape, and topology of granular cermet were analyzed by Holzer *et al.* [34] using FIB-SEM techniques. AFM method is used to approximate electrochemical functionality [35]. Local irreversible electrochemical processes in the electrochemically active surface are demonstrated by using scanning probe microscopy approach [35].

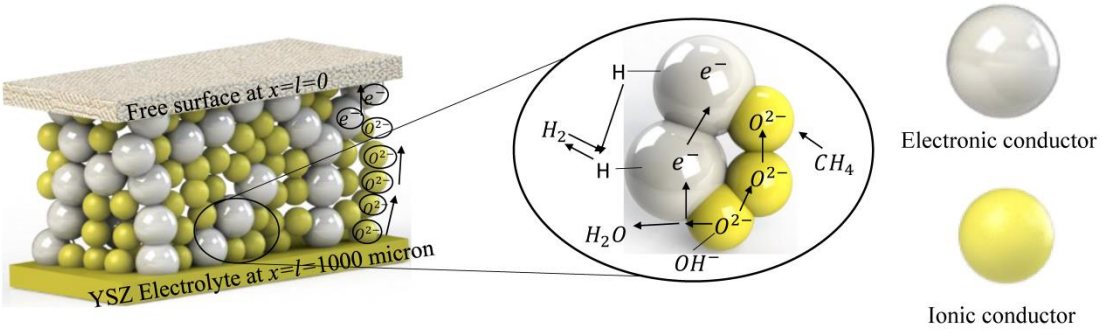

Figure 3.1. Schematics of TPB microstructure

Those aforementioned experimental investigations provide insight into the SOFC microstructure and its performance, however, the numerical model is required for theoretical explanation of experimentally observed phenomena as well as evaluating SOFCs' performance enhancement. Previous research has explored functionally graded electrode to optimize the TPB area of an electrode. Costamagna *et al.* [36] developed a microscopic model of an electrode formed by nearly spherical electronic and ionic conducting particles (i.e., randomly packed sphere theory). This modeling approach had also been used in recent studies [37, 38]. The results showed that volumetric composition and particle size strongly influence power output. Hussain *et al.* [39] investigated a 1-D anode supported cell with a thin layer of a reaction zone in the vicinity of the electrode. Greene *et al.* [40] confirmed a functionally graded electrode can increase electrochemical activity and cell performance. Ni *et al.* [41] presented a model exploring linearly graded electrodes to improve the peak power density of SOFCs.

These aforementioned microstructure models investigated particle-size graded electrodes and how it can be beneficial to improve power output. In addition, controlling electrode porosity can

further improve the performance of SOFCs with optimized TPB [42-44]. Experiments conducted by Holtapples *et al.* [45] showed porosity graded SOFC anodes can optimize gas transport to achieve high electrochemical activity at the anode-electrolyte interface. Joshi *et al*. [46] applied the lattice Boltzmann method to formulate a diffusion model. Liu *et al*. [3] developed an electrode-level model that focuses on the effects of particle-size- and porosity-graded anode on the performance of SOFCs. Despite previous efforts, much investigation is yet to be done on cell level modeling that considers particle-size- and porosity-grading in both anode and cathode. More attention should be focused on microstructural optimization from the standpoint of lowering operating temperature. In this work, we investigate offsetting adverse effects of lowering operating temperatures by tailoring the microstructures of SOFC electrodes considering the electrochemical behavior of both electrodes' based on grading range as well as grading profile. In detail, our previous developed electrode-level model [4] is extended to a full cell-level model, which incorporates the microstructures of both electrodes. The performance of functionally graded electrodes is numerically analyzed using the developed cell-level model. The cell-level model is applied to provide insight into reducing SOFC operating temperature via optimizing electrodes' microstructures.

3.2 MODEL DEVELOPMENT

In this paper, our previous models [3, 4] are extended to a cell level model for SOFCs. Both macro-scale and micro-scale characteristics of SOFC electrodes are considered. The micro- model considers the microstructural features, such as particle size, pore diameter, particle coordination number, and TPB area. Effective resistivity and effective conductivity of SOFC electrode are

treated by the micro-model based on aforementioned microstructural parameters. The macro modeling is mainly focused on three different types of voltage losses: activation loss, ohmic loss, and concentration loss. Additionally, macro-scale modeling focuses on investigating the effects of porosity change and different porosity/tortuosity ratios on optimizing TPB area. Then, the two models are integrated to formulate a cell level model of SOFC.

Following the micro-model of electrode developed by Costamagna *et al.* [47], which is based on randomly packed sphere theory, this modeling approach considers the electrode to be a mixture of spherical ionic and electronic particles with random particle packing. Various micro-model parameters such as porosity, particle size, particle co-ordination number, ionic-electronic conductor size ratio, ionic-electronic conductor particle number fraction, and bulk conductivity are taken into account to calculate effective resistivity and effective diffusivity. The effective conductivity and effective diffusivity are later used in the macro-modeling approach to formulating ohmic loss and concentration loss. The TPB area, *A*, can be calculated by the following equation [47],

$$A = \frac{\pi(r_{el} \sin\theta_{el})^2 n_{star} n_{el} n_{io} Z_{el} Z_{io} p_{el} p_{io}}{Z} \tag{3.1}$$

where θ is the contact angle between electronic and ionic conducting particles, r_{io} represents ionic particle radius, r_{el} represents electronic particle radius, p_{el} and p_{io} are the probabilities of the electronic and ionic conducting particles being in a percolation cluster, respectively. n_{el} is the number fraction of the electronic conducting particle, n_{io} is the number fraction of the ionic conducting particle. The effective resistivity, $\rho_{el(eff)}$, can be calculated by using Eq. (3.4)[36].

This work assumes the coordination number, *Z*, to be 6 [3, 4, 36, 48, 49] because of the random packing sphere of a 2-component mixture [50]. n_{star} is the number of particle per unit volume, can be determined by the following equation,

$$n_{star} = \frac{1-\varepsilon}{\frac{4}{3}\pi r_{io}^3\left(n_{io} + (1-n_{io})R_p^3\right)} \tag{3.2}$$

where ε denotes the porosity ranged from 0.3 to 0.7. The radius ratio of ionic to electronic conducting particles is denoted by R_P , which can be defined as follows in Eq. (3.3),

$$R_p = \frac{r_{io}}{r_{el}} \tag{3.3}$$

$$\rho_{el(eff)} = \frac{\left(1-n_{el,cr}\right)^2}{\gamma\sigma_{el}\left(n_{el}-n_{el,cr}\right)^2} \text{ and } \rho_{io(eff)} = \frac{\left(1-n_{io,cr}\right)^2}{\gamma\sigma_{io}\left(n_{io}-n_{io,cr}\right)^2} \tag{3.4}$$

where σ_{el} and σ_{io} define the collision diameter for the electronic and ionic conductors respectively. γ is the necking factor between the contacting particles. The necking factor is an adjustable parameter and takes into account the effect of necks between the conductive particles [51]. Researchers previously provided analytical estimates of effective conductivity for a randomly packed structure and Costamagna *et al.* [36] assumed necking factor to be constant. An investigation by Chinda *et al.* [52] showed the variation of the necking factor from 0.5 leads to increased activation loss. This modeling work assumes γ = 0.5, which is a commonly accepted value [3, 36, 50, 51]. The critical number fraction, $n_{el,cr}$ and $n_{io,cr}$ is obtained from percolation theory critical thresholds for randomly packed bimodal spheres [9, 53, 54].

Pore diameter, d_{pore}, can be calculated using Eq. (3.5), developed by Nam *et al.* [42].

$$d_{pore} = \frac{2}{3}\frac{d_{el}\varepsilon}{(1-\varepsilon)}\frac{n_{el} + (1-n_{el})R_p^3}{n_{el} + (1-n_{el})R_p^2} \tag{3.5}$$

where d_{el} is particle diameter.

The spheres contact at a particular angle determined by particle size, volume fraction, and coordination number. The binary particle mixture has a coordination number, Z, determined by Eq. (3.6),

$$Z_{el} = 3 + \frac{Z-3}{n_{el}+(1-n_{el})R_p^2} \text{ and } Z_{io} = 3 + \frac{(Z-3)R_p^2}{n_{io}+(1-n_{io})R_p^2} \tag{3.6}$$

where Z_{el} represents the average coordination number of the electronic particle, and Z_{io} is the average coordination number of the ionic particle.

The volume fraction $\emptyset$ can be determined from the particle size ratio, R_P, and the number fraction of electronic and ionic conducting particles, as shown in Eq. (3.7).

$$\emptyset_{el} = \frac{n_{el}}{n_{el}+(1-n_{el})R_p^3} \text{ and } \emptyset_{io} = \frac{n_{io}}{n_{io}+(1-n_{io})R_p^{-3}} \tag{3.7}$$

where $\emptyset_{el}$ and $\emptyset_{io}$ are the volume fractions of the electronic and ionic particles, respectively. The occurrence of electronic or ionic percolation is determined by the probability that a continuous cluster of conducting particles extends from the electrolyte to the electrode free surface.

Costamagna *et al.* [36] applied Eq. (3.8) to determine the probability of a particle being in a percolation cluster, P_{rm}. Subscript *m* denotes the particle conducting phase.

$$P_{rm} = \left(1 - \left(\frac{4.236 - Z_{m-m}}{2.472}\right)^{2.5}\right)^{0.4} \tag{3.8}$$

Here, the coefficient Z_{m-m} is set equal to 1.764 based on the experimental study by Kuo *et al.* [55]. For $0.154<R_p<6.464$, Suzuki's model [50] is proven to be valid. Suzuki's model utilizes Eq. (3.9) to calculate electronic and ionic coordination numbers,

$$Z_{el-el} = \frac{n_{el}Z}{n_{el}+(1-n_{el})R_p^2} \text{ and } Z_{io-io} = \frac{n_{io}Z}{n_{io}+(1-n_{io})R_p^{-2}} \tag{3.9}$$

In the macro-model, the open circuit voltage (OCV), activation loss, ohmic loss, and concentration (diffusion) losses are calculated. The operating cell voltage relationship can be expressed in Eq. (3.10) as,

$$V_{out} = V_{oc} - V_{loss} = V_{oc} - V_{ohm} - V_{act} - V_{conc} \tag{3.10}$$

where V_{out} is the output voltage, V_{oc} is the open circuit voltage, and V_{loss} is the total voltage loss. V_{loss} includes ohmic voltage loss (V_{ohm}), activation voltage loss (V_{act}), and concentration voltage loss (V_{conc}).

The basic equations that are used in macro modeling are shared among many research papers [2, 56, 57]. The open-circuit voltage of SOFC is calculated using the Nernst potential, as seen in Eq. (3.11),

$$V_{oc} = \frac{-\Delta g}{n_e F} + \frac{R_g T}{n_e F} \ln \frac{p_{H_2} \sqrt{p_{O_2}}}{p_{H_2O}} \tag{3.11}$$

where Δg is the Gibbs free energy, n_e is the number of electrons involved in the reaction, F is Faraday's constant, R_g is the universal gas constant, T is the temperature in kelvin scale, and p_A is the absolute gas pressure of species A.

In an electrochemical system, as described by [36, 41, 50], voltage loss is defined by the following equation

$$V_{loss} = \left(V_{el(eq)} - V_{io(eq)}\right) - (V_{el} - V_{io}) \tag{3.12}$$

where $V_{el(eq)}$ is the electronic equilibrium voltage, $V_{io(eq)}$ is the ionic equilibrium voltage, V_{el} is electronic voltage, and V_{io} is the ionic voltage.

The charge transport in a SOFC electrode can be modeled based on Ohm's law. Ohm's law for electronic and ionic conductors is written as,

$$\frac{dV_{el}}{dx} = \rho_{el(eff)} i_{el} \text{ and } \frac{dV_{io}}{dx} = \rho_{io(eff)} i_{io} \tag{3.13}$$

where $\rho_{el(eff)}$ is the effective electronic resistivity, i_{el} is the electronic current density, $\rho_{io(eff)}$ is the effective ionic resistivity, and i_{io} is the ionic current density. The charge balance in the electronic and ionic conductors is represented as,

$$\frac{di_{el}}{dx} = -\frac{di_{io}}{dx} = -Ai_n \tag{3.14}$$

where i_n is the exchange current density.

Ohmic loss occurs as a result of the voltage gradient driving the charge transport. By combining Eq. (3.12), (3.13), and (3.14), the second derivative of Eq. (3.12) can be written as,

$$\frac{d^2V_{loss}}{dx^2} = \rho_{io(eff)}\frac{di_{io}}{dx} - \rho_{el(eff)}\frac{di_{el}}{dx} = \left(\rho_{el(eff)} + \rho_{io(eff)}\right)Ai_n \tag{3.15}$$

The Butler-Volmer equation is applied to determine the activation loss that take place in the cell. In general, the Butler-Volmer equation is a rate determining equation that mainly depends on the reaction mechanism. Formation of water in various stages of SOFC reaction processes makes it difficult to determine the exact reaction mechanism. However, other SOFC modeling works have evaluated the number of electrons (n_e) transferred in the Butler-Volmer equation, and found this number to be one [1] by comparing theoretical models with experimental data [58, 59]. Activation polarization model verified the reaction to be a one-electron transfer mechanism [60, 61]. Therefore, the reaction mechanism assumes each reaction occurrence to be a one-step, single-transfer process represented by Eq. (3.16).

$$i_n = i_o \left\{ exp\left(\frac{\beta n_e F V_{act}}{R_g T}\right) - exp\left(-(1-\beta)\frac{n_e F V_{act}}{R_g T}\right)\right\} \tag{3.16}$$

where i_n is the charge transfer current density, i_o is the exchange current density, and β is the charge transfer coefficient and has been assumed to be 0.5 in previous modeling works [3, 36, 49, 62]. The charge transfer coefficient is the fraction of the activation voltage loss that affects the activation energy barrier, and thus the rate of electrochemical transformation. For single step electron transfer reactions the sum of anodic charge transfer coefficient and cathode charge transfer coefficient is equal to one [62, 63]. For simplicity the charge transfer coefficient β considered to be 0.5 on both sides to make a symmetric energy barrier.

The activation loss can be expressed as Eq. (3.17).

$$V_{act} = 2\frac{R_g T}{n_e F}\sinh^{-1}\left(\frac{i_n}{2i_o}\right) \tag{3.17}$$

Recent studies found the exchange current density i_o is directly proportional to the TPB area [48, 64, 65] and can be expressed as,

$$i_{O(a)} = \alpha_a A\left(\frac{P_{H_2}}{P}\right)\left(\frac{P_{H_2O}}{P}\right) exp\left(-\frac{E_a}{RT}\right) \tag{3.18}$$

$$i_{O(c)} = \alpha_c A\left(\frac{P_{O_2}}{P}\right)^{0.25} exp\left(-\frac{E_c}{RT}\right) \tag{3.19}$$

where α_a and α_c are the coefficient for the exchange current density of the anode and the cathode, p_{H_2} is the inlet hydrogen pressure, p_{H_2O} is the inlet water vapor pressure, and E_a and E_c are the activation energy at the anode and cathode.

The concentration loss, or mass transfer loss, can be calculated from the Nernst potential difference between the bulk and TPB via Eq. (3.20),

$$V_{conc} = -\frac{R_g T}{n_e F} \ln\left(\frac{p_{r,H_2} p_{H_2O}}{p_{H_2} p_{r,H_2O}}\right) \tag{3.20}$$

where p_{r,H_2} is the hydrogen pressure within the electrode and p_{r,H_2O} is the water vapor pressure within the electrode. The hydrogen and water vapor pressures inside the electrode can be calculated by Eq. (3.21),

$$p_{r,H_2} = p_{H_2}^i - \frac{RTl_a i_n}{n_e F D_{a(eff)}} \text{ and } p_{r,H_2O} = p_{H_2O}^i - \frac{RTl_a i_n}{n_e F D_{a(eff)}} \tag{3.21}$$

where l_a is the anode thickness and $D_{a(eff)}$ is the anode effective diffusion coefficient.

The partial pressure gradient along the thickness of the anode can be obtained by combining the Fickian diffusion and current flux flowing in the electrode, shown in Eq. (3.22),

$$\frac{dp_{H_2}}{dx} = -\frac{R_g T i_n}{2F D_{(eff)}} \tag{3.22}$$

where $D_{(eff)}$ is the effective diffusion coefficient. Calculation of the effective diffusion coefficient can be found in the Appendix. Eq. (3.22) is valid for all depths throughout the electrodes and can account for hydrogen consumption when combined with the Butler-Volmer equation. The second-order derivative of total voltage loss is expressed as Eq. (3.23) and utilizes the Butler-Volmer equation coupled with the mass transport equation [36, 41, 50]. By combining Eqs. (3.14), (3.15), (3.16), (3.21), and (3.22), a system of coupled differential equations for the anode can be derived. These are represented by Eqs. (3.23), (3.24), and (3.25),

$$\frac{d^2V_{loss}}{dx^2} = \left(\rho_{el(eff)} + \rho_{io(eff)}\right) A i_o \left[\frac{p_{r,H_2}}{p^i_{H_2}} exp\left(\frac{\beta n F V_{loss}}{RT}\right) - \frac{p_a - p_{r,H_2}}{p_a - p^i_{H_2}} exp\left(-(1-\beta)\frac{nFV_{loss}}{RT}\right)\right] \tag{3.23}$$

$$\frac{dp_{r,H_2}}{dx} = -\frac{RT}{2F}\frac{i_{el}}{\left(1 - \frac{p_{r,H_2}}{p_a}\right) D_{H_{2(eff)}} + \left(\frac{p_{r,H_2}}{p_a}\right) D_{H_2O_{eff}}} \tag{3.24}$$

$$\frac{di_{el}}{dx} = -A i_o \left[\frac{p_{r,H_2}}{p^i_{H_2}} exp\left(\frac{\beta n F V_{loss}}{RT}\right) - \frac{p_a - p_{r,H_2}}{p_a - p^i_{H_2}} exp\left(-(1-\beta)\frac{nFV_{loss}}{RT}\right)\right] \tag{3.25}$$

where p_a is the total pressure on the anode,

Eqs. (3.23), (3.24), and (3.25) are modified to account for the cathode in Eqs. (3.26), (3.27), and (3.28):

$$\frac{d^2V_{loss}}{dx^2} = \left(\rho_{el(eff)} + \rho_{io(eff)}\right) Ai_o \left[\frac{p_{r,O_2}}{p^i_{O_2}} exp\left(\frac{\beta nFV_{loss}}{RT}\right)\right. \tag{3.26}$$

$$\left. - \frac{p_a - p_{r,H_2}}{p_a - p^i_{H_2}} exp\left(-(1-\beta)\frac{nFV_{loss}}{RT}\right)\right]$$

$$\frac{dp_{r,H_2}}{dx} = -\frac{RT}{2F}\frac{i_{el}}{D_{O_{2(eff)}}}\left(\frac{p_c - \partial p_{r,O_2}}{p_c}\right) \tag{3.27}$$

$$\frac{di_{el}}{dx} = -Ai_o\left[\frac{p_{r,H_2}}{p^i_{H_2}} exp\left(\frac{\beta nFV_{loss}}{RT}\right) - \frac{p_a - p_{r,H_2}}{p_a - p^i_{H_2}} exp\left(-(1-\beta)\frac{nFV_{loss}}{RT}\right)\right] \tag{3.28}$$

The electrolyte of a SOFC is sandwiched between two electrodes and is made of ceramic materials, for example yttria-stabilized zirconia (YSZ). Let δ present the electrolyte thickness and ϑ_{ysz} is the conductivity of YSZ. Then, ohmic resistance of the electrolyte is determined by the following equation [66],

$$V_{ohm,elec} = \frac{I\delta}{\vartheta_{ysz}} \tag{3.29}$$

where I is the total current density, total current density is varied from 0 to 55000 A m^{-2} for cell level modeling. At 1173 K, $\vartheta_{ysz} = 8 \times 10^{-2}$ S/cm [66].

3.3 MODEL VALIDATION

This work focuses on the optimization of SOFC cell level performance with nonlinearly graded electrodes in order to compensate the adverse effect of reduced operating temperature. In the model validation, we adopted porous composite of Nickel (Ni)/YSZ for the anode, a Lanthanum Strontium Manganite (LSM)/YSZ composite for the cathode, and YSZ for the electrolyte. These materials were chosen based on the availability of material properties reported in the literature and our previous experimental works [67]. However, the developed modeling framework can also be applied to different SOFC material systems and configurations. By volumetric ratio, 40% Ni was mixed with 60% YSZ for the anode [68]. A volumetric composition of 20% LSM and 80% YSZ was used for the cathode [69]. For cell level performance simulation, 89% H_2 and 11% H_2O were used, while air was used as the oxidant [70]. Throughout the study, the air pressure was kept constant at 1 atm. The particle size of the SOFC graded electrode varied from 0.3 to 3 μm [3], and the porosity grading was in the range of 30% to 70%, similar to the ranges used by Ni *et al.* [41]. The boundary conditions of this coupled boundary value equation developed in the previous sections are summarized in Table 3.1. All model validation parameters are shown in

Table **3.2**. Numerical steps required to solve the coupled boundary value equation is shown in Figure 3.2.

Table 3.1. Boundary conditions for the anode and cathode

X=0	$\frac{dV_{loss}}{dx} = \rho_{el(eff)} i_{el}$	$i_{el} = I_t$	$P_{r,H2} = p^i_{H2}$
X=l	$\frac{dV_{loss}}{dx} = \rho_{io(eff)} i_{io}$		

Table 3.2. Values of model parameters used in this study

Model Parameter	Symbol	Value
Temperature (K)	T	1073
Total pressure on anode (Pa)	p_a	101300
Pressure of hydrogen (Pa) **[3]**	$p^i_{H_2}$	86105
Pressure of oxygen (Pa)	$p^i_{H_2O}$	21273

Electronic number fraction (unitless) **[47]**	n_{el}	0.36
Activation energy for anode (J mol^{-1}) **[71]**	E_a	1×10^5
Activation energy for cathode (J mol^{-1}) **[71]**	E_c	1.17×10^5
Thickness of anode (µm)	l_a	1000
Thickness of cathode (µm)	l_c	50
Electrolyte thickness (µm)	δ	25
Electronic conductor in anode (S m^{-1}) **[3, 47]**	σ_{el}	2×10^6
Coefficient for exchange current density (anode) (A m^{-2}) **[64]**	α_a	1.344×10^{10}
Coefficient for exchange current density (cathode) (A m^{-2}) **[64]**	α_c	2.051×10^9
Ionic conductor in anode (S m^{-1}) **[3, 47]**	σ_{io}	$3.44\times10^4\exp(-10300/T)$
Porosity (unitless)	ε	0.3
Electronic conductor in cathode (S m^{-1}) **[41]**	$\sigma_{el,c}$	1×10^4
Ionic conductor in cathode (S m^{-1}) **[41]**	$\sigma_{io,c}$	$3.44\times10^4\exp(-10300/T)$
Tortuosity (unitless) **[3]**	τ	2.8
Electrolyte resistance(Ω m^{-2}) **[72]**	R_e	1.3×10^{-5}
Number of electrons in reaction (unitless) **[3, 47, 73]**	n	1
Necking factor(unitless) **[47]**	γ	0.5
Symmetry factor (unitless) **[3, 47, 73]**	β	0.5
Faraday's constant (C mol^{-1})	F	96485
Gas constant (J $(mol*K)^{-1}$)	R	8.314

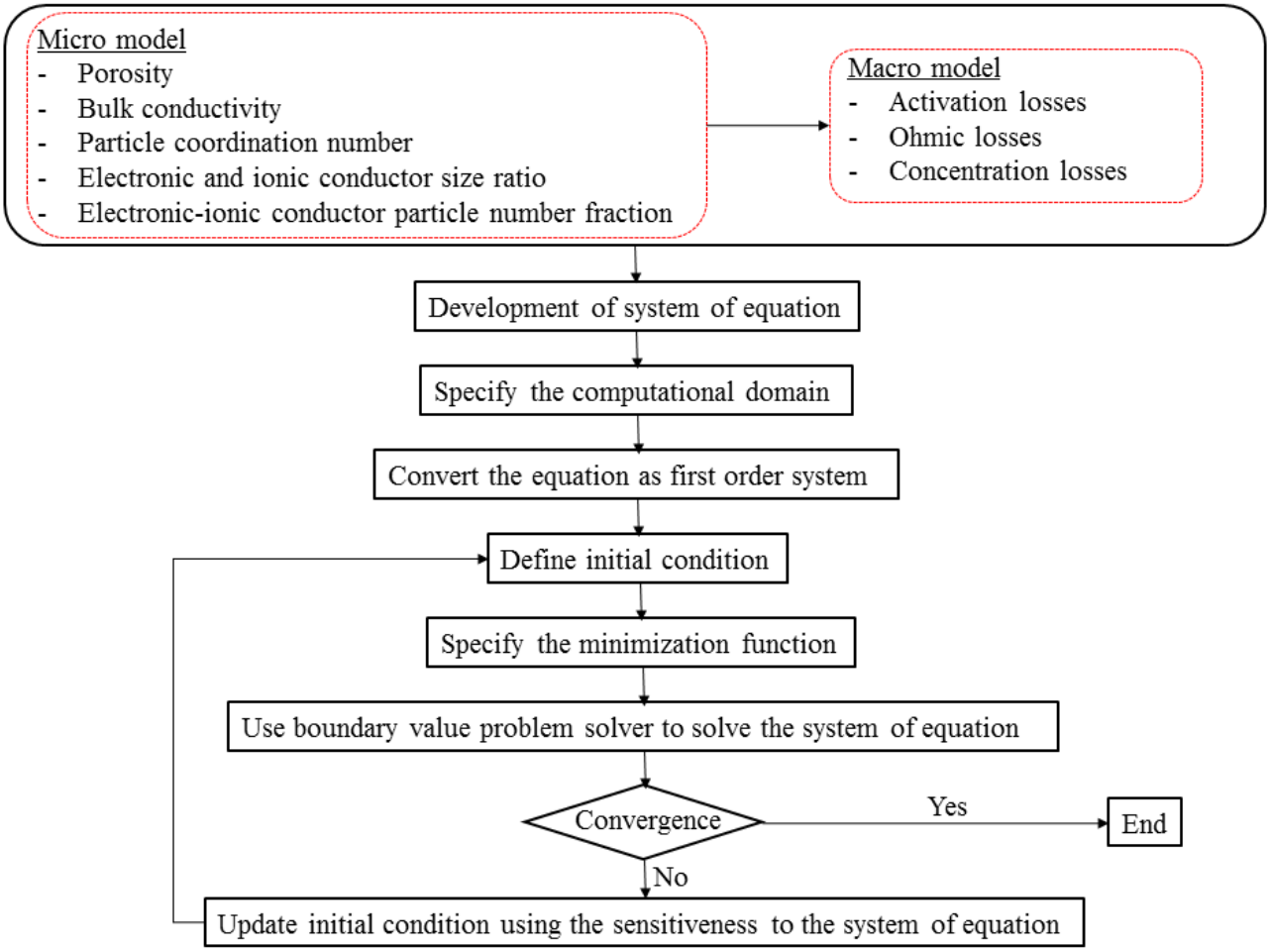

Figure 3.2. Numerical Flow Chart

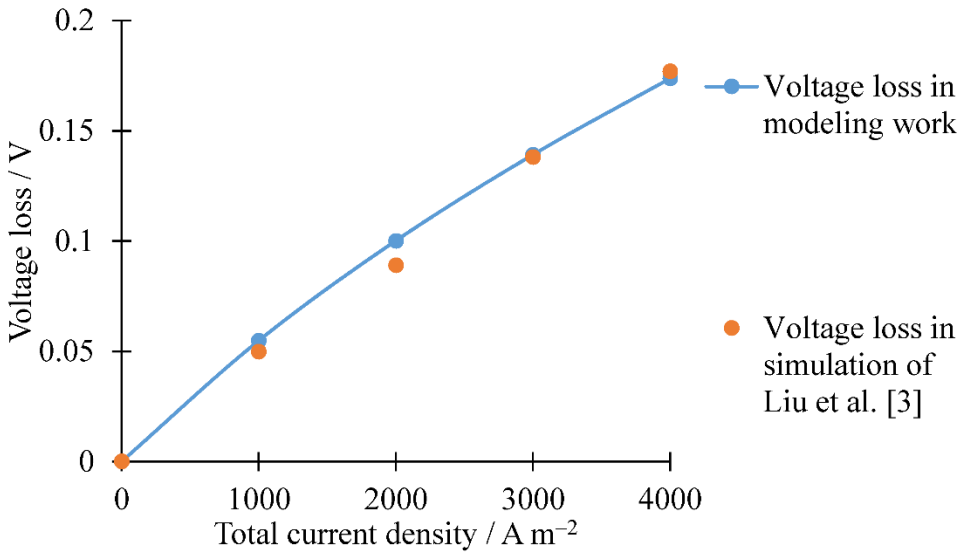

Figure 3.3. Comparison between model simulation and simulation results of Liu et al. [3]

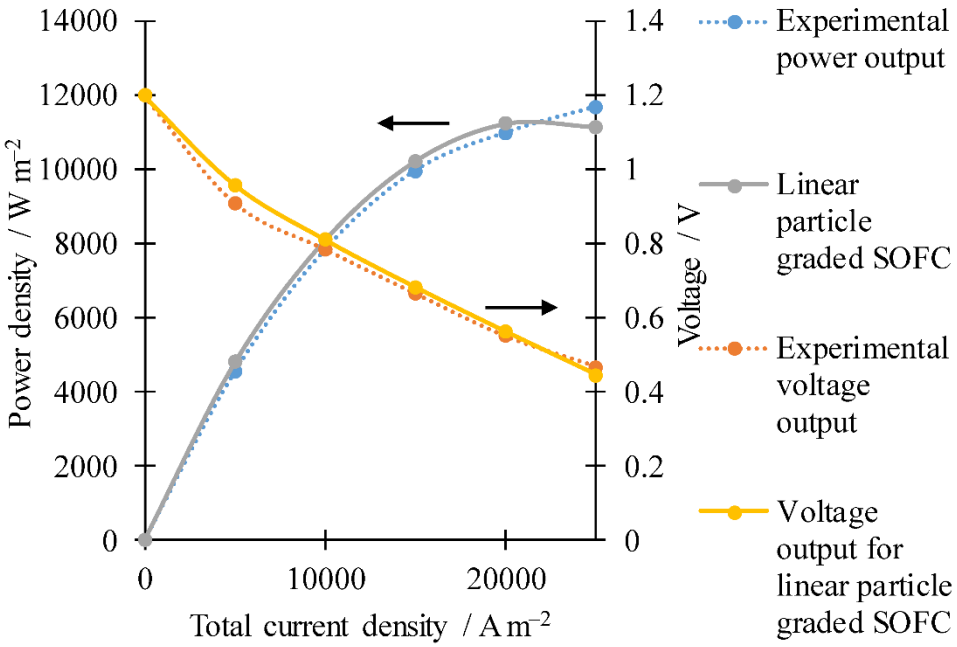

Figure 3.4. Comparison between model simulation and experimental data of Zhao et al. [35]

Simulation results from Liu *et al.* [3] were considered for the half-cell validation, as shown in Figure 3.3. For half- cell validation, the anode was considered with a thickness of 150 μm and porosity of 30%, as reported by Liu *et al.* [3]. Temperature and pressure were kept constant at 1073 K and 101325 Pa, respectively. Exchange current density is a fitting parameter varied from 1,000 to 6,500 A m^{-2}. Upon completion of the half-cell validation both the anode and cathode were considered for the complete cell model and the developed complete cell model is validated against the experimental work by Zhao *et al.* [74], see Figure 3.4. A reasonable fit is obtained at the operating temperature of 1073 K.

3.4 RESULTS AND DISCUSSION

In the following sections, we apply the validated model to analyze the effect of microstructural optimization on the performance improvement of SOFCs. Performance improvement on both conventional non-graded SOFCs and graded SOFCs are compared via applying different particle-size- and porosity-grading profiles in both anode and cathode. Then, a combination of particle-size and porosity grading are applied to grading both electrodes. The material system used in the model validation is applied here as well.

Figure 3.5 (a) shows the voltage loss for different anode- and electrolyte- thickness. For this study, we considered three different anode thickness of 1000 micron, 700 micron, and 500 micron. The voltage loss seems to be decreasing with the decrease of the anode thickness. This large thickness of anode influence both ohmic and concertation loss. Concentration polarization is related to the transport of gaseous species through porous electrodes and thus is related to the microstructure of

the electrodes, specifically the volume percent of porosity, the pore size, the tortuosity ratio, and finally the thickness of the electrode. On the other hand, the thickness of electrode also has a significant influence on ohmic loss due to the reduction of ionic conductivity. So the higher voltage loss was obtained due to high ohmic and concentration loss was driven by the higher thickness of components. Therefore, investigation needs to be done to reduce the voltage loss of SOFC. Comparison between different cathode materials at 873 k is shown in Figure 3.5 (b). This study considered three different cathode material LSM/YSZ composite, Lanthanum strontium cobalt ferrite (LSCF), and a composite of LSCF/*Gadolinium doped ceria (GDC).* The figure shows at low temperature the voltage loss of LSCF and LSCF/GDC composite exhibits better result compared to the LSM / YSZ composite cathode. However, LSM/YSZ composite cathode was chosen for the ready availability of material properties reported in the literature and our own experimental results.

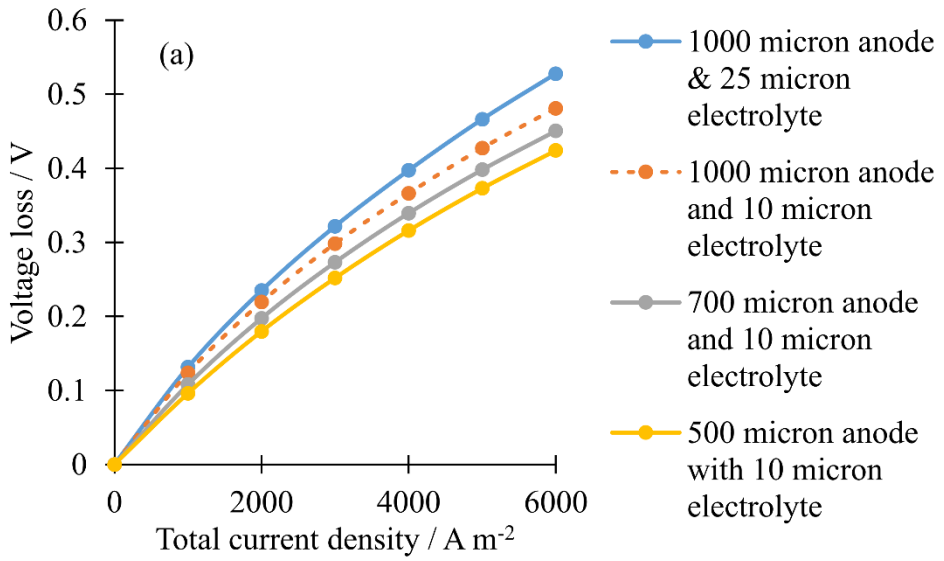

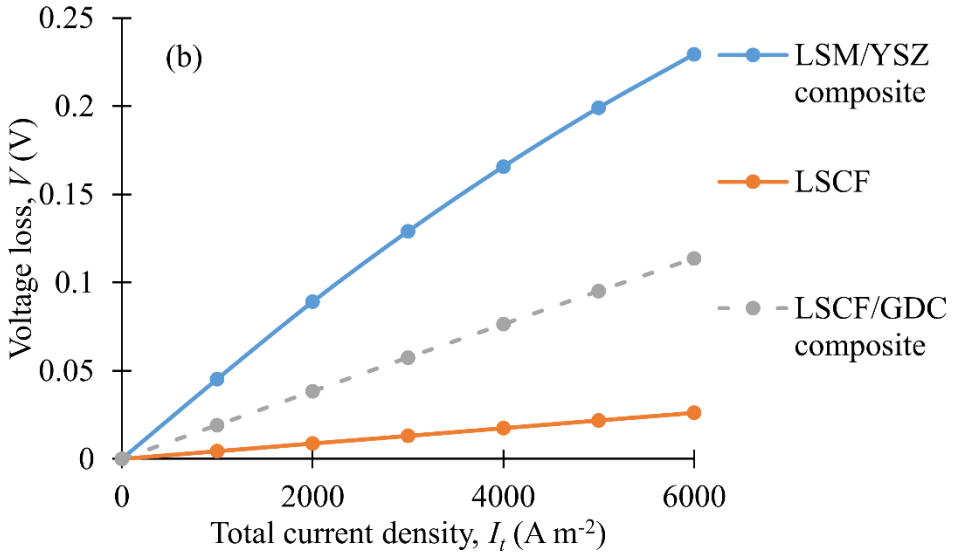

Figure 3.5. (a) Voltage loss for different SOFC components thickness, (b) voltage loss for different cathode material

At high current density, the thickness of the electrodes plays a critical role in determining voltage loss [41]. In Figure 3.6, we compare the voltage loss in both anode and cathode at different current densities for an anode-supported SOFC without microstructural optimization. It shows the voltage loss from anode side is higher compared with the cathode side at same current density. This is due to the configuration of the anode-supported structure with different thicknesses in both electrodes. In Figure 3.6, anode thickness of 1000 μm and cathode thickness of 50 μm are considered. As the anode shows considerable voltage loss, investigation needs to be done on the anode. However, cathodes are widely cited as being the limiting electrode in SOFC performance [75, 76], as shown in the Figure 3.6 cathode side shows higher voltage loss. Therefore, different grading profiles apply to both anode and cathode in order to increase the peak power density of SOFC. It has been shown in the literature that, successfully tailoring the microstructures of SOFC electrodes can effectively increase the peak power density by reducing voltage loss [3, 41].

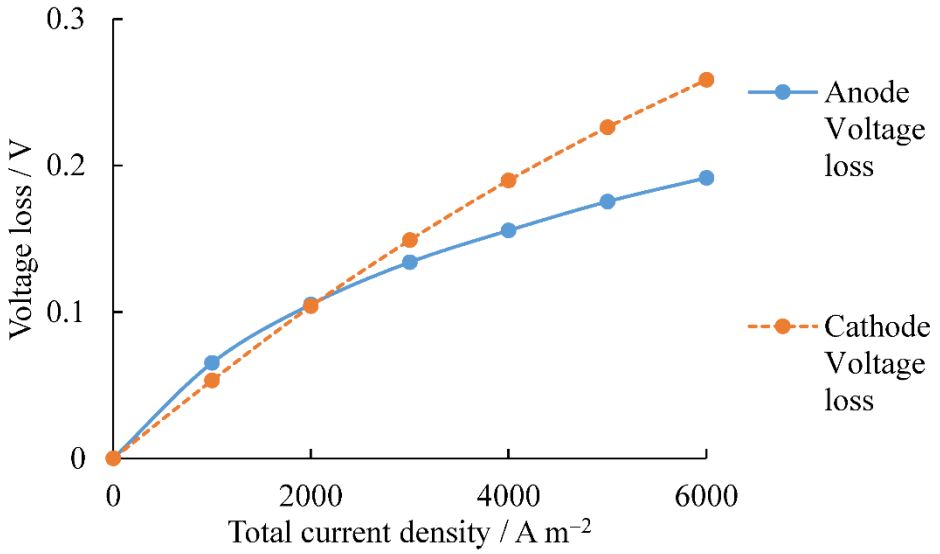

Figure 3.6. Comparison between anode (thickness of 1000 μm) and cathode (thickness of 50 μm) voltage losses as a function of total current density

In order to examine linear and nonlinear particle-size- and porosity-grading, we developed the following Eqs (3.30) and (3.31) [3, 49] to obtain different particle-size- and porosity-grading profiles, as illustrated in Figure 3.7.

$$d_p = \frac{(d_f - d_i)}{d_f}\left(\frac{(b^2 + lb)d_f}{l(x+b)} + d_f - \left(\frac{d_f(b^2+lb)}{lb}\right)\right) + d_i \tag{3.30}$$

$$d_p = \frac{(d_f - d_i)}{d_f}\left(\frac{(b^2 + lb)d_f}{l(x-l-b)} - d_f + \left(\frac{d_f(b^2+lb)}{lb}\right)\right) + d_f \tag{3.31}$$

where d_p represents the particle diameter, or porosity, b is the shape factor which determines the nonlinearity of the grading profile, d_f is the particle diameter, or porosity, at the free surface, and

d_i is the particle diameter, or porosity, at the interface between electrode and electrolyte. When b = 1, the grading profile is linear. If b < 1, the grading profile is nonlinear. Eq. (3.30) can generate any grading profile between the linear profile (b = 1) and a concave down profile (Figure 3.7 shows concave down profiles with dark blue and green lines) with b = 0.00001 [3, 49]. On the other hand, Eq. (3.31) can generate any grading profile between the linear profile (b = 1) and a concave up profile (Figure 3.7 represents concave up profile with orange and red lines) with b = 0.00001 [3, 49]. In this study, the grading profile using Eq. (3.30) and Eq. (3.31) have been implemented to examine nonlinear particle-size- and porosity-grading profiles.

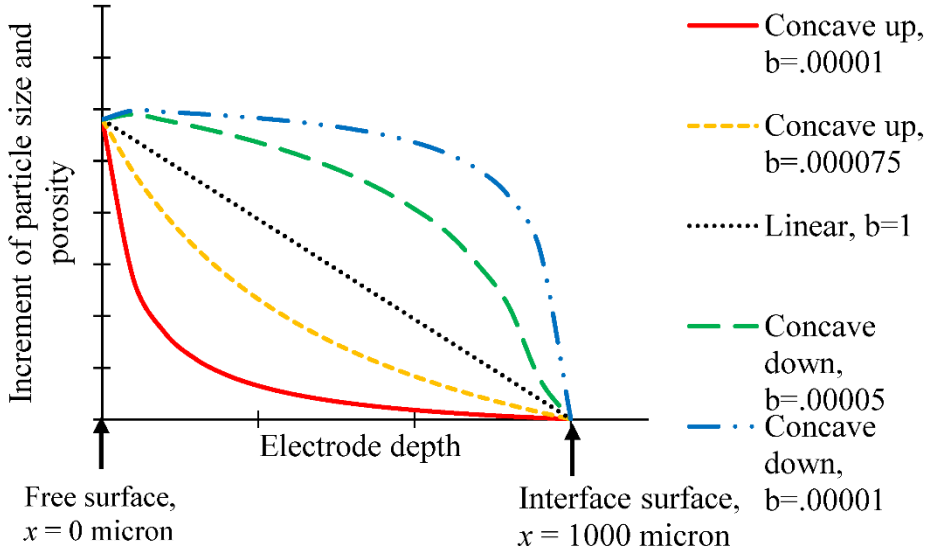

Figure 3.7. Particle size and porosity grading variations across the electrode as related to grading profile linearity

We investigate the effect of different grading profiles on both lowering SOFC voltage loss and increasing power density, as shown in Figure 3.8. In Figure 3.8, it shows that the particle size grading can positively influence the peak power density of an SOFC. The voltage losses in both

non-graded (i.e., homogeneous) electrodes and graded electrodes with different grading profiles are compared in Figure 3.8. Particle size varies from 0.3 to 3 μm (i.e., d_p = 0.3 μm @ x = 0 and d_p = 3 μm @ $x = l_a$ =1000 μm) and a shape factor, b = 0.00001 was used in the simulations shown in Figure 3.8. The result shows nonlinear electrode grading shows up to a 22% reduction in voltage loss over linear grading. This is caused by reduced concentration and activation loss with increased TPB area, which agrees with previous research [41]. In Figure 3.9, different shape factors related to the grading profile were used to determine a specific shape factor that can optimize the TPB area. Four different shape factors were applied and they are b = 0.00001 and b = 0.000075 for concave up particle-size grading and b = 0.00001 and b = 0.00005 for concave down particle-size grading. The results give a comprehensive comparison and were used to identify a shape factor which can maximize the power density. Figure 3.9 shows that peak power density for different shape factor and the maximum peak power density was achieved with concave down particle grading and a shape factor of 0.00001. The particle size at electrode free surface is 0.3 μm (x = 0) and is 3 μm ($x = l_a$ =1000 μm) at the electrode-electrolyte interface.

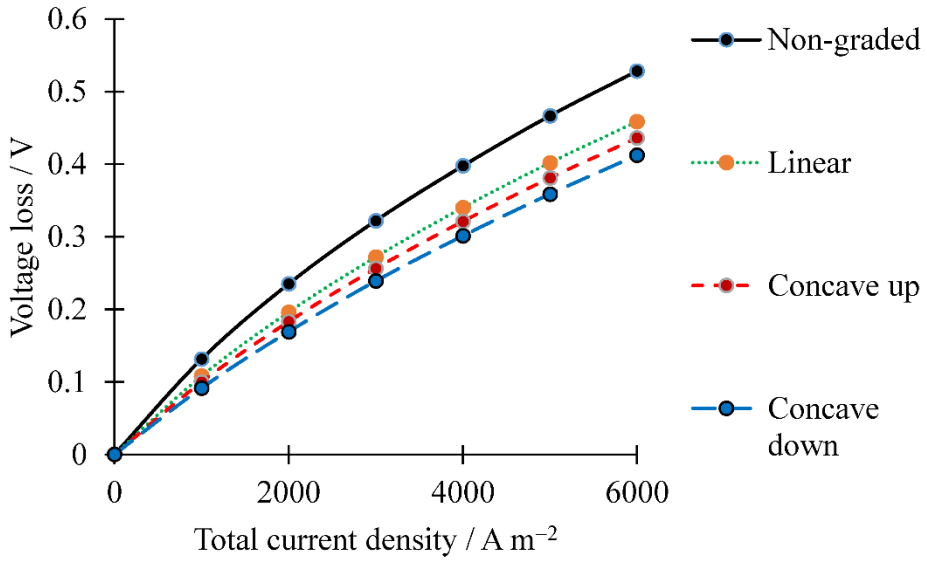

Figure 3.8. Voltage loss for 0.3 to 3 µm particle size grading range (for both concave up and concave down particle-size grading profiles with a shape factor b=0.00001)

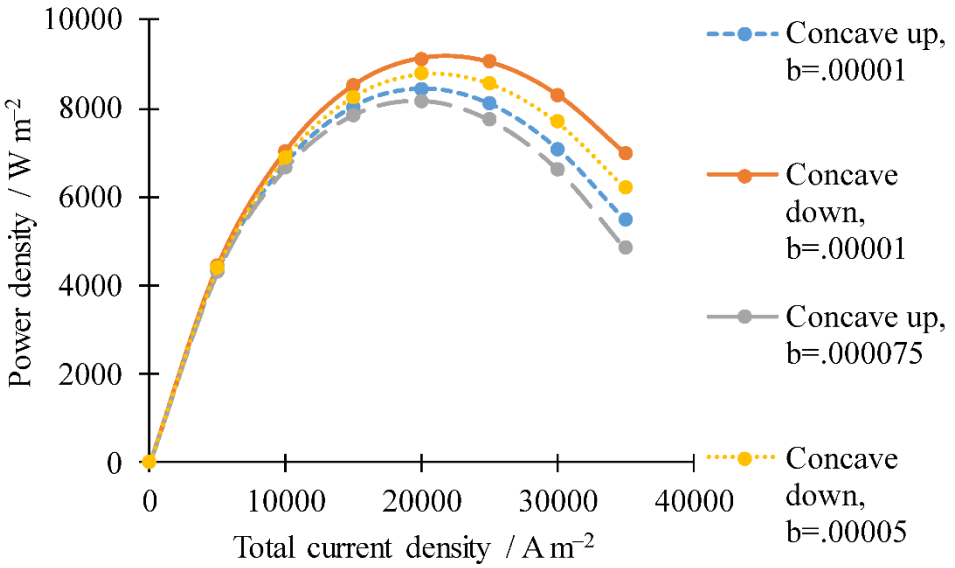

Figure 3.9. Power density curves for graded (0.3− 3 µm) electrode with different grading profiles

In Figure 3.10, the shape factor *b* was fixed to be 0.00001 for the nonlinear particle size grading. The particle size was varied from 0.3 µm (@ electrode free surface) to 3 µm (@ electrode/electrolyte interface). The peak power density obtained for the linear profile size is 7,778 W m^{-2}, while the peak power density for the concave down profile is 9,132 W m^{-2}. Thus, the maximum power density for the concave down profile is 17% higher than the linear profile.

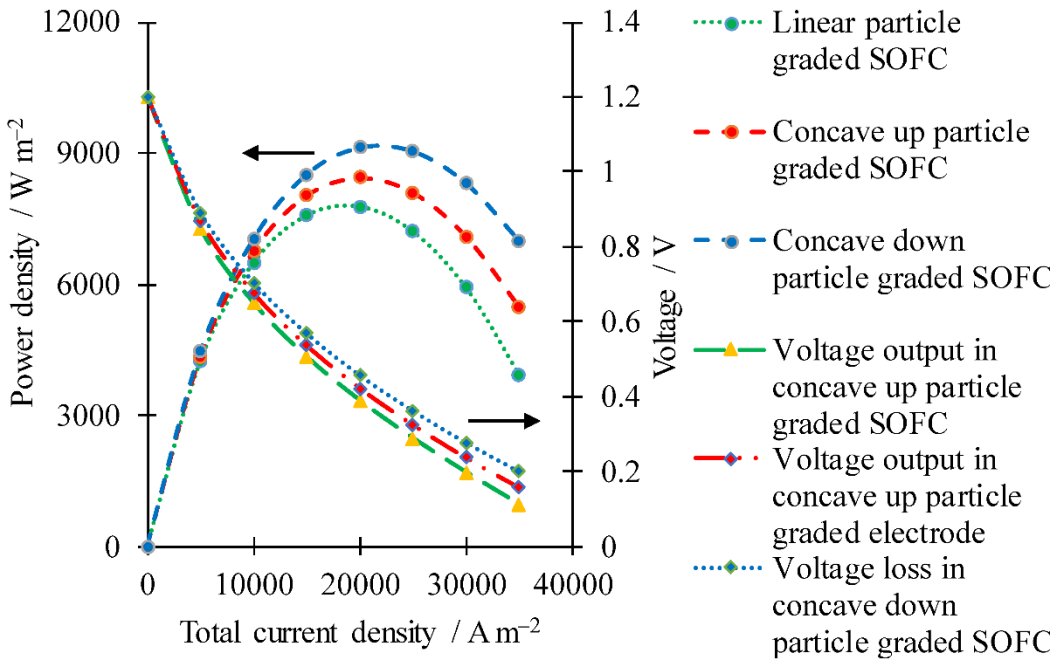

Figure 3.10. Comparison of voltage and power density curves for a linear (0.3−3 µm), concave up (0.3−3 µm) and concave down (0.3−3 µm) particle size graded electrodes (with a shape factor b=.00001)

Figure 3.11 shows the effect of the combination of nonlinear particle-size- and porosity-grading on the performance of SOFCs. The shape factor was considered to be 0.00001 for all grading profiles. The porosity was varied from 30% to 70% along the thickness of the electrode as well as applying particle size grading. The particle size varied from 0.3 to 3 µm. Electrodes with lower porosity have low diffusion coefficients due to the small pore size, which leads to the increased concentration loss [3]. So the application of porosity grading can further improve the peak power density by reducing concentration loss. However, increased porosity grading can also reduce the TPB area and lead to more activation loss. In order to mitigate this problem, both particle-size- and porosity-grading were applied simultaneously to the electrode microstructure.

The result shows peak power density is improved by 27% compared to the linearly graded SOFC, as seen in Figure 3.11.

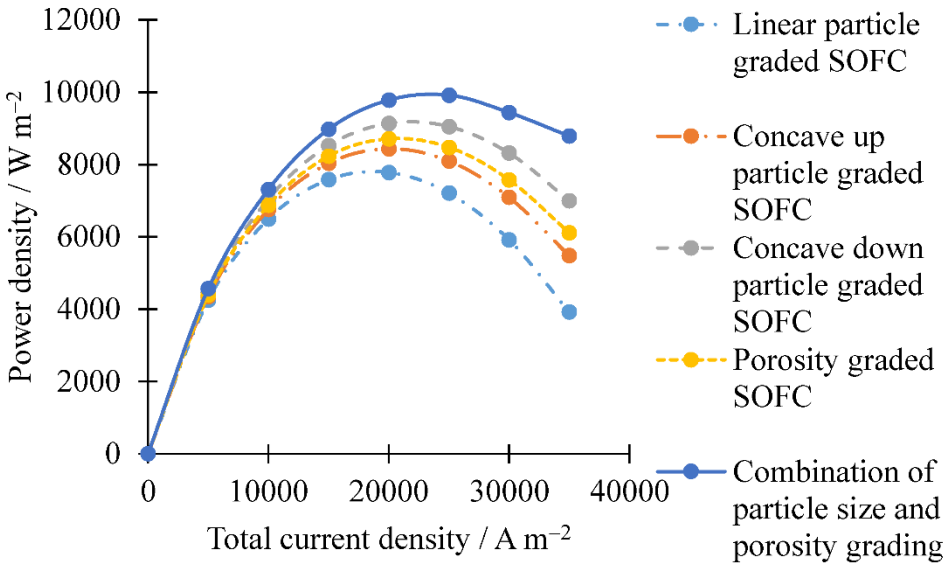

Figure 3.11. Comparison of power densities of SOFCs for linear (0.3−3 μm) and nonlinear (0.3−3 μm) particle graded electrodes (with a shape factor b=.00001) in combination with porosity gradient (30%−70%)

The power output of a SOFC tends to decrease with lower operating temperatures. To determine the peak power density, the OCV needs to be calculated. OCV of a SOFC is a function of temperature and can be determined with the following equation,

$$E = V_{oc}(T_0) + \frac{\Delta s}{n_e F}(T - T_0) \tag{3.32}$$

where V_{oc} is the OCV at 298 K (25°C), Δs is the change in entropy, and T_0 is 298 K. Different peak power densities of graded SOFCs at 1273 K, 1073 K, and 873 K are predicted and shown in

Figure 3.12. The peak power density is 7,778 Wm^{-2} at 1273 K, which tends to decrease as reducing operating temperature. Figure 3.12 shows, compared to operation at 1273 K, there is a 7.7% decrease in peak power density when the temperature is lowered to 1073 K and an even larger performance reduction of 13% when operating at 873K. The negative effect on the performance of SOFC is experienced at lower temperatures can be mitigated by utilizing the combination of nonlinear particle-size- and porosity-grading. The blue curve (i.e., the very top one) from Figure 3.12 plots the power density of a nonlinearly graded electrode at 873 K, the particle size is varied from 0.3 to 3 µm with a concave down grading profile of b = 0.00001, and porosity is varied from 30% to 70%. The peak power density of this electrode is found to be 8004 Wm^{-2}, which is 18.3% increase compared with the linearly graded electrode at the same temperature.

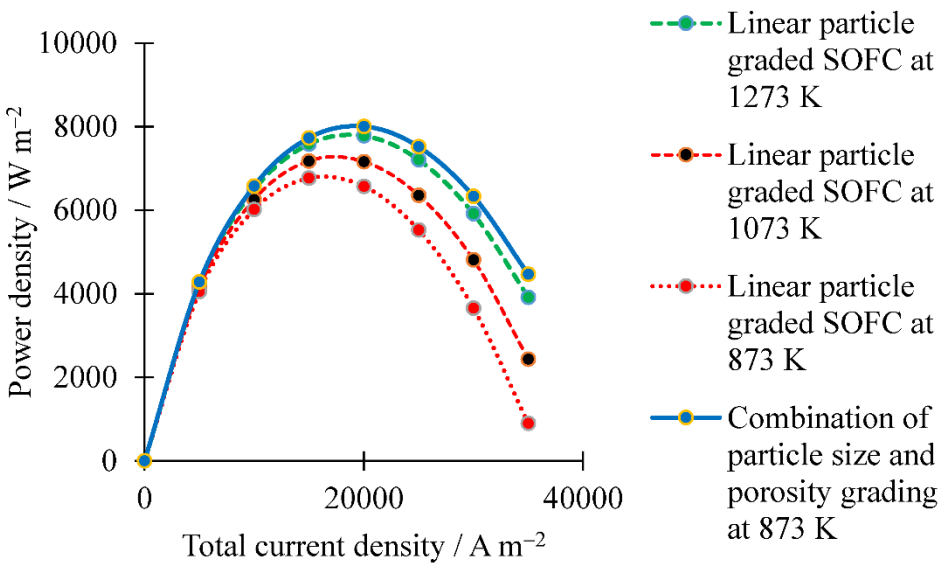

Figure 3.12. The effect of applying different grading profiles on peak power density at different temperatures.

3.5 CONCLUSION

In this work, a cell-level, multi-scale SOFC model is developed to investigate the effect of particle-size- and porosity-grading of both electrodes on reducing the operating temperature of SOFC. The model is validated against both simulation and experimental data reported in the literature. Optimization of the graded microstructure of SOFC electrodes increases TPB area and reduces the total voltage loss, which plays an important role in lowering the operating temperature of SOFC while maintaining its performance at high temperature. The simulation results show that the optimum particle size for achieving both a minimum voltage loss and a maximum power output is 0.3−3 μm. It is also found that the power output for a nonlinearly graded SOFC is 17% higher than that of a linearly graded SOFC. Moreover, the combination of nonlinear particle-size- and porosity-grading in the electrodes results in 27% improvement in peak power density. This demonstrates that a properly graded electrode can significantly reduce the adverse effect of lowering operating temperature and enable SOFCs to operate at a reduced temperature (as low as 873 K) while maintaining the performance at high temperature of 1273 K. However, further investigation is needed to reduce the ohmic loss by performing more sensitive analysis of different cell geometries and material systems.

3.6 APPENDIX

$D_{(eff)}$ can be obtained using binary and Knudsen diffusion models. Binary diffusion occurs where molecular-molecular interactions are dominant, and Knudsen diffusion occurs where molecular-surface interactions are dominant. The binary diffusion coefficient can be calculated using the

Chapman-Enskog theory, as seen in Eqs. (A-1) and (A-2) [60]. σ_{AB} is the collision diameter and Ω_{DAB} Ω_{DAB} is the collision integral based on the Lennard-Jones potential. The collision integral can be found in Eq. (A-2). M_{H_2} and $\mathrm{M_{H_2O}}$ are the molecular weights of hydrogen and water. The average energy well depth, in ergs, is calculated by: $\in_{H_2\text{-}H_2O} = (\in_{H_2} \in_{H_2O})^{0.5}$. $\in_{H_2}$ and $\in_{H_2O}$ are found from the viscosity of the gas [60]. The average collision diameter, Ω is calculated using $\sigma_{H_2-H_2O} = \frac{\sigma_{H_2} + \sigma_{H_2O}}{2}$. σ_{H_2} and $\mathrm{\sigma_{H_2O}}$ σ_{H_2O} are the collision diameters, in angstroms, of the individual species molecules [72].

$$D_{H_2-H_2O} = 0.0018583 \left(\frac{1}{M_{H_2}} + \frac{1}{M_{H_2O}} \right)^{\frac{1}{2}} \frac{T^{1.5}}{p_a \sigma_{H_2-H_2O}^2 \Omega_{D,H_2-H_2O}} \tag{A-1}$$

$$\Omega_{D,H_2-H_2O} = \frac{A}{(T^*)^B} + \frac{C}{exp(DT^*)} + \frac{E}{exp(FT^*)} + \frac{G}{\exp(HT^*)} \tag{A-2}$$

where $T^* = \frac{KT}{\in_{H_2\text{-}H_2O}}$, A = 1.06036, B = 0.15610, C = 0.19300, D = 0.47635, E = 1. 03587, F = 1.52996, G = 1.76474, H = 3.89411.

Knudsen diffusion conditions occur where the pore diameter is approximately 50 nm. As determined by [50, 55, 73], the Knudsen diffusion coefficient for a gas species A can be calculated by Eq. (A-3)

$$D_{AK} = 48.5 d_{pore} \sqrt{\frac{T}{M_A}} \tag{A-3}$$

where d_{pore} is the pore diameter.

The effective diffusion coefficient, $D_{A(eff)}$, can be found by Eq. (A-4),

$$D_{A(eff)} = \frac{\varepsilon}{\tau}\left(\frac{1}{D_{AB}} + \frac{1}{D_{AK}}\right)^{-1} \quad \text{(A-4)}$$

where ε and τ represent porosity and tortuosity of the porous structure, respectively.

3.7 LIST OF SYMBOLS

Greek letters

α	Coefficient for exchange current density
β	Symmetry factor, unitless
γ	Necking factor, unitless
ε	Porosity, unitless
θ	Contact angle, radians
ρ	Resistivity, ohm m
σ	Collision diameter, Å
τ	Tortuosity, unitless
φ	Volume fraction, unitless
Ω	Collision integral
ϑ_{ysz}	Conductivity of YSZ

Latin letters

A	Reaction area, $m^2\ m^{-3}$
b	Shape factor, unitless
d	Diameter, m
D	Diffusion coefficient, mol $m^{-2}\ s^{-1}$
E	Activation energy J mol^{-1}
F	Faraday's constant, C mol^{-1}
g	Gibbs free energy, J mol^{-1}
i_n	Charge transfer current density, A m^{-2}
i_o	Exchange current density, A m^{-2}
I	Total current, A m^{-2}
J	Molar flux, mol $m^{-2}\ s^{-1}$
l	Thickness of electrode, m
M	Molecular weight, g mol^{-1}
n_e	Number of electrons in reaction
n_{star}	Number of particle per volume
n_{el}	Number fraction of electronic particles, unitless
n_{io}	Number fraction of ionic particles, unitless
p	Pressure, Pa
pr	Probability of being in a percolation cluster, unitless
$part$	Particle size or porosity
r	Radius of particle, m
R_e	Electrolyte resistance Ω m^{-2}

R_g	Gas constant, J mol^{-1} K^{-1}
R_p	Particle size ratio, unitless
T	Temperature, K
V	Voltage, V
Z	Coordination number, unitless
Super script	
i	Inlet
Sub scripts	
a	Anode
A	Gas specie A
act	Activation
B	Gas specie B
c	Cathode
$conc$	Concentration
cr	Critical
e	Electrolyte
eff	Effective
el	Electronic
eq	Equilibrium
f	Free surface
H_2O	Water
H_2	Hydrogen
i	Interface at electrolyte

io	Ionic
K	Knudsen diffusion
loss	Loss
O_2	Oxygen
ohm	Ohmic
part	Particle
pore	Pore
r	Reaction site

3.8 REFERENCE

1. Abel, J., A. Kornyshev, and W. Lehnert, *Correlated resistor network study of porous solid oxide fuel cell anodes.* Journal of the Electrochemical Society, 1997. **144**(12): p. 4253-4259.
2. Aguiar, P., C.S. Adjiman, and N.P. Brandon, *Anode-supported intermediate temperature direct internal reforming solid oxide fuel cell. I: model-based steady-state performance.* Journal of Power Sources, 2004. **138**(1-2): p. 120-136.
3. Liu, L., et al., *Modeling of solid oxide fuel cells with particle size and porosity grading in anode electrode.* Fuel Cells, 2012. **12**(1): p. 97-108.
4. Abdullah, T. and L. Liu, *Peak Power Optimization of Solid Oxide Fuel Cells with Particle Size and Porosity Grading.* ECS Transactions, 2014. **61**(13): p. 33-46.
5. Liu, L., *Solid oxide fuel cell reliability and performance modeling and fabrication by spray pyrolysis.* 2011.

6. Liu, L., G.-Y. Kim, and A. Chandra. *Life Prediction of a Solid Oxide Fuel Cell Under Thermal Cycling Conditions*. in *ASME 2009 7th International Conference on Fuel Cell Science, Engineering and Technology*. 2009. American Society of Mechanical Engineers.

7. Wachsman, E.D. and K.T. Lee, *Lowering the temperature of solid oxide fuel cells.* Science, 2011. **334**(6058): p. 935-939.

8. de Souza, S., S.J. Visco, and L.C. De Jonghe, *Thin-film solid oxide fuel cell with high performance at low-temperature.* Solid State Ionics, 1997. **98**(1): p. 57-61.

9. Liu, L., G.-Y. Kim, and A. Chandra, *Modeling of thermal stresses and lifetime prediction of planar solid oxide fuel cell under thermal cycling conditions.* Journal of Power Sources, 2010. **195**(8): p. 2310-2318.

10. Fukui, T., et al., *Morphology control of Ni–YSZ cermet anode for lower temperature operation of SOFCs.* Journal of power sources, 2004. **125**(1): p. 17-21.

11. Kim, S.-D., et al., *Performance and durability of Ni-coated YSZ anodes for intermediate temperature solid oxide fuel cells.* Solid State Ionics, 2006. **177**(9): p. 931-938.

12. Inui, Y., et al., *Analytical investigation on cell temperature control method of planar solid oxide fuel cell.* Energy Conversion and Management, 2006. **47**(15): p. 2319-2328.

13. Fellet, M. and W. Rossner, *Ceramics improve operating conditions of solid-oxide fuel cells.* MRS Bulletin, 2015. **40**(03): p. 214-215.

14. Grew, K.N., A.S. Joshi, and W.K.S. Chiu, *Direct Internal Reformation and Mass Transport in the Solid Oxide Fuel Cell Anode: A Pore-scale Lattice Boltzmann Study with Detailed Reaction Kinetics.* Fuel Cells, 2010. **10**(6): p. 1143-1156.

15. Abdullah, T. and L. Liu, *Phase Field Simulation Coupling Microstructural Evolution and Crack Propagation during Performance Degradation of Solid Oxide Fuel Cells.* ECS Transactions, 2015. **66**(2): p. 207-217.

16. Liu, L., G.-Y. Kim, and A. Chandra, *Modeling of Ni–CGO anode in a solid oxide fuel cell deposited by spray pyrolysis.* Journal of Power Sources, 2012. **210**: p. 129-137.

17. Abdullah, T. and L. Liu, *Meso-Scale Phase-Field Modeling of Microstructural Evolution in Solid Oxide Fuel Cells.* Journal of The Electrochemical Society, 2016. **163**(7): p. F618-F625.

18. Gostovic, D., et al., *Three-dimensional reconstruction of porous LSCF cathodes.* Electrochemical and solid-state letters, 2007. **10**(12): p. B214-B217.

19. O'Hayre, R., D.M. Barnett, and F.B. Prinz, *The triple phase boundary a mathematical model and experimental investigations for fuel cells.* Journal of the Electrochemical Society, 2005. **152**(2): p. A439-A444.

20. Liu, L., G.-Y. Kim, and A. Chandra. *Deposition of Porous Anode Electrode of a Solid Oxide Fuel Cell by Ultrasonic Spray Pyrolysis*. in *ASME 2010 8th International Conference on Fuel Cell Science, Engineering and Technology*. 2010. American Society of Mechanical Engineers.

21. Golbert, J., C.S. Adjiman, and N.P. Brandon, *Microstructural modeling of solid oxide fuel cell anodes.* Industrial & Engineering Chemistry Research, 2008. **47**(20): p. 7693-7699.

22. Juhl, M., et al., *Performance/structure correlation for composite SOFC cathodes.* Journal of Power Sources, 1996. **61**(1): p. 173-181.

23. Suzuki, T., et al., *Impact of anode microstructure on solid oxide fuel cells.* Science, 2009. **325**(5942): p. 852-855.

24. Grosjean, A., et al., *Reactivity and diffusion between La 0.8 Sr 0.2 MnO 3 and ZrO 2 at interfaces in SOFC cores by TEM analyses on FIB samples.* Solid State Ionics, 2006. **177**(19): p. 1977-1980.

25. Liu, Y. and C. Jiao, *Microstructure degradation of an anode/electrolyte interface in SOFC studied by transmission electron microscopy.* Solid State Ionics, 2005. **176**(5): p. 435-442.

26. Kuriyama, K., et al., *Atomic force microscopy study of surface morphology change in spinel LiMn 2 O 4: possibility of direct observation of Jahn–Teller instability.* Surface science, 2007. **601**(10): p. 2256-2259.

27. Semenov, A., I. Borodina, and S. Garofalini, *In Situ Deposition and Ultrahigh Vacuum STM/AFM Study of V 2 O 5/Li3 PO 4 Interface in a Rechargeable Lithium-Ion Battery.* Journal of The Electrochemical Society, 2001. **148**(11): p. A1239-A1246.

28. Matsuo, Y., R. Kostecki, and F. McLarnon, *Surface Layer Formation on Thin-Film LiMn2 O 4 Electrodes at Elevated Temperatures.* Journal of The Electrochemical Society, 2001. **148**(7): p. A687-A692.

29. Kostecki, R. and F. McLarnon, *Nanometer-scale electrochemical lithography on the spinel oxide LiMn2O4.* Applied Physics Letters, 2000. **76**(18): p. 2535-2537.

30. Kostecki, R., et al., *Interfacial studies of a thin-film Li 2 Mn 4 O 9 electrode.* Electrochimica acta, 1999. **45**(1): p. 225-233.

31. Kushida, K. and K. Kuriyama, *Cyclic surface morphology change related to Li ion movement in Li secondary microbattery embedded in Si substrate: Atomic force microscopy studies.* Applied physics letters, 2004. **84**(18): p. 3456-3458.

32. Wilson, J.R., et al., *Three-dimensional reconstruction of a solid-oxide fuel-cell anode.* Nature materials, 2006. **5**(7): p. 541-544.

33. Smith, J., et al., *Evaluation of the relationship between cathode microstructure and electrochemical behavior for SOFCs.* Solid State Ionics, 2009. **180**(1): p. 90-98.

34. Holzer, L., et al., *FIB-Nanotomography of Particulate Systems—Part I: Particle Shape and Topology of Interfaces.* Journal of the American Ceramic Society, 2006. **89**(8): p. 2577-2585.

35. Arruda, T.M., et al., *Mapping irreversible electrochemical processes on the nanoscale: ionic phenomena in Li ion conductive glass ceramics.* Nano letters, 2011. **11**(10): p. 4161-4167.

36. Costamagna, P., P. Costa, and V. Antonucci, *Micro-modelling of solid oxide fuel cell electrodes.* Electrochimica Acta, 1998. **43**(3): p. 375-394.

37. Zhang, Y., C. Xia, and M. Ni, *Simulation of sintering kinetics and microstructure evolution of composite solid oxide fuel cells electrodes.* International journal of hydrogen energy, 2012. **37**(4): p. 3392-3402.

38. Zheng, K., et al., *On the tortuosity factor of solid phase in solid oxide fuel cell electrodes.* International Journal of Hydrogen Energy, 2015. **40**(1): p. 665-669.

39. Hussain, M., X. Li, and I. Dincer, *Mathematical modeling of planar solid oxide fuel cells.* Journal of Power Sources, 2006. **161**(2): p. 1012-1022.

40. Greene, E.S., W.K. Chiu, and M.G. Medeiros, *Mass transfer in graded microstructure solid oxide fuel cell electrodes.* Journal of Power Sources, 2006. **161**(1): p. 225-231.

41. Ni, M., M.K. Leung, and D.Y. Leung, *Micro-scale modelling of solid oxide fuel cells with micro-structurally graded electrodes.* Journal of Power Sources, 2007. **168**(2): p. 369-378.

42. Nam, J.H. and D.H. Jeon, *A comprehensive micro-scale model for transport and reaction in intermediate temperature solid oxide fuel cells.* Electrochimica Acta, 2006. **51**(17): p. 3446-3460.

43. Reszka, A.J., R.C. Snyder, and M.D. Gross, *Insights into the Design of SOFC Infiltrated Electrodes with Optimized Active TPB Density via Mechanistic Modeling.* Journal of The Electrochemical Society, 2014. **161**(12): p. F1176-F1183.

44. Duong, A.T. and D.R. Mumm, *Microstructural optimization by tailoring particle sizes for LSM-YSZ solid oxide fuel cell composite cathodes.* Journal of The Electrochemical Society, 2011. **159**(1): p. B39-B52.

45. Holtappels, P., et al., *Preparation of porosity–graded SOFC anode substrates.* Fuel Cells, 2006. **6**(2): p. 113-116.

46. Joshi, A.S., et al., *Lattice Boltzmann modeling of 2D gas transport in a solid oxide fuel cell anode.* Journal of Power Sources, 2007. **164**(2): p. 631-638.

47. Costamagna, P., P. Costa, and V. Antonucci, *Micro-modelling of solid oxide fuel cell electrodes.* Electrochimica Acta, 1998. **43**(3-4): p. 375-394.

48. Chan, S.H. and Z.T. Xia, *Anode micro model of solid oxide fuel cell.* Journal of the Electrochemical Society, 2001. **148**(4): p. A388-A394.

49. Flesner, R., *Modeling of Solid Oxide Fuel Cell functionally graded electrodes and a feasibility study of fabrication techniques for functionally graded electrodes.* 2009.

50. Suzuki, M. and T. Oshima, *Estimation of the Co-ordination number in a Multi-Component Mixture of Spheres.* Powder Technology, 1983. **35**(2): p. 159-166.

51. Chen, X., S. Chan, and K. Khor, *Simulation of a composite cathode in solid oxide fuel cells.* Electrochimica Acta, 2004. **49**(11): p. 1851-1861.

52. Chinda, P., et al., *Mathematical modeling of a solid oxide fuel cell with nearly spherical-shaped electrode particles.* Journal of sustainable energy and environment, 2010. **1**: p. 185-196.

53. Hines, A.L. and R.N. Maddox, *Mass transfer: fundamentals and applications*. Vol. 434. 1985: Prentice-Hall Englewood Cliffs, NJ.

54. Liu, L., et al., *Microstructural and electrochemical impedance study of nickel-Ce0.9Gd0.1O1.95 anodes for solid oxide fuel cells fabricated by ultrasonic spray pyrolysis.* Journal of Power Sources, 2011. **196**(6): p. 3026-3032.

55. Kuo, C.-H. and P.K. Gupta, *Rigidity and conductivity percolation thresholds in particulate composites.* Acta metallurgica et materialia, 1995. **43**(1): p. 397-403.

56. Greene, E.S., W.K.S. Chiu, and M.G. Medeiros, *Mass transfer in graded microstructure solid oxide fuel cell electrodes.* Journal of Power Sources, 2006. **161**(1): p. 225-231.

57. Colpan, C.O., I. Dincer, and F. Hamdullahpur, *A review on macro-level modeling of planar solid oxide fuel cells.* International Journal of Energy Research, 2008. **32**(4): p. 336-355.

58. Yoon, K.J., et al., *Polarization measurements on single-step co-fired solid oxide fuel cells (SOFCs).* Journal of Power Sources, 2007. **172**(1): p. 39-49.

59. Zhu, H. and R.J. Kee, *A general mathematical model for analyzing the performance of fuel-cell membrane-electrode assemblies.* Journal of Power Sources, 2003. **117**(1-2): p. 61-74.

60. Chan, S., K. Khor, and Z. Xia, *A complete polarization model of a solid oxide fuel cell and its sensitivity to the change of cell component thickness.* Journal of Power Sources, 2001. **93**(1): p. 130-140.

61. Noren, D. and M. Hoffman, *Clarifying the Butler–Volmer equation and related approximations for calculating activation losses in solid oxide fuel cell models.* Journal of Power Sources, 2005. **152**: p. 175-181.

62. Bergethon, P.R., *The physical basis of biochemistry: the foundations of molecular biophysics*. 2013: Springer Science & Business Media.

63. Guidelli, R., et al., *Defining the transfer coefficient in electrochemistry: An assessment (IUPAC Technical Report).* Pure and Applied Chemistry, 2014. **86**(2): p. 245-258.

64. Yang, S., et al., *Electrochemical analysis of an anode-supported SOFC.* Int. J. Electrochem. Sci, 2013. **8**(2): p. 2330-2344.

65. Ni, M., M.K. Leung, and D.Y. Leung, *Parametric study of solid oxide fuel cell performance.* Energy Conversion and Management, 2007. **48**(5): p. 1525-1535.

66. Barfod, R., et al., *Break down of losses in thin electrolyte SOFCs.* Fuel Cells, 2006. **6**(2): p. 141-145.

67. Liu, L., G.-Y. Kim, and A. Chandra, *Fabrication of solid oxide fuel cell anode electrode by spray pyrolysis.* Journal of Power Sources, 2010. **195**(20): p. 7046-7053.

68. Brown, M., S. Primdahl, and M. Mogensen, *Structure/Performance Relations for Ni/Yttria-Stabilized Zirconia Anodes for Solid Oxide Fuel Cells.* Journal of the Electrochemical Society, 2000. **147**(2): p. 475-485.

69. Holtappels, P. and C. Bagger, *Fabrication and performance of advanced multi-layer SOFC cathodes.* Journal of the European Ceramic Society, 2002. **22**(1): p. 41-48.

70. Singhal, S., *Advances in solid oxide fuel cell technology.* Solid state ionics, 2000. **135**(1): p. 305-313.

71. Campanari, S. and P. Iora, *Comparison of finite volume SOFC models for the simulation of a planar cell geometry*. Fuel Cells, 2005. **5**(1): p. 34-51.

72. Cussler, E.L., *Diffusion: mass transfer in fluid systems*. 2009: Cambridge university press.

73. Poling, B.E., et al., *The properties of gases and liquids*. Vol. 5. 2001: McGraw-Hill New York.

74. Zhao, F. and A.V. Virkar, *Dependence of polarization in anode-supported solid oxide fuel cells on various cell parameters.* Journal of Power Sources, 2005. **141**(1): p. 79-95.

75. Sholklapper, T.Z., et al., *LSM-infiltrated solid oxide fuel cell cathodes.* Electrochemical and Solid-State Letters, 2006. **9**(8): p. A376-A378.

76. Suzuki, T., et al., *Role of composite cathodes in single chamber SOFC.* Journal of the Electrochemical Society, 2004. **151**(10): p. A1678-A1682.

CHAPTER 4 . MESO-SCALE PHASE-FIELD MODELING OF MICROSTRUCTURAL EVOLUTION IN SOLID OXIDE FUEL CELLS[2]

4.1 INTRODUCTION

Solid oxide fuel cells (SOFCs) could be one possible solution to the depleting energy resources of the modern world due to its fuel flexibility, low carbon emissions, and high efficiency. With up to 60% energy efficiency and a life expectancy of 40,000 hours, the SOFC has emerged as an ideal candidate to meet the energy challenges of the modern world [1-3]. However, the commercialization of SOFC is hindered due to its high operating temperature, manufacturing cost, and structural instability [4-6]. Structural evolution of SOFC often leads to the structural failure and shortening of SOFC lifetime [7, 8]. Moreover, structural evolution results in compromising SOFCs' electrochemical performance, mostly in the electrodes.

An SOFC consists of both electrodes (i.e., anode and cathode) and a ceramic electrolyte. The anode is consisted of ion-conducting phase and electron-conducting phase to facilitate the fuel oxidation reaction [9]. The cathode reduces the oxygen into oxygen ion, which is then diffused to the anode through the ceramic electrolyte, such as yttria stabilized zirconia (YSZ) [10].

[2] Material in this chapter is a published paper: Abdullah, T. and L. Liu, "*Meso-Scale Phase-Field Modeling of Microstructural Evolution in Solid Oxide Fuel Cells",* Journal of The Electrochemical Society, 2016. **163**(7): p. F618-F625.

Electrochemical reaction of SOFC mainly occurs in the triple phase boundary (TPB) area [11], where the pore phase, the ion conducting phase, and electron-conducting phase join to convert chemical energy of fuel gases to electrical energy [1, 8, 12, 13]. TPB area is the key microstructural property controlling the electrochemical activities of SOFC [14]. It is desired to have a stable microstructure with optimized TPB area [15, 16]. However, recent studies reveal that TPB area is often diminished due to microstructure evolution [10, 17-20]. The microstructure evolution is controlled by the Ni particle coarsening, which in turn leads to the performance degradation and crack formation. Particle coarsening process was first reported by Ostwald *et al*. [21]. However, Ostwald ripening involves evaporation and condensation and controlled by the solubility of the droplet [22]. Gibbs-Thompson effect is often used to explain the particle coarsening phenomena [23] in the solid. Various experimental investigations explored the effects of Ni particle coarsening on the performance degradation of SOFC. For example, Tanasini *et al.* [24] revealed the performance degradation is directly related to Ni particle coarsening in the anode electrode. The experimental study by Simwonis *et al.* [25] showed that electrical conductivity of anode decreases due to Ni coarsening. Nelson *et al.* [26] reported TPB contiguity is affected by Ni particle coarsening. Faes *et al.* [27] investigated the interplay between particle size and TPB by measuring Ni-YSZ particle size and the TPB area using microscopy techniques. Experimental investigation by Iwata *et al.* [28] showed that the pore radius decreases due to Ni particle coarsening. Recent work by Cronin *et al*. [29] demonstrated that both pore percolation and TPB area are affected by Ni particle coarsening process.

Those aforementioned experimental investigations provide insight into the SOFC degradation process caused by Ni particle coarsening, however, the numerical model is required for theoretical

explanation of experimentally observed phenomena as well as evaluating SOFCs' performance in the long term. In this modeling work, the coarsening of Ni particle is considered as a capillarity-driven phenomena [30]. According to the Gibbs-Thomson effect, materials with high curvature regions have higher chemical potential than that of the lower curvature regions, this difference in chemical potential controls the transportation of materials from higher curvature regions to lower curvature regions this process is known as minimization of total free energy. In SOFCs, the modeling of the microstructural evolution is dependent on local interface mean curvature of Ni particle, which is driven by the process of minimization of total free energy of the system [25]. The total free energy function is governed by the dominant transport mechanism (i.e., surface- and volume-diffusion) of Ni particle [31]. Additionally, high operating temperature of SOFC leads to the enhanced mass transport of Ni particle [32]. During its operation, the surface diffusion coefficient of Ni particle is much higher than that of the YSZ particle, which essentially makes YSZ stationary or non-evolving compared to the Ni particle [33-35]. Moreover, the evolution of the microstructure leads to the pore size growth and the accumulation of expanded pores during the surface- and volume-diffusion, which causes crack formation [36]. However, it is quite challenging capturing microstructural evolution due to the explicit tracking of the interface moving boundaries.

To overcome the aforementioned issue, researchers have been applying the phase-field method for illustrating the variety of interfacial phenomena among different immiscible interfaces, microstructural evolution, and crack formation [30, 37, 38]. The phase-field method, which allows explicit tracking of the phase interfaces, has emerged as a powerful computational method for modeling transport phenomena and complex microstructural evolution process [9]. In addition, the

modeling approach allows visualizing the microstructural evolution in two- and three-dimensional [9]. The phase-field method separates an immiscible binary mixture into a domain pure in each component. It applies different orientation fields to defining the crystallographic orientations of Ni- and YSZ phases. The interfacial dynamics of the anode is defined by a variable called Order Parameter (OP) (i.e., phase-field variable). For instance, an OP $C = 0\ to\ 1$ can be used to indicate the domains of different constituents' particles, i.e., $C = 1$ indicates one particle phase while $C = 0$ denotes the other particle phase in an immiscible binary mixture. The interfacial region is tracked by $0 < C < 1$. The phase-field modeling approach has been successfully applied to explore the Ni particle coarsening associated with SOFCs evolution. For example, modeling work by Li *et al.* [9] revealed that TPB area is significantly reduced due to the microstructural evolution of SOFC. Chen *et al*. [30] quantitatively characterized the microstructural evolution by examining the TPB density, interfacial area, and tortuosity versus time using phase-field method. Abdeljawad *et al.* [19] established an integrated phase-field model coupling the analysis of the microstructural coarsening process with SOFC electrochemical performance evaluation of SOFC. Many researchers, including but not limited to Aranson *et al.* [39], Karma *et al.* [40], Mieche *et al.* [41], and Marconi *et al.* [42] have also explored crack formation using the phase-field model. Despite previous efforts, further investigation is yet to be done on the long-term degradation of SOFC caused by microstructural evolution, which has been identified as one of the major sources of SOFCs structural failure and performance degradation [19, 30]. Experimental investigation of SOFC electrodes degradation needs more further theoretical analysis [24]. In particular, a more comprehensive understanding is needed to investigate the interplay between the dynamics of microstructural evolution at the meso-scale and electrochemical performance at the macro-scale.

In this work, a meso-scale computational framework was established to investigate the quantitative effect of Ni particle coarsening on the performance of SOFC. An integrated phase-field model was developed to couple microstructure evolution and crack formation in the anode. The developed meso-scale model captures the dynamics of Ni particle coarsening and crack formation in Ni-YSZ anodes. Moreover, it tracks the evolution of microstructural features that influence the electrochemical performance. The time-dependent microstructural properties obtained from the phase-field model was applied as effective properties to our previously developed SOFC electrochemical model [1] to investigate the electrochemical performance of SOFC.

4.2 MODEL DEVELOPMENT

In this work, SOFC anode consists of three constituents, Ni particle, YSZ, and pore. The mass of each phase inside anode is assumed to be unchanged. The modeling approach is based on the minimization of the total free energy of the anode that is represented by F_{tot}. YSZ is assumed to be stationary due to slow diffusion compared to Ni that evolves via diffusion along Ni-pore interface. Three OPs are utilized to represent Ni phase (ζ), YSZ phase (ξ), and crack (ϑ), respectively. Based on the phase-field method, an OP changes continuously from 0 to 1 based on diffuse-interface theory. The range over which the OP changes from 0 to 1 is defined as interfacial region or interfacial thickness. For example,$\vartheta = 1$, $\vartheta = 0$, and $0 < \vartheta < 1$ represent the intact, fully broken, and the transitional interfacial thickness of the material. Minimization of total free energy leads to the interface diffusion. Interface diffusion can be formulated by using the Cahn Hilliard equation as follows,

$$\frac{\partial \zeta}{\partial t} = M\nabla^2\mu \tag{4.1}$$

where, *M* is the mobility function that depends on the OPs of the system, ∇^2 is the Laplace operator, and μ is the chemical potential of the system. The chemical potential is driven by total free energy that is based on dominant transport mechanism. The three phases of Ni-YSZ anode is considered immiscible, therefore, the effect of elastic energy is assumed to be negligible. F_{tot} represent the total free energy of the anode and can be expressed as follows,

$$F_{tot} = \int \left[\frac{\varphi^2}{2}|\nabla\zeta|^2 + f(\zeta) + f(\vartheta) + f(\sigma)\right] dV \tag{4.2}$$

where the first term on the right represents gradient energy, φ donates interfacial thickness, $f(\vartheta)$ is the fracture OP of anode, and $f(\sigma)$ is the elastic strain energy. *f(ζ)* is a generic double wall function that can be represented as follows,

$$f(\zeta) = \frac{\zeta^2(1-\zeta^2)}{4} \tag{4.3}$$

Two boundary conditions (i.e., contact angle at the TPB and no flux at the Ni-YSZ interface) are implemented with the Cahn-Hilliard equation. No flux BC (i.e., $\partial\mu \times \partial\zeta = 0$) can be solved using the smoothed boundary method (SBM) [43, 44]. The BC of contact angle is implemented as

elaborated in the literatures [45, 46]. The Cahn-Hilliard equation for anode within SBM framework can be written as follows,

$$\frac{\partial \zeta}{\partial t} = \nabla . M(\zeta, \xi) \nabla \mu = \nabla . \vec{\kappa} \tag{4.4}$$

where *M* is the mobility function of two OPs (i.e., ζ and ξ), $\vec{\kappa} = M(\zeta, \xi)\nabla\mu$.

The chemical potential of anode is denoted by μ and can be represented by the following equation [36],

$$\mu = \frac{\delta F_{tot}}{\delta \zeta} = f'(\zeta) - \varphi^2 \nabla^2 \zeta - g(\vartheta) \frac{1}{3} \frac{E\Omega}{1-2\upsilon} \zeta \varepsilon \tag{4.5}$$

where φ represents interfacial thickness, $g(\vartheta) = \vartheta^3(4 - 3\vartheta)$, is the coupling function between the fracture OP and elastic stress field. Karma *et al.* [40] showed the choice of $g(\vartheta)$ does not affect the transport mechanism as long as $g(\vartheta) = 0$. $\vartheta = 0$ represents the material is fully fractured. *E* is the Young's modulus, υ is the Poisson's ratio, and Ω is the volume fraction of Ni phase (i.e., ratio of Ni volume to total anode volume).

Multiplying with the OP ξ, Eq. (4.4) can be rewritten as follows,

$$\frac{\partial (\zeta \xi)}{\partial t} = \xi \nabla . \vec{\kappa} = \nabla . (\xi \vec{\kappa}) - \vec{\kappa} . \nabla \xi \tag{4.6}$$

Applying the no flux boundary condition, i.e., $\partial\mu \times \partial\zeta = 0$, into Eq. (4.6),

$$\frac{\partial(\zeta\xi)}{\partial t} = \xi\nabla.\vec{\kappa} = \nabla.(\xi\vec{\kappa}) \tag{4.7}$$

The unit normal vector of YSZ particle can be formulated as follows,

$$\vec{n} = \frac{\nabla\xi}{|\nabla\xi|} \tag{4.8}$$

Immiscible properties of Ni-YSZ controls the crystallographic orientation of the structure and is used to formulate the TPB contact angle θ,

$$\vec{n}\frac{\nabla\zeta}{|\nabla\zeta|} = \frac{\nabla\xi}{|\nabla\xi|}\frac{\nabla\zeta}{|\nabla\zeta|} = -\cos\theta \tag{4.9}$$

where the negative sign is due to the outward normal of the Ni particles.

The energy equilibrium at the TPB corresponds to an extremum of the total free energy, i.e., $\partial F_{tot} = 0$. Hence Eq. (4.2) can be written as follows,

$$|\nabla\zeta| = \frac{\sqrt{2[f(\zeta) + f(\vartheta) + f(\sigma)]}}{\varphi} \tag{4.10}$$

Eq. (4.9) can be formulated as follows,

$$\nabla\zeta.\nabla\xi = -|\nabla\xi|cos\theta\frac{\sqrt{2[f(\zeta) + f(\vartheta) + f(\sigma)]}}{\varphi} \tag{4.11}$$

The microstructural evolution governing equation can be defined as follows,

$$\frac{\partial(\zeta\xi)}{\partial t} = \nabla.\left\{\xi M\nabla\left[f_{\zeta} - \frac{\varphi^2}{\xi}\left(\nabla(\xi\nabla\zeta) + \frac{\sqrt{2[f(\zeta)+f(\vartheta)+f(\sigma)]}}{\varphi}cos\theta\right)\right]\right\} \tag{4.12}$$

In Eq. 4.12, *M* is the mobility function and can be formulated as follows,

$$M(\zeta,\xi) = M_{Ni-pore}\prod\nolimits_{C_l C_h}(\zeta)\left(\zeta^2(1-\zeta^2)\right)g(\xi) \tag{4.13}$$

where, *g(ξ)* is a function to control the Ni particle mobility near the TPB area, can be represented by a polynomial function [30] .

$$g(\xi) = \xi^6(10\xi^2 - 15\xi + 6) \tag{4.14}$$

The pores in anode are treated as pre-existing crack or initial cracks. Following the previous work [36], the governing equation for crack formation using fracture OP can be described as follows,

$$\frac{1}{\omega}\frac{\partial\vartheta}{\partial t} = \alpha\nabla^2\vartheta - 32H\vartheta(1-\vartheta)(1-2\vartheta) - 12\vartheta^2(1-\vartheta)(\sigma_{st}-\sigma) \tag{4.15}$$

where, ω is the relaxation constant [47] of fracture order parameter, α is gradient energy co-efficient, H is the energy barrier [48], σ_{st} is the elastic energy density, and σ is the threshold value strain [36].

The microstructural properties are expressed in non-dimensional units in order to allow the investigation with a wide range of particle size and particle size ratio. Suitable parameters of the mobility function are necessary for the effective calculation of the Ni particle coarsening process. Due to diffuse interface nature of the microstructure, it is necessary to get an asymptotic analysis of phase-field method for the normalization of time. Following the references [49, 50], an asymptotic analysis has been developed to measure the characteristic time (time normalization),

$$\tau = \frac{L^4 k_B T N_v}{\gamma_s D_s \delta_s} \tag{4.16}$$

where, L represents characteristic length scale of sample, k_B is the Boltzmann constant, T is the temperature, N_v is the atomic number density, δ_s is surface diffusin depth, γ_s is surface energy, and D_s is surface diffusivity.

4.3 NUMERICAL SETUP AND SOLVER FLOW

The simulations were carried out by solving governing Eqs. 12-15 in FeniCS, an open source finite element software. Numerical calculations were on the order of 884736 elements and required about 16 GB of RAM and 140 hrs of time when solved in parallel over seven cores on an Ubuntu Linux workstation with 24 3.4 GHz Intel Xeon processors. The numerical tolerance for convergence and tolerance for the Newton solver were both set to be 1×10^{-6}. The Newton

iterative solver was utilized due to nonlinear nature of the governing equations. An open-source multiplatform tool ParaView was used for data analysis and visualization. The numerical solver flow can be referred to Figure 4.1.

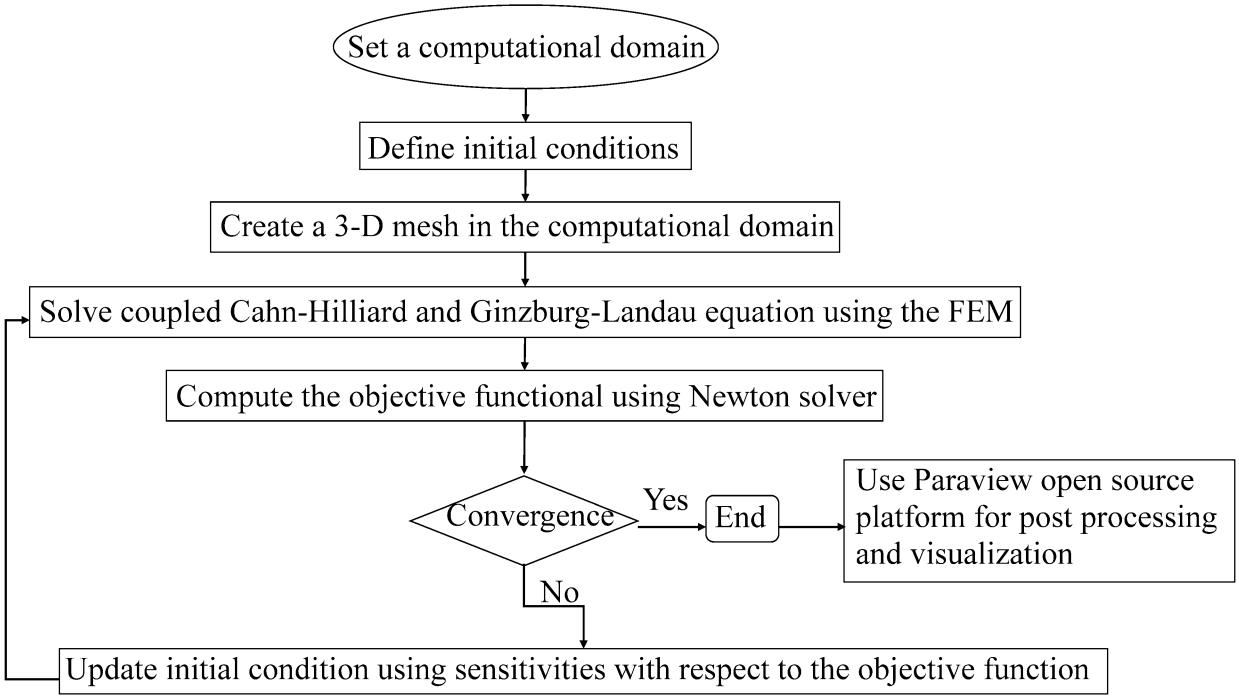

Figure 4.1. Numerical solver flow

4.4 MODEL VALIDATION

The work focuses on the modeling of microstructural evolution and crack formation in SOFC anode. Randomly disordered Ni-YSZ anode was adopted for the simulations due to the difficulty of obtaining initial crystallographic orientation. Ni particle size of 0.55 μm and Ni-YSZ particle size ratio of 0.9 were used as initial values. Time step size for simulation represented one-hour operation in real time. The mobility for Cahn-Hilliard equation was taken as one. Simulation

results show 26% increment in the Ni particle size after 1000 time steps, which agrees with the experimental result reported by Tanasini *et al.* [24]. Additionally, the particle size ratio of Ni-YSZ was decreased by 16%, while Tanasini *et al.* [24] reported 14.6% decrement based on their experimental study. Figure 4.2 shows the comparison between the experimental and modeling work for both particle size and particle size ratio. Comparison of TPB evolution shows a close match with the literature from Li *et al.* [9]. As for the volume ratios of three different phases, we used 30% Ni phase, 30% YSZ phase, and 40% porosity to validate the simulation result obtained from the modeling work. Figure 4.3 shows a close match between the two simulation results for TPB fraction (i.e., TPB fraction is defined as the ratio between TPB volume and anode volume). The TPB area is calculated using the ParaView. The key model parameters and values are listed in Table 4.1.

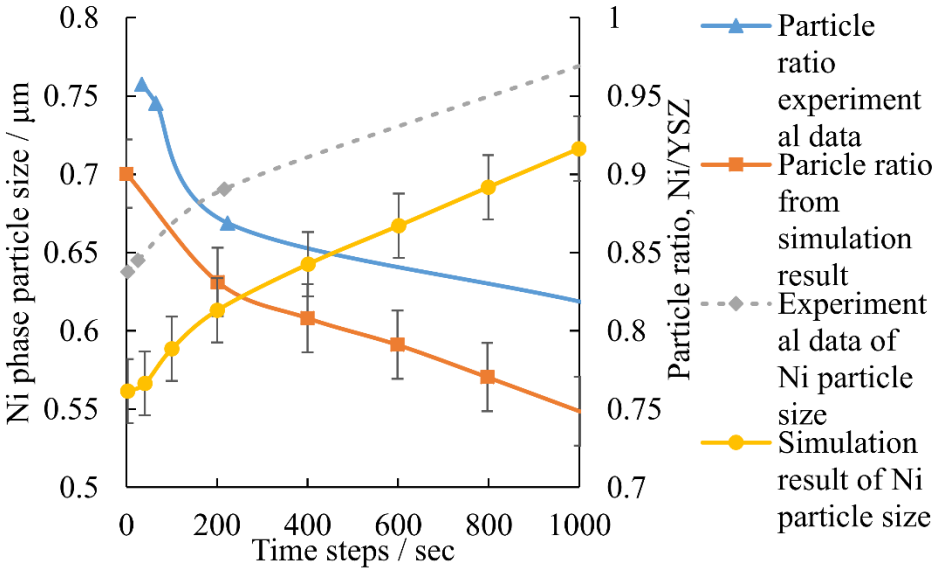

Figure 4.2. Comparison between model simulation and experimental data by Tanasini et al. (24)

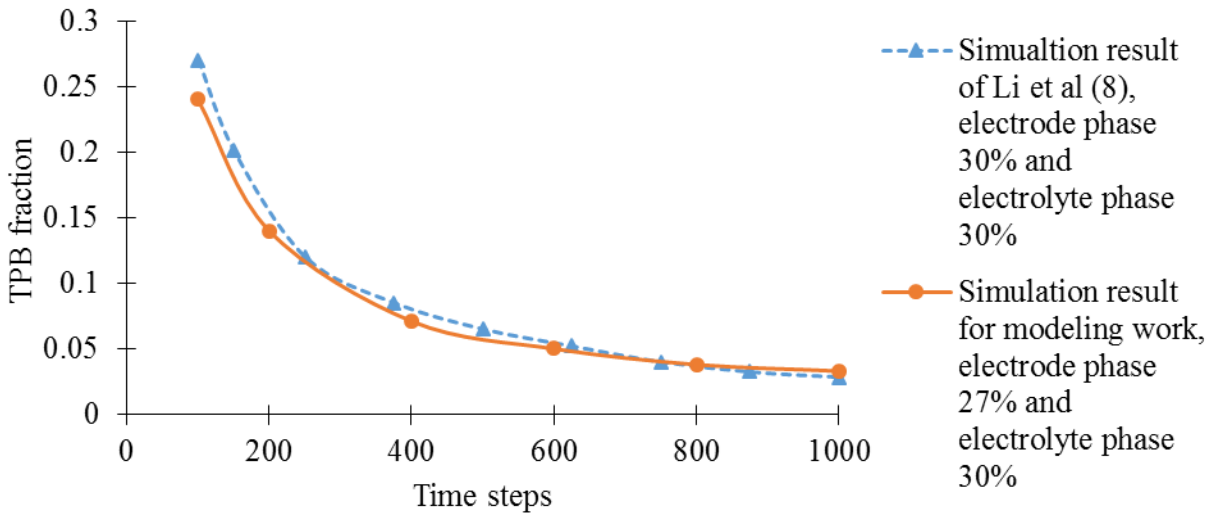

Figure 4.3. Comparison of temporal evolution simulation of TPB fraction with Li et al.(9)

Table 4.1. Values of model parameters used in this study

Model parameter		Value
Elastic constant, *GPa* (57)	E	200
Partial molar volume, m^3/mol (57)	Ω	6.63×10^{-6}
Poisson ratio (58)	P	0.3
Energy barrier, J/m^3 (43)	H	5
Threshold strain, (51, 52)	ε	0.002
Characteristic length, *m*	φ	25×10^{-6}
Relaxation constant (59)	ω	0.3
Surface energy, $J\ m^{-2}$ (30)	γ_s	1.9
Surface diffusion co-efficient, $m^2\ s^{-1}$ (30)	D_s	10^{-6}
Interfacial thickness, *nm* (30)	δ_s	1
Boltzmann constant, $m^2\ kg\ s^{-2}\ K^{-1}$ (30)	k_B	1.38×10^{-23}

4.5 RESULT AND DISCUSSION

In this work, the developed meso-scale phase-field model was applied to investigate the anode microstructural evolution and crack formation. The SOFC anode microstructure evolution is driven by the Ni particle coarsening process, which leads to TPB area reduction, long term performance degradation, and crack formation of SOFC. The developed model was also used to obtain the time-dependent microstructural properties during microstructure evolution, which is later used to quantify the performance degradation of SOFC.

The temporal microstructural evolution in two-dimensional is shown in Figure 4.4. A randomly disordered microstructure is generated in a normalized domain, where blue color represents the Ni particle, green color represents the YSZ, and red color is the pore, to explore the microstructural evolution process. During SOFC operation, the anode evolves over time due to coarsening of Ni particle. Due to the nature of the diffusive interface, YSZ-pore phase interface and Ni-pore interface can be tracked with obtaining their microstructural parameters (e.g., particle size ratio, TPB fraction) by solving governing Eqs. 44-47. This particle coarsening process is driven by the minimization of total free energy, which causes average particle size to increase and the number of particles to decrease. Two different stages of microstructures at T=40 (i.e., 40 hrs operation) and T=1000 (i.e., 1000 hrs operation) are shown in the figure.

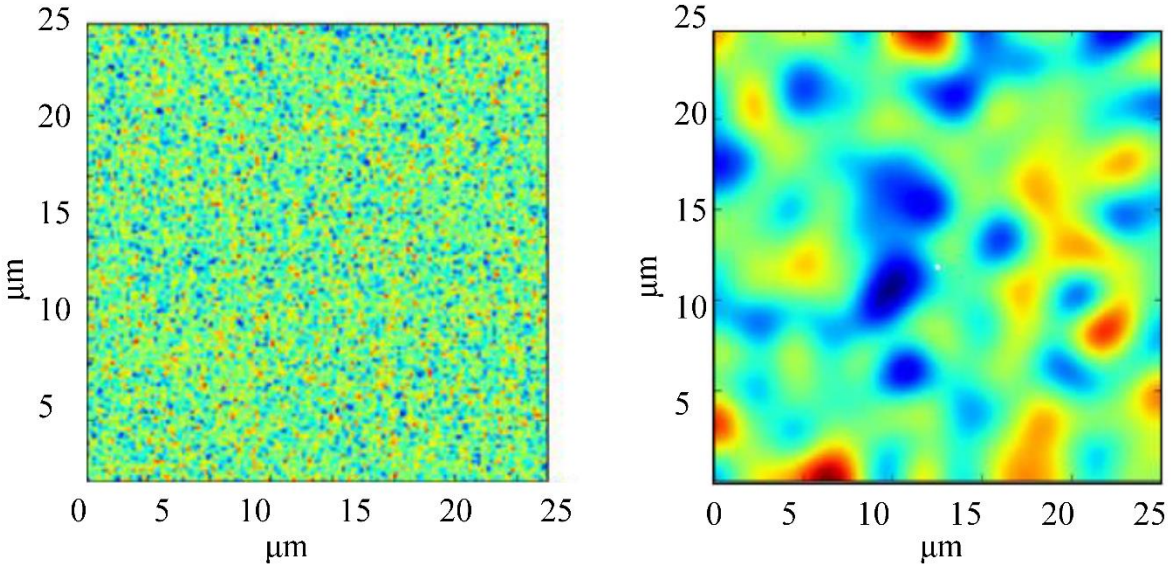

(a) T=40 (b) T=1000

Figure 4.4. Microstructural evolution at different time steps of SOFC anode, where Blue, yellow, and red represent the Ni, YSZ, and pore, respectively

The temporal three-dimensional structural simulations are completed for an anode microstructure of $25\ \mu m \times 25\ \mu m \times 25\ \mu m$ with a mesh grid of $96 \times 96 \times 96$. The Ni-YSZ microstructure was generated following a previous study, where three phase volume fraction was prescribed as 27% Ni phase, 30% YSZ phase, and 43% pore phase [30]. Figure 4.5 shows temporal three-dimensional microstructural evolution for Ni, YSZ, and pore after 1000 hours of operation. Each of the constituents' phases is shown in Figure 4.5. The simulation results show the internal structure of the connectivity of each phase, which can be utilized to quantify the growth of the average characteristic length and discriminate the percolated cluster from isolated clusters in the evolved anode.

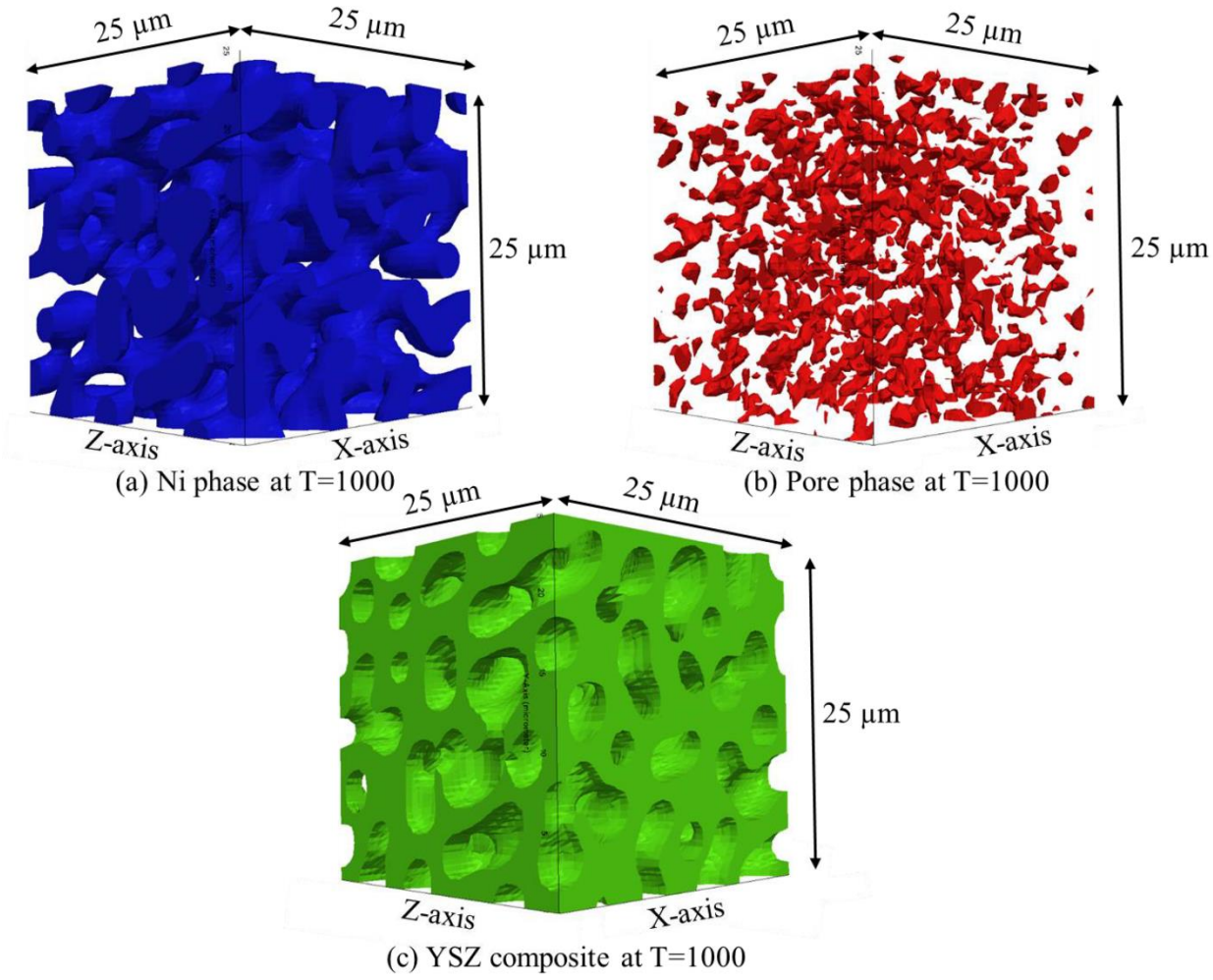

Figure 4.5. Temporal evolution of the three phases associated with the anode system of SOFC, at T=1000

Ni particle coarsening decreases TPB density and increases the resistance of anode. Figure 4.6 visualizes the reduction of the TPB area during the microstructural evolution process. The result shows rapid reduction of TPB area at the initial stage of the coarsening process, which agrees with the experimental observation where the main performance change occurs at the initial stages. Due to high interfacial energy at the initial stages, the TPB area decreases rapidly, but it slows down over the time period. The TPB area reduction is consistent with the temporal phase

coarsening, which indicates the performance degradation is directly related to the particle agglomeration and coarsening of Ni particle. The overall TPB area reduction is found to be approximately 24%, which is close to the experimental work of Cronin *et al.* [29].

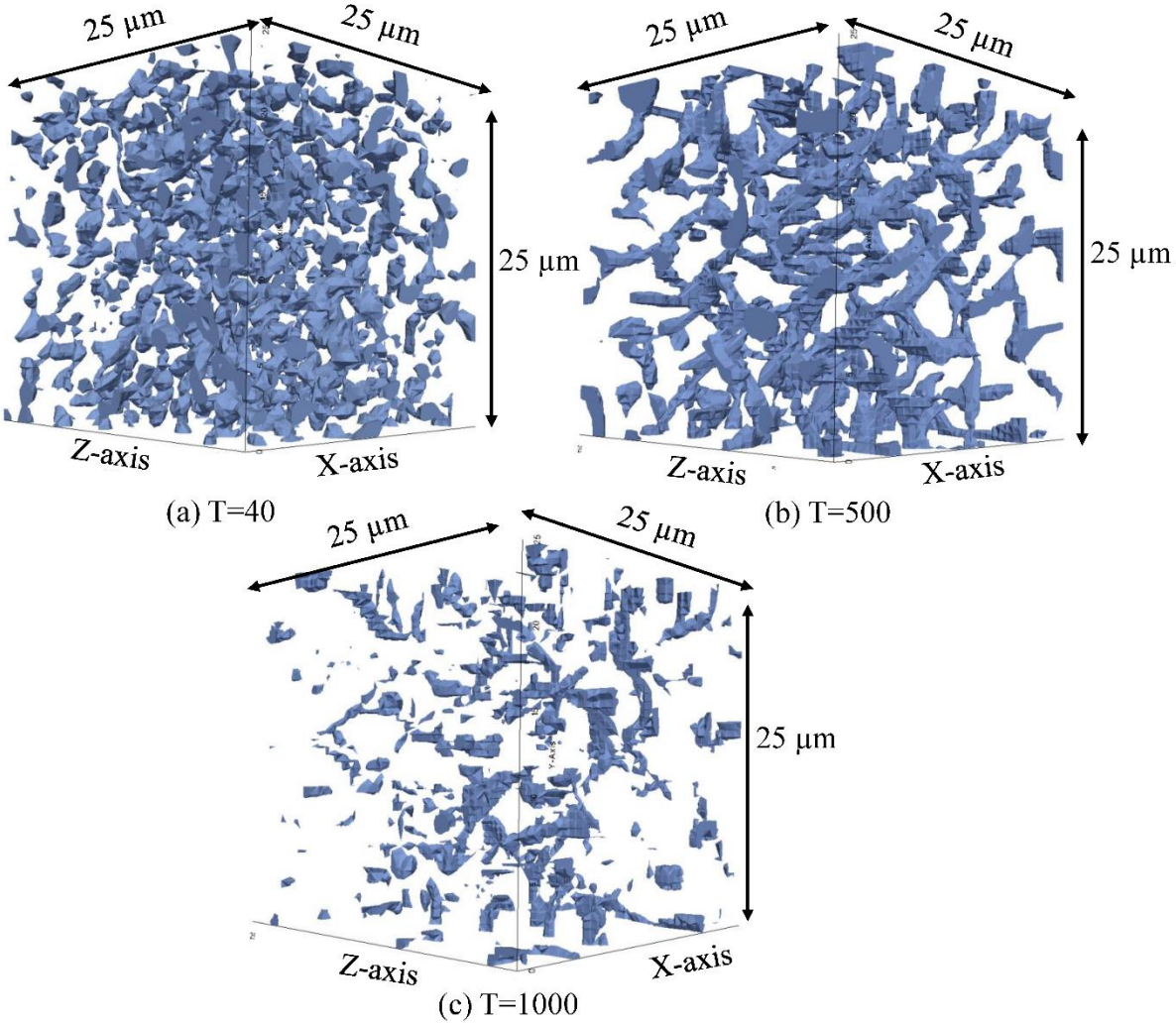

Figure 4.6. Degradation of TPB during temporal evolution of three phase SOFC electrode at three different dimensionless time steps. (a) Time step=40; (b) Time step=500; (c) Time step=1000 where the volume fractions are 27% Ni phase, 30% YSZ phase, and 43% pore phase at the initial stage.

The evolution of pore phase has been illustrated in Figure 4.7. Numerous pores exist in the anode to facilitate gas transportation. Pre-existing pores in Ni-YSZ grow due to interface diffusion during anode microstructure evolution which results in the increase of pore radius. By examining the evolution of pore phase, it can be concluded that the pores are growing in size and evolving into a round shape, thus minimizing total free energy. The coupling effect of diffuse interface and stress evolution plays a vital role in the formation of cracks. The radius of the pore increases during the minimization of interfacial area. The interface diffusion during the evolution process leads to the accumulation of these expanded pores which causes crack formation. In the meanwhile, as Ni particle diffuses during microstructural evolution, the tensile stress field in the inner region evolves, which causes stress concentration at the crack tip. The stress concentration eventually leads to the formation of crack and subsequently structural failure. The simulation results are in good agreement with annealing experiments on Ni-YSZ anodes with Ni and YSZ particles of similar sizes, where a 25% decrease in total Ni-pore interfacial area was observed [24].

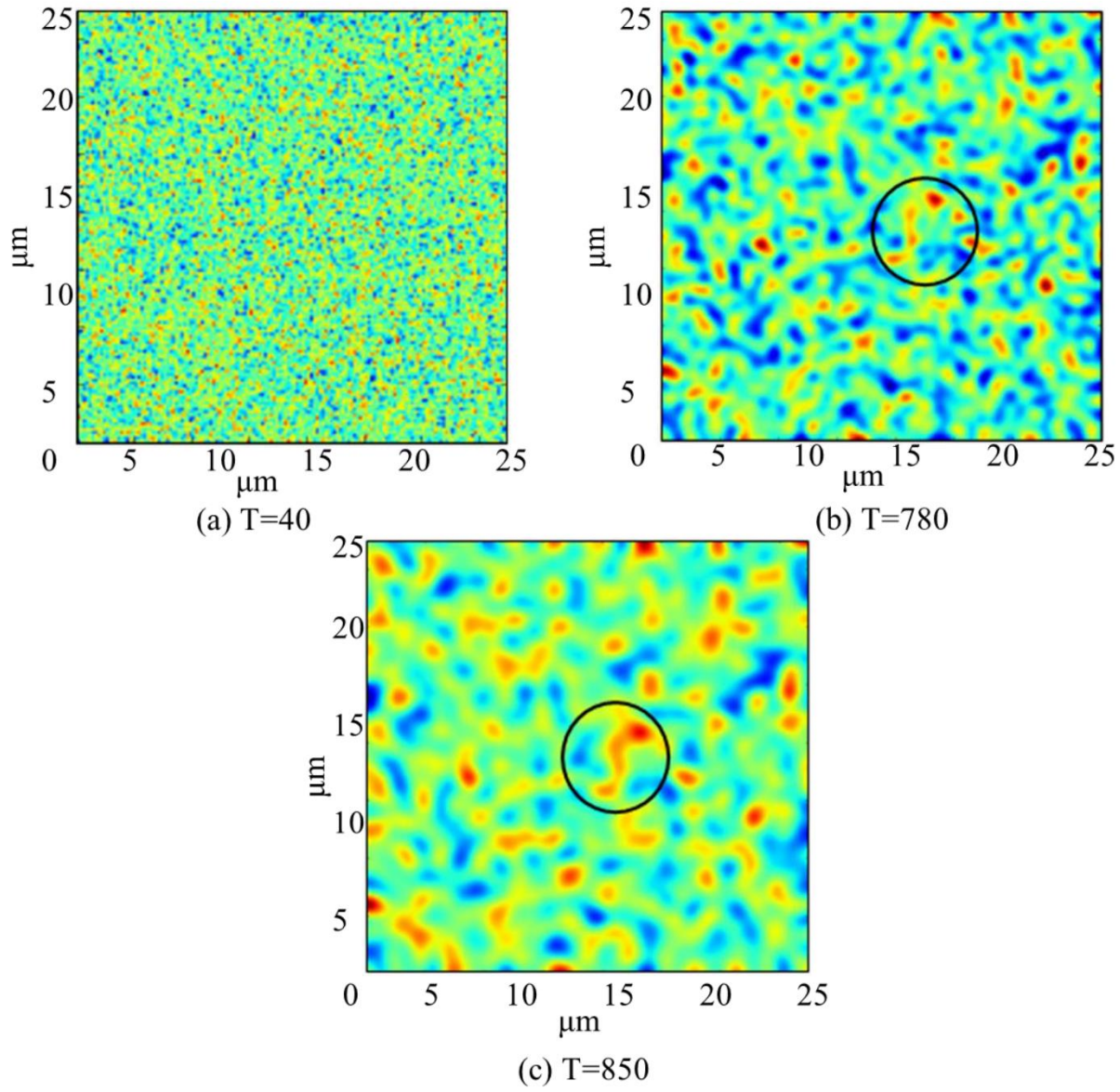

Figure 4.7. Propagation of crack in the microstructure due to interface diffusion. (a) Blue, yellow, and red represent the Ni, YSZ, and pore, respectively at T=40; (b) Formation of initial crack in microstructure at T=780; (c) Propagation of crack due to the coupling effect of interface diffusion and stress evolution at T=850.

The temporal pore phase evolution is presented in Figure 4.8, which helps to visualize the crack formation during microstructural evolution in three-dimension. Only the pore phase after the

evolution is shown for an anode microstructure of $25\ \mu m \times 25\ \mu m \times 25\ \mu m$ with a mesh grid of $96 \times 96 \times 96$ to demonstrate crack formation. In the modeling work, the initial crack appears after 780 dimensionless time steps. Then, the crack formation develops quickly, as shown in Figure 4.8, at two different dimensionless time steps, T=40 and T=1000.

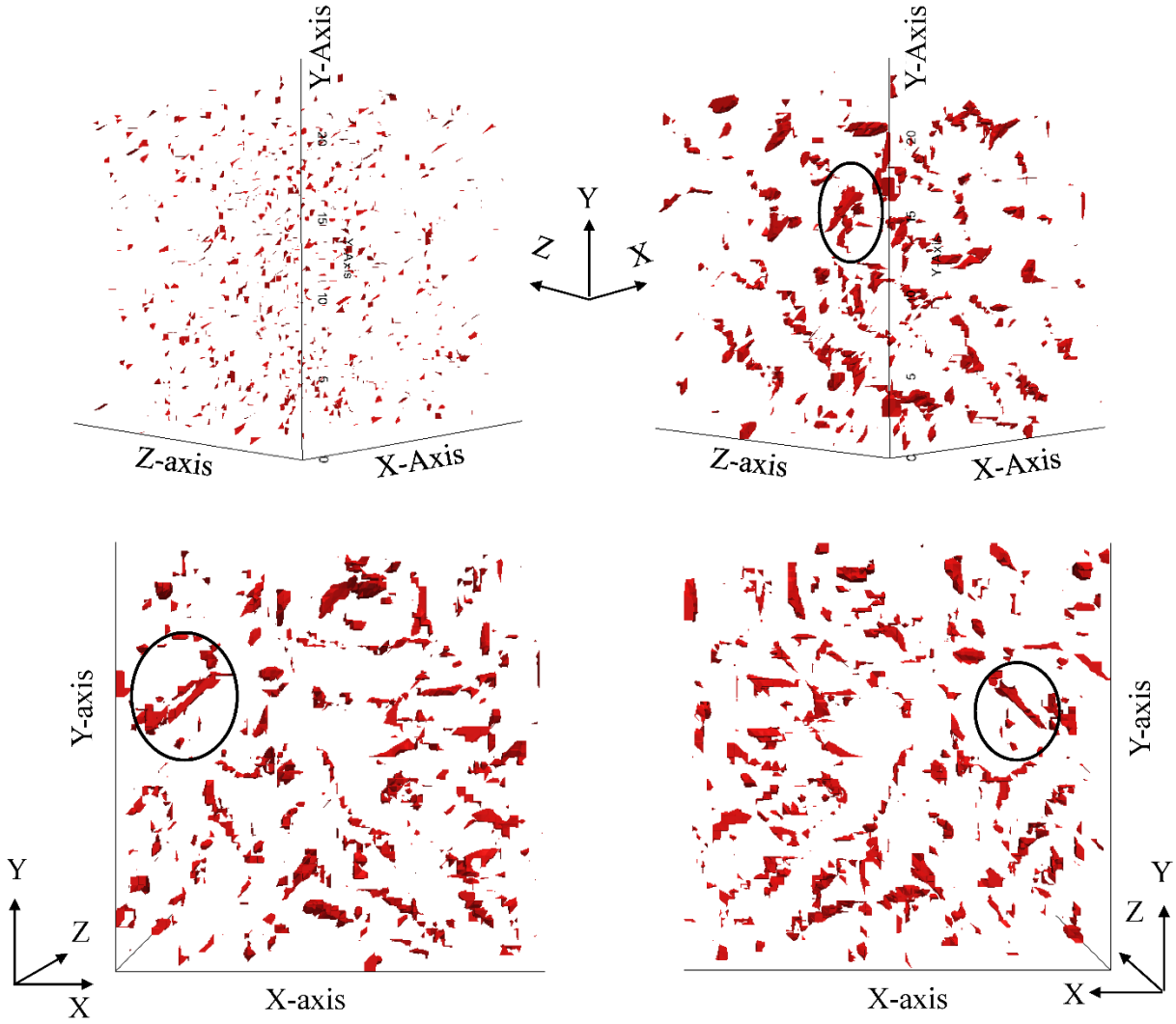

Figure 4.8. Temporal evolution of pore phase. (a) Pore phase at the beginning of the simulation, T=40; (b) Crack formation in the microstructure during evolution at T=1000

The microstructural features and effective material properties extracted from meso-scale phase-field simulations can be utilized to investigate the influence of Ni coarsening on the electrochemical performance degradation of SOFCs. For the electrochemical analysis in this section, we assigned an absolute value to the size of non-evolving YSZ particle as the characteristic length scale. In order to make the results as general as possible, all dimensions were scaled with respect to the characteristic length and no absolute physical dimensions of the simulation box had been assigned. Peak power density plots are shown to quantify the performance degradation of SOFC due to microstructural evolution. Figure 4.9 compares the peak power density plot at the initial stage and after the degradation for an anode. The result shows, the peak density is 9550 W m^{-2} at the initial stage of the operation. However, the final peak power density decreases by 4.3% and reaches to 9150 W m^{-2} after the initial 500 hours of operation. After 1000 hours of operation the peak power density is further reduced to 8680 W m^{-2}. Overall, 1000 hours of operation results in 9.11% decreased power output. However, the performance degradation appears to slow down during 500-1000 simulation time steps. The performance degradation is caused by the combined effects of continuous loss of TPB area, a decrease in electronic conductivity, and the crack formation.

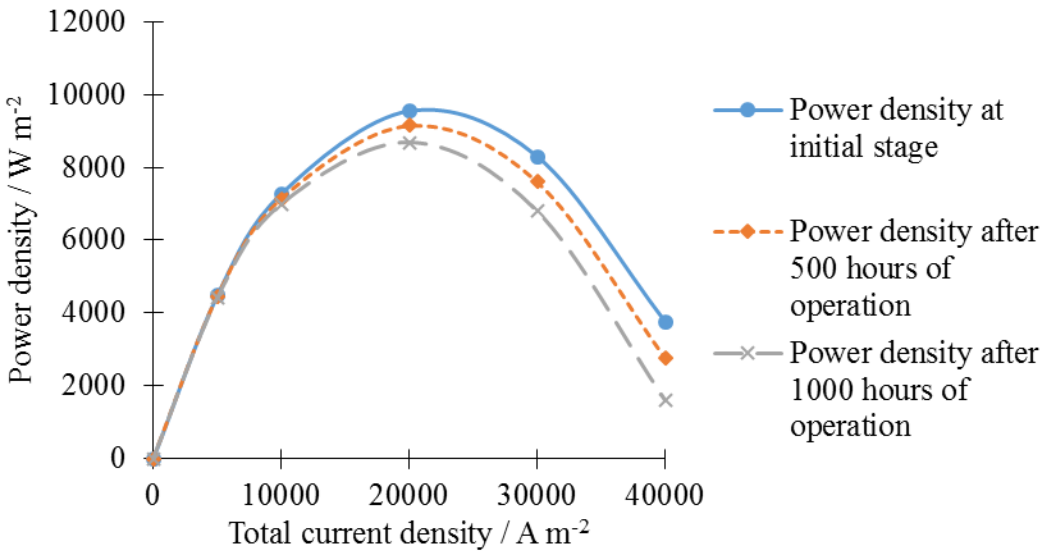

Figure 4.9. Comparison of power density plot at different stages of the microstructural evolution for anode.

Figure 4.10 shows the performance degradation of anode supported SOFC due to crack formation. The formation of crack causes the interruption of current flow, which in turn increases the polarization resistance of the anode microstructure. The increased polarization resistance due to crack formation causes a sudden fall in the power density curve [51, 52]. The peak power density at the initial stage of anode supported SOFC is 11345.34 W m^{-2}. But the formation of cracks causes increased resistance and results in a 27% reduction in the peak power density and the obtained peak power density is 8210 W m^{-2}.

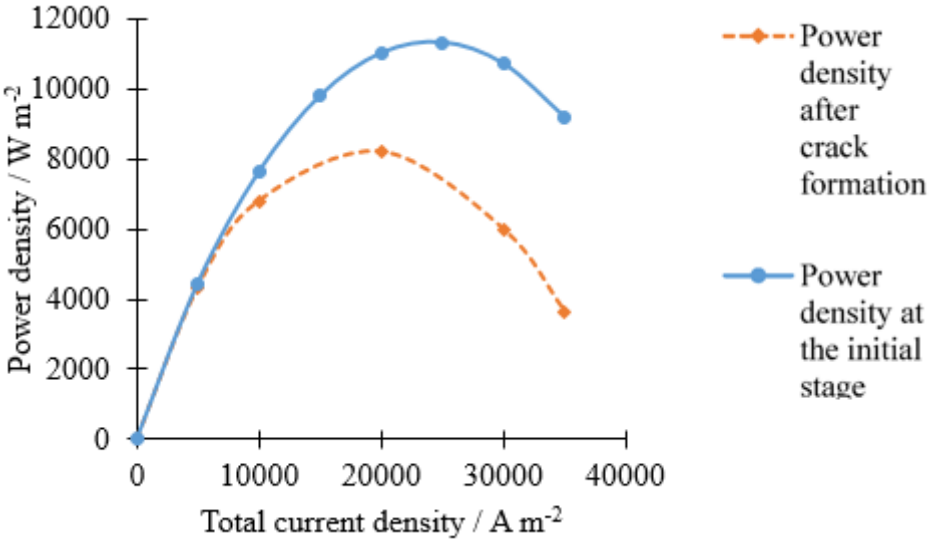

Figure 4.10. Power density curve before and after crack formation for anode.

4.6 CONCLUSION

A meso-scale phase-field model is developed to investigate performance degradation and crack formation during anode microstructural evolution. A phase-field model was developed to illustrate the effect of Ni particle coarsening in electrode microstructure. Randomly generated microstructure was considered and the time step size of 1 hour was used for the simulation. Developed phase-field model was validated against the experimental work by Tanasini *et al.* [24] the modeling work can be used to predict the morphology of three phases associated with the electrode. The volume fraction of the phases is used to find out the TPB area reduction. Statistical material properties due to microstructural changes obtained from the phase-field simulation results are used as input parameter to the previously developed cell level model to quantify the performance degradation.

The simulation result shows that the average particle size is increased during temporal microstructural evolution. The Ni particle size is increased by 26%, which leads to the TPB area reduction. Moreover, TPB phase contiguity is also affected significantly due to 24% reduction if Ni-YSZ particle size. Temporal evolution of the microstructure leads to a decrease in the TPB area by 24%, which has a profound effect on the microstructural performance level. The power output is found to be decreased by 11.03% after 1000 hours of operation. Additionally, crack formation due to the accumulation of pores during phase diffusion is also demonstrated. This work is expected to provide us a comprehensive understanding of SOFCs' microstructural evolution as well as a tool for SOFC's performance degradation analysis.

4.7 LIST OF SYMBOLS

Greek Letters

α	Gradient energy coefficient
γ_s	Surface energy
ζ	Order parameter for Ni particle
ξ	Order parameter for YSZ
ϑ	Order parameter for crack
ε	Strain tensor
μ	Chemical potetntial of the anode
φ	Gradient energy coeffiecient
ω	Relaxation constant

σ	Threshold strain
σ_{st}	Elastic energy density
δ_s	Interfacial thickness
υ	Poisson's ratio
$\vec{v}$	Unit interface normal
Ω	Volume fraction of the phase
τ	Time scale for surface diffusion

Latin Letters

C_l	Lower cutoff order parameter value
C_h	Upper cutoff order parameter value
D_s	Surface diffusion coefficient
E	Young's modulus
F_{tot}	Total free energy
H	Energy barrier
k_B	Boltzman constant
k_c	Local curvature
L	Characteristic length
M	Mobility
N_v	Atomic number density per volume
T	Time (sec)
V_n	Normal velocity

V	Total volume
s	Surface
n	Normal

Operator

∇^2	Laplacian
π	Multiplication notation
$\partial/\partial s$	Gradient operator along the interface

4.8 REFERENCE

1. Liu, L., et al., *Modeling of solid oxide fuel cells with particle size and porosity grading in anode electrode.* Fuel Cells, 2012. **12**(1): p. 97-108.
2. Ge, X.M., et al., *Solid oxide fuel cell anode materials for direct hydrocarbon utilization.* Advanced Energy Materials, 2012. **2**(10): p. 1156-1181.
3. Liu, L., *Solid oxide fuel cell reliability and performance modeling and fabrication by spray pyrolysis*, in *Mechanical Engineering*. 2011, Iowa State University: Digital Repository@ Iowa State University.
4. Stambouli, A.B. and E. Traversa, *Solid oxide fuel cells (SOFCs): a review of an environmentally clean and efficient source of energy.* Renewable and Sustainable Energy Reviews, 2002. **6**(5): p. 433-455.

5. Wachsman, E.D. and K.T. Lee, *Lowering the temperature of solid oxide fuel cells.* Science, 2011. **334**(6058): p. 935-939.

6. Liu, L., G.-Y. Kim, and A. Chandra. *Life Prediction of a Solid Oxide Fuel Cell Under Thermal Cycling Conditions*. in *ASME 2009 7th International Conference on Fuel Cell Science, Engineering and Technology*. 2009. American Society of Mechanical Engineers.

7. Abdullah, T. and L. Liu, *Phase Field Simulation Coupling Microstructural Evolution and Crack Propagation during Performance Degradation of Solid Oxide Fuel Cells.* ECS Transactions, 2015. **66**(2): p. 207-217.

8. Liu, L., G.-Y. Kim, and A. Chandra, *Modeling of thermal stresses and lifetime prediction of planar solid oxide fuel cell under thermal cycling conditions.* Journal of Power Sources, 2010. **195**(8): p. 2310-2318.

9. Li, Q., et al., *Phase-field modeling of three-phase electrode microstructures in solid oxide fuel cells.* Applied Physics Letters, 2012. **101**(3): p. 033909.

10. Chen, L. and J. Shen, *Applications of semi-implicit Fourier-spectral method to phase field equations.* Computer Physics Communications, 1998. **108**(2): p. 147-158.

11. Lichtner, A., et al., *Dispersion, connectivity and tortuosity of hierarchical porosity composite SOFC cathodes prepared by freeze-casting.* Journal of the European Ceramic Society, 2015. **35**(2): p. 585-595.

12. Abdullah, T. and L. Liu, *Peak Power Optimization of Solid Oxide Fuel Cells with Particle Size and Porosity Grading.* ECS Transactions, 2014. **61**(13): p. 33-46.

13. Liu, L., *Solid oxide fuel cell reliability and performance modeling and fabrication by spray pyrolysis.* 2011.

14. Mogensen, M. and S. Skaarup, *Kinetic and geometric aspects of solid oxide fuel cell electrodes.* Solid State Ionics, 1996. **86**: p. 1151-1160.

15. Holzer, L., et al., *Microstructure degradation of cermet anodes for solid oxide fuel cells: Quantification of nickel grain growth in dry and in humid atmospheres.* Journal of Power Sources, 2011. **196**(3): p. 1279-1294.

16. Liu, L., G.-Y. Kim, and A. Chandra, *Modeling of Ni–CGO anode in a solid oxide fuel cell deposited by spray pyrolysis.* Journal of Power Sources, 2012. **210**: p. 129-137.

17. Chinda, P., et al., *Microscale Modeling of an Anode-Supported Planar Solid Oxide Fuel Cell.* Fuel Cells, 2011. **11**(2): p. 184-199.

18. Chen, L.-Q., *Phase-field models for microstructure evolution.* Annual review of materials research, 2002. **32**(1): p. 113-140.

19. Abdeljawad, F., et al., *Connecting microstructural coarsening processes to electrochemical performance in solid oxide fuel cells: An integrated modeling approach.* Journal of Power Sources, 2014. **250**: p. 319-331.

20. Liu, Z. and P.P. Mukherjee, *Microstructure evolution in lithium-ion battery electrode processing.* Journal of The Electrochemical Society, 2014. **161**(8): p. E3248-E3258.

21. Ostwald, W., *On the assumed isomerism of red and yellow mercury oxide and the surface-tension of solid bodies.* Zeitschrift Fur Physikalische Chemie--Stochiometrie Und Verwandtschaftslehre, 1900. **34**(4): p. 495-503.

22. Marqusee, J. and J. Ross, *Theory of Ostwald ripening: Competitive growth and its dependence on volume fraction.* The Journal of chemical physics, 1984. **80**(1): p. 536-543.

23. Perez, M., *Gibbs–Thomson effects in phase transformations.* Scripta Materialia, 2005. **52**(8): p. 709-712.

24. Tanasini, P., et al., *Experimental and theoretical investigation of degradation mechanisms by particle coarsening in SOFC electrodes.* Fuel Cells, 2009. **9**(5): p. 740-752.

25. Simwonis, D., F. Tietz, and D. Stöver, *Nickel coarsening in annealed Ni/8YSZ anode substrates for solid oxide fuel cells.* Solid State Ionics, 2000. **132**(3): p. 241-251.

26. Nelson, G.J., et al., *Three-dimensional microstructural changes in the Ni–YSZ solid oxide fuel cell anode during operation.* Acta Materialia, 2012. **60**(8): p. 3491-3500.

27. Faes, A., et al., *Nickel–zirconia anode degradation and triple phase boundary quantification from microstructural analysis.* Fuel cells, 2009. **9**(6): p. 841-851.

28. Iwata, T., *Characterization of Ni-YSZ Anode Degradation for Substrate-Type Solid Oxide Fuel Cells.* Journal of the Electrochemical Society, 1996. **143**(5): p. 1521-1525.

29. Cronin, J.S., J.R. Wilson, and S.A. Barnett, *Impact of pore microstructure evolution on polarization resistance of Ni-Yttria-stabilized zirconia fuel cell anodes.* Journal of Power Sources, 2011. **196**(5): p. 2640-2643.

30. Chen, H.-Y., et al., *Simulation of coarsening in three-phase solid oxide fuel cell anodes.* Journal of Power Sources, 2011. **196**(3): p. 1333-1337.

31. Abdeljawad, F.F., *Mesoscale Modeling of Heterogeneous Materials Systems: From Solid Oxide Fuel Cells to Bulk Metallic Glasses*, in *Mechanical and Aerospace Engineering Department*. 2014, Princeton University.

32. Atkinson, A., et al., *Advanced anodes for high-temperature fuel cells.* Nature materials, 2004. **3**(1): p. 17-27.

33. Mallard, W., et al., *Self-diffusion in silver-gold solid solutions.* Physical Review, 1963. **129**(2): p. 617.

34. Bonzel, H. and E. Latta, *Surface self-diffusion on Ni (110): Temperature dependence and directional anisotropy.* Surface Science, 1978. **76**(2): p. 275-295.

35. Mayo, M., *Zr surface diffusion in tetragonal yttria stabilized zirconia.* Journal of Materials Science, 2000. **35**(2): p. 437-442.

36. Zuo, P. and Y.-P. Zhao, *A phase field model coupling lithium diffusion and stress evolution with crack propagation and application in lithium ion batteries.* Physical Chemistry Chemical Physics, 2015. **17**(1): p. 287-297.

37. Brailsford, A. and P. Wynblatt, *The dependence of Ostwald ripening kinetics on particle volume fraction.* Acta Metallurgica, 1979. **27**(3): p. 489-497.

38. Hardy, S. and P. Voorhees, *Ostwald ripening in a system with a high volume fraction of coarsening phase.* Metallurgical Transactions A, 1988. **19**(11): p. 2713-2721.

39. Aranson, I., V. Kalatsky, and V. Vinokur, *Continuum field description of crack propagation.* Physical Review Letters, 2000. **85**(1): p. 118.

40. Karma, A., D.A. Kessler, and H. Levine, *Phase-field model of mode III dynamic fracture.* Physical Review Letters, 2001. **87**(4): p. 045501.

41. Miehe, C., M. Hofacker, and F. Welschinger, *A phase field model for rate-independent crack propagation: Robust algorithmic implementation based on operator splits.* Computer Methods in Applied Mechanics and Engineering, 2010. **199**(45): p. 2765-2778.

42. Marconi, V. and E. Jagla, *Diffuse interface approach to brittle fracture.* Physical Review E, 2005. **71**(3): p. 036110.

43. Bueno-Orovio, A. and V.M. Pérez-García, *Spectral smoothed boundary methods: the role of external boundary conditions.* Numerical Methods for Partial Differential Equations, 2006. **22**(2): p. 435-448.

44. Chen, H.-Y., Y. Kwon, and K. Thornton, *Multifunctionality of three-dimensional self-assembled composite structure.* Scripta Materialia, 2009. **61**(1): p. 52-55.

45. Gránásy, L., et al., *Phase field theory of heterogeneous crystal nucleation.* Physical review letters, 2007. **98**(3): p. 035703.

46. Warren, J.A., et al., *Phase field approach to heterogeneous crystal nucleation in alloys.* Brunel Centre for Advanced Solidification Technology;, 2009.

47. Laurencin, J., et al., *A numerical tool to estimate SOFC mechanical degradation: case of the planar cell configuration.* Journal of the European Ceramic Society, 2008. **28**(9): p. 1857-1869.

48. Karma, A. and A.E. Lobkovsky, *Unsteady crack motion and branching in a phase-field model of brittle fracture.* Physical review letters, 2004. **92**(24): p. 245510.

49. Wise, S.M., et al., *Efficient phase-field simulation of quantum dot formation in a strained heteroepitaxial film.* Superlattices and Microstructures, 2004. **36**(1-3): p. 293-304.

50. Yeon, D.H., P.R. Cha, and M. Grant, *Phase field model of stress-induced surface instabilities: Surface diffusion.* Acta Materialia, 2006. **54**(6): p. 1623-1630.

51. Pihlatie, M., T. Ramos, and A. Kaiser, *Testing and improving the redox stability of Ni-based solid oxide fuel cells.* Journal of Power Sources, 2009. **193**(1): p. 322-330.

52. Fouquet, D., et al., *Kinetics of oxidation and reduction of Ni/YSZ cermets.* Ionics, 2003. **9**(1-2): p. 103-108.

CHAPTER 5 . CONCLUSION AND SCIENTIFIC CONTRIBUTION

5.1 CONCLUSION

5.1.1 SUMMARY

This study strengthens the understanding of SOFC electrochemical performance with graded microstructure and shed light on the microstructural evolution of SOFC. In order to fully understand the SOFC electrochemical performance with tailored microstructure, a cell level microstructure model has been developed incorporating both particle size and porosity grading. The modeling work illustrates the effect of functionally graded electrode on the performance of SOFC. Then, a meso-scale phase-field model has been developed combining the Chan Hilliard and Ginzburg-Landau equations to investigate the microstructural evolution. The model successfully predicts the performance degradation due to the Ni particle coarsening as well as crack formation. Several microstructural attributes such as TPB area, particle size, particle size ratio, and pore space were tracked down to examine the performance degradation during microstructural evolution.

5.1.2 SIMULATION BASED MICROSTRUCTURAL OPTIMIZATION OF SOLID OXIDE FUEL CELL FOR LOW TEMPERATURE OPERATION

In this study, functionally graded electrode microstructure was studied to compensate the effect of reducing operating temperature. A complete cell level microstructural modeling based on

the functionally graded electrode was developed to examine the effect of non-linear grading. The modeling approach was based on the minimization of the voltage losses associated with SOFC. The numerical model considered both particle size and porosity grading to compare the performance of homogenous, linear, and non-linear graded electrode. The following conclusions have been drawn from this study.

1. Among three different losses associated with SOFC the activation loss is more significant than other two.
2. Microstructure grading of electrode demonstrates improved power output compared to the homogenous electrode. Additionally, nonlinear grading can show a significant benefit over linear microstructural grading.
3. Combined effect of particle size and porosity grading in SOFC microstructure is used in this work. Typically, the particle size is more influential compared to the porosity grading but the combination of particle size and porosity grading results in enhanced power output.
4. Performance optimization of SOFC can enable SOFCs to operate at a reduced temperature (as low as 873 K) while maintaining the performance of high-temperature SOFCs.

5.1.3 A PHASE-FIELD MODEL OF COUPLED MICROSTRUCTURAL EVOLUTION AND CRACK FORMATION IN SOLID OXIDE FUEL CELL

In this study, a meso-scale phase-field model was developed to illustrate the microstructural evolution. The modeling framework examined the microstructural evolution based on the minimization of total free energy. Randomly disordered microstructure model is used to investigate the evolution. The evolution of Ni phase is considered to be driven by the

interface diffusion of Ni phase where YSZ composite is considered stationary. Simulation result of the phase-field model is applied to the previously developed microstructure model for the quantitate analysis of the performance degradation. The following conclusions can be drawn from the integrated phase-field model.

1. Rapid microstructural evolution occurs at the initial stages caused by relatively higher total free energy, which appears to slow down with time.
2. Accumulation of pores and pre-existing cracks during phase diffusion causes crack formation. Initial crack formation takes time, then the crack develops quickly due to stress concentration.
3. The average Ni particle size is increased during temporal microstructural evolution by 26%, which leads to the TPB area reduction.
4. The temporal microstructural evolution affects the contiguity of TPB area which significantly reduced by 24%.

5.2 SCIENTIFIC CONTRIBUTIONS

The major scientific contributions of the thesis may be summarized as the following:

1. The work provided insight on the effect of nonlinear particle size and porosity grading on the electrode microstructure. A multi-scale cell level model was developed to incorporating both particle size and porosity grading to optimize the peak power density of SOFC.
2. The cell-level, multi-scale model demonstrates that a properly graded electrode can significantly reduce the adverse effect of lowering operating temperature and enable

SOFCs to operate at a reduced temperature (as low as 873 K) while maintaining the performance at high temperature of 1273 K.

3. Meso-scale phase field model in expected to provide a comprehensive understanding of SOFCs' microstructural evolution as well as a tool for SOFC's performance degradation analysis.

5.3 RECOMMENDATION FOR FUTURE WORK

1. Randomly disordered particle structure is used to explore the microstructural degradation and crack formation. So designing a controlled microstructures will be helpful to determine and predict the exact location of the crack.
2. A complete cell level model could be developed by coupling thermo-mechanical model and electrochemical model that could be used as an effective tool for designing and optimizing cell structure.